UNIVERSITÀ DEGLI STUDI
DI MODENA E REGGIO EMILIA

Dottorato di ricerca in Neuroscienze
in convenzione con l'Università degli Studi di Parma

Ciclo XXXII

"Neuromorphic Organic Sensors for Neurotransmitters"

Candidata: Martina Giordani

Relatore (Tutor): Prof. Fabio Biscarini

Correlatore (Co-Tutor): Prof. Michele Zoli

Coordinatore del Corso di Dottorato: Prof. Michele Zoli

To Niccolò and Irma

List of publications

Giordani et al., *"Whole organic electronic synapse for dopamine detection"*, Proceedings of SPIE, IX 9944, **2016**

Di Lauro et al., *"Liquid-gated organic electronic devices based on high-performance solution-processed molecular semiconductor"*, Advanced Electronic Materials 3(9), 1700159, **2017**

Giordani et al., *"Specific dopamine sensing based on short-term plasticity behavior of a whole organic artificial synapse"*, ACS sensors 2(12), 1756-1760, **2017**

Di Lauro et al*., "A bacterial photosynthetic enzymatic unit modulating organic transistors with light"* Advanced Electronic Materials 6(1), 1900888, **2020**

Giordani et al., *"Neuromorphic organic devices that specifically discriminate dopamine from its metabolites by nonspecific interactions"*, Advanced Functional Materials 30(28), 2002141, **2020**

List of attended conferences and workshop

6 December 2019
"XIX Giornata della Chimica dell'Emilia Romagna", Modena (Italy): poster presentation

12-14 June 2019
"1st Workshop on Neuromorphic Organic Devices", Ferrara, (Italy): oral talk

17 December 2018
"XVIII Giornata della Chimica dell'Emilia Romagna, Parma, (Italy): poster presentation

22-26 October 2018
"Italian National Conference on Materials Science and Technology", Bologna, (Italy): oral talk

1 December 2017
"XVII Giornata della Chimica dell'Emilia Romagna", Bologna (Italy): flash talk

25-27 October 2017

"OrBItaly2017 - Organic Bioelectronics in Italy: from Biosensors to Neuronal Interfaces", Cagliari (Italy): poster presentation and oral talk

24 February 2017
"New Perspectives in Neuroscience: Research Results of Young Italian Neuroscientists", Napoli (Italy): poster presentation

19 December 2016
"XVI Giornata della Chimica dell'Emilia Romagna", Ferrara (Italy): poster presentation

8-10 June 2016

Workshop in memoriam of Carlo Taliani, Bologna (Italy)

10-11 September 2015

"OrBItaly2015 - Organic Bioelectronics in Italy: from Biosensors to Neuronal Interfaces", Modena (Italy)

Report of PhD activities

First year (2016-2017): during my first year of PhD I optimized the architecture and fabrication of the sensor that I developed during my master thesis; moreover I improved the R script for the extraction of the maxima of current. I tested the sensor for dopamine, ascorbic acid and uric acid. The measurements were repeated different times, in order to have a strong statistics.

Second year (2017-2018): I tested the sensor for different metabolites/catabolites and neurotransmitters present in the extracellular and cerebrospinal fluid (i.e. 3-MT, homovanillic acid, DOPAC, epinephrine, norepinephrine).

Maternity leave from February 2018 to July 2018.

Third year (2018-2019-2020): with the help of Dr. Matteo Sensi, we performed the Density-theory functional calculation for PEDOT:PSS with DA, 3-MT, norepinephrine and epinephrine and we simulated a simple RC circuit in order to understand the mode of operation of the sensor. Moreover, during this year I collected the literature on "Neuromorphic devices" in order to publish a review on this topic.

Maternity leave from February 2020 to July 2020.

Abstract

In this thesis an ultra-sensitive and selective sensor for dopamine (DA) by means of a neuro-inspired device platform without the need of a specific recognition moiety is demonstrated.

DA is a neurotransmitter of catecholamines family that controls functions of cardiovascular, renal, hormonal and central nervous systems. DA deficit is a hallmark of Parkinson's disease (PD), due to the degeneration of dopaminergic neurons in *substantia nigra pars compacta.*

The sensor is a whole organic device featuring two electrodes made of poly(3,4-ethylenedioxythiophene):polystyrene sulfonate – PEDOT:PSS – directly patterned through laser ablation on a polydymethylsiloxane – PDMS – flexible substrate. One electrode is pulsed with a train of voltage square waves (-200 mV with a frequency of 500 Hz for 1s), to mimic the pre-synaptic neuron behavior, while the other is used to record the displacement current, mimicking the post-synaptic neuron. The current response exhibits the features of synaptic Short-Term Plasticity (STP) with facilitating or depressing response according to the stimulus frequency. We found that the resulting current decreases with a characteristic time, τ_{STP} , depending on DA concentration in solution. The sensor detects [DA] down to 1 pM range. We assess the sensor also in the presence of several moieties physiologically present in cerebrospinal fluid or extracellular fluids, i.e. ascorbic acid, uric acid, 3-methoxytyramine, 3,4-dihydroxyphenylacetic acid, homovanillic acid, epinephrine and norepinephrine. Our detection strategy successfully discriminates DA from the other analytes in model solutions (i.e. Phosphate Saline Buffer). The sensor appears still more sensitive to DA than to the others, even in presence of moieties with similar chemical structures. The synapse appears ultrasensitive to DA (from physiological to pathological concentrations) and selective thanks to the interaction mechanism with PEDOT:PSS. Density-fuctional theory calculations on PEDOT:PSS/metabolite clusters hint to a correlation between the STP response and stronger non-covalent interactions between DA and PEDOT:PSS, specifically electrostatic and hydrogen bonding of DA ammonium end group with sulfonate. Moreover we demonstrated with a simple RC circuit the operation mode of the sensor.

The whole organic synapse, being biocompatible, soft and flexible, is attractive for implantable devices aimed to real-time monitoring of DA concentration in bodily fluids, to be used as a diagnostic tool, for instance, in chronic neurodegenerative diseases such as Parkinson's disease.

Nel presente lavoro di tesi è presentato un sensore per la dopamina (DA) per mezzo di un dispositivo che non necessita di un specifica specie di riconoscimento.

La DA è un neurotrasmettitore appartenente alla famiglia delle catecolamine che controlla alcune funzioni del sistema cardiovascolare, renale, ormonale e nervoso. La diminuzione dei livelli di DA, dovuta alla degenerazione dei neuroni dopaminergici della *substantia nigra pars compacta*, è un segnale che indica la comparsa del morbo di Parkinson (PD).

Il sensore è completamente organico e presenta due elettrodi di poly(3,4-ethylenedioxythiophene):polystyrene sulfonate – PEDOT:PSS – direttamente modellati sul substrato flessibile di polidimetilsilossano (PDMS).

Il protocollo di misura prevede che uno dei due elettrodi sia pulsato con un treno di onde quadre (-200 mV con una frequenza di 500 Hz per 1 s), in modo da simulare il comportamento di un neurone pre-sinaptico, mentre l'altro viene utilizzato per misurare la corrente risultante, simulando un neurone post-sinaptico. La risposta in corrente mostra le caratteristiche della Short-Term Plasticity (STP) neuronale con un comportamento depressivo o facilitativo a seconda della frequenza di stimolo. Durante questo lavoro di tesi abbiamo dimostrato come la corrente risultante dal protocollo di stimolo decadesse con un tempo caratteristico τ_{STP}, dipendente dalla concentrazione di DA in soluzione. Il sensore è in grado di rivelare concentrazioni sotto al pM. Inoltre abbiamo testato il sensore anche in presenza di altre molecole fisiologicamente presenti nel fluido cerebrospinale e nel fluido extracellulare, i.e. acido ascorbico, acido urico, 3-metossitiramina, acido 3,4-diidrossifenilacetico, acido omovanillico, adrenalina e noradrenalina. La nostra strategia di rilevazione è in grado di distinguere la DA dagli altri analiti in soluzioni modello (i.e. Buffer Salino Fosfato). Il sensore risulta essere ancora più sensibile alla DA rispetto alle altre specie chimiche, anche in copresenza con molecole con strutture chimiche simili. La sinapsi artificiale appare ultra-sensibile alla DA (da concentrazioni fisiologiche, fino a quelle patologiche) e selettiva grazie a meccanismi di interazioni con il PEDOT:PSS. I nostri dati sperimentali sono poi stati confermati da calcoli DFT su PEDOT:PSS/metaboliti suggerendo una correlazione tra la risposta STP e le forti interazioni non covalenti tra DA e PEDOT:PSS, in particolare interazioni elettrostatiche e legami idrogeno con l'ammonio della DA e il sulfonato. Inoltre, il funzionamento del sensore è stato confermato da simulazioni attuate su un semplice circuito RC.

Questa sinapsi totalmente organica, essendo anche biocompatibile e flessibile risulta essere un buon candidato per futuri impianti in modelli animali con malattie neurodegenerative, come il PD, con l'obiettivo di andare a monitorare in tempo reale la concentrazione di DA nei fluidi biologici e per essere utilizzata come strumento diagnostico.

CONTENTS

1 INTRODUCTION

This chapter introduces the role of dopamine in the brain, what (bio)sensing is and the standard techniques of dopamine sensing; it defines the field of organic (bio)electronics from its first applications to its employment nowadays in the field of neuroscience; the final section outlines the aim of this work of thesis.

1.1 PHYSIOLOGICAL ROLE OF DOPAMINE

Dopamine (DA) is an important neurotransmitter that belongs to catecholamine family. In the brain DA controls the reward-motivated behavior, moreover it is implicated in executive functions, motor control, motivation, arousal and reinforcement.[1]

DA was firstly found in plants[2] and later has been recognized as substrate of aromatic amino acid decarboxylase[3], which could be isolated from sympathetic ganglia and other animal tissues. DA was considered the precursor of neurotransmitters as epinephrine (EPI) and norepinephrine (NE), only years later was recognized as an independent neurotransmitter.[4,5] In the 50s the studies of Arvid Carlsson together with Eric Kandel and Paul Greengard brought to new techniques of DA measurements that culminate with their Nobel Prize in medicine and physiology in 2000. Quickly, DA imbalances were associated to Parkinson's disease (PD), schizophrenia, attention deficit hyperactivity disorders and Segawa disease.

DA production in central nervous system (CNS) was postulated by Blaschko in 1939 [6]: the two steps of its synthesis take place in the cytosol of catecholaminergic neurons and starts with the hydroxylation of L-tyrosine by tyrosine hydroxylase to yield DOPA. DOPA is then decarboxylated to DA by aromatic amino acid decarboxylase. Another possibility for DA biosynthesis is the tyrosinase hydroxylation of tyrosine and the subsequent uptake of DOPA by catecholaminergic neurons (Figure 1.1)

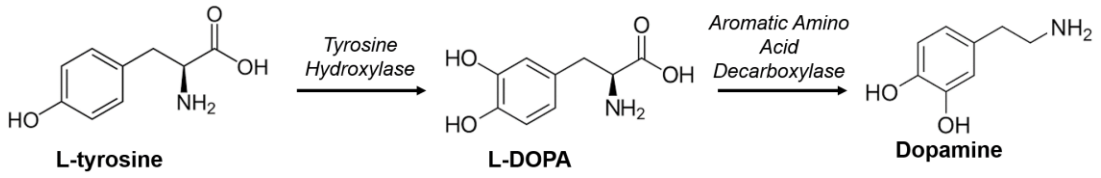

Figure 1.1 Biosynthesis of dopamine: L-tyrosine is hydroxylated by tyrosine hydroxylase and then transformed in dopamine by aromatic amino acid decarboxylase.

In catecholaminergic neurons DA is sequestered into synaptic vesicles and stabilized by the acidic pH into them. Once vesicles are emptied into the synaptic cleft, DA interacts with its post-synaptic receptors. The reuptake of DA is made by glial cells and followed by the sequestration into synaptic storage vesicles by vesicular monoamine transporter 2 (VMAT2), while DA in the cytosol is degraded by monoamine oxidase (MAO), producing the reactive 3,4-dihydroxyphelylacetaldehyde (DOPAL). DOPAL is inactivated in 3,4-dihydroxyphenylethanol (DOPET) or to 3,4-dihydroxyphenylacetc acid (DOPAC) by alcohol dehydrogenase or aldehyde dehydrogenase, respectively. Synaptic cleft is also emptied by surrounding glial cells that

degrade DA by MAO and catechol-O methyl transferase (COMT), that converts DOPAC into homovanillic acid (HVA).[7] The metabolic pathway is showed in Figure 1.2.

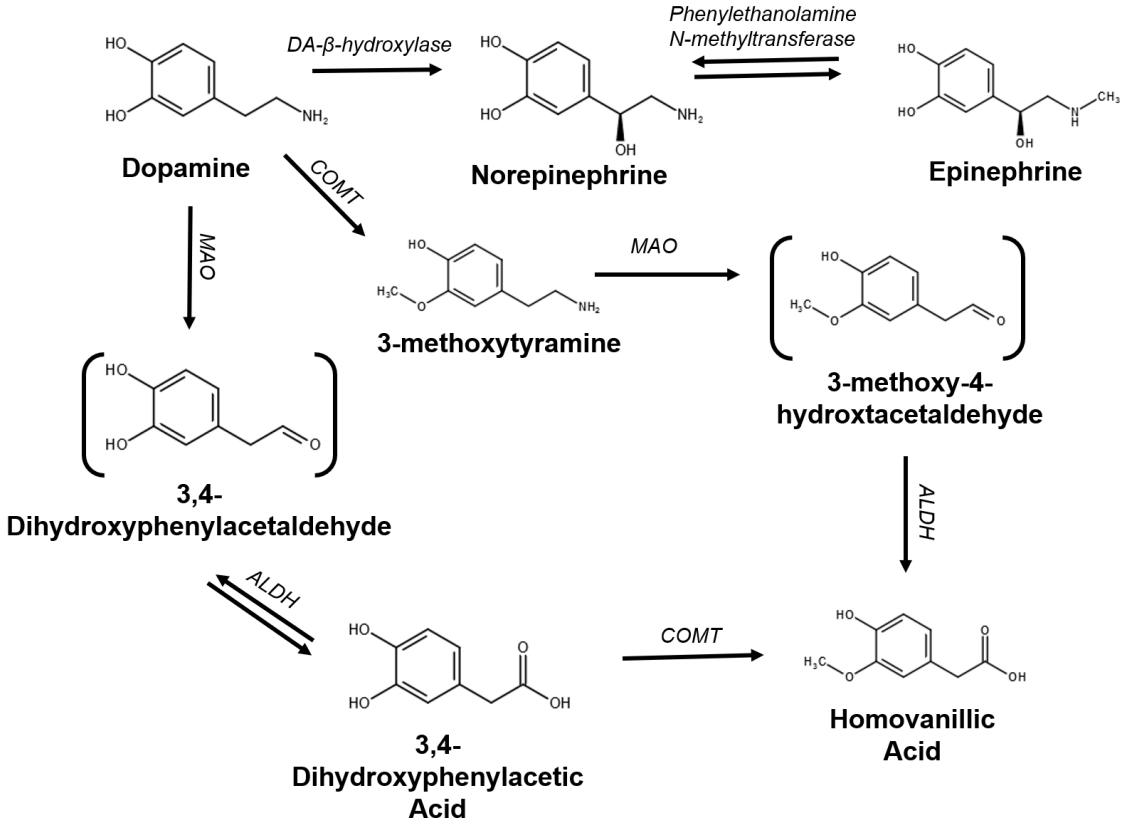

Figure 1.2 Metabolic pathway of DA.

The oxidative deamination of catecholamines by MAO generate hydrogen peroxide causing oxidative stress in catecholaminergic neurons, moreover, DA, as well as the other catecholamines, is prone to oxidation, due to its electron-rich catechol, producing neuromelanin (NM).[8] NM is a pigment mainly found in *substantia nigra pars compacta* and in *locus coerulus* synthesized by non-vesicular DA. NM interacts through π-stacking interactions forming a polymer, that is not clear if it is degradable *in vivo* or not.

1.1.1 Parkinson's Disease

PD is a neurodegenerative disorder characterized by motor deficits, rigidity, postural instability and tremor at rest, together with anosmia, depressed mood, psychosis, pain, disruption of sleep and cognitive dysfunction.[9]

The most common feature of PD is the age-related degeneration of nigrostriatal dopaminergic pathways of the *striatum* with the subsequent loss of neurons.[10]

PD is just symptomatically treated with L-DOPA, an endogenous precursor of DA. This treatment raise levels of DA, reducing motor symptoms, but is poorly effective against non-motor symptoms.
Other types of therapies are the functional stereotaxic neurosurgery (deep brain stimulation) performed in the ventral intermediate nucleus, subthalamic nucleus and *globus pallidus*, and supportive therapies (physiotherapy, speech therapy and dietary measures).[11]

1.1.2 Review on dopamine sensing

Sensing DA in bodily fluid is really challenging, since it requires high sensitivity and selectivity, due to low physiological basal levels ($9x10^{-11}$ M in cerebrospinal fluid and $1x10^{-9}$-$3x10^{-8}$ M in extracellular fluid) and to the presence of other molecules with similar redox potentials in the extracellular fluid, respectively.
The standard techniques rely on different charges and/or mass of the analyte, or on redox potentials.

- Capillary Electrophoresis, shown in Figure 1.3 a, is a technique that, since two decades, has been used for *in vivo* monitoring of neurotransmitters levels, mainly glutamate. For samples like DA the sensing is difficult, because of the low concentration (nM range) and the presence of inteferings. It has the advantage of being performed on a small amount of sample.[12]
- High-Performance Liquid Chromatography (HPLC), shown in Figure 1.3 b, is the most common technique used to determine the levels of catecholamines in biological samples. The advantage of HPLC is the use of a small amount of sample; on the other hand, it is not suitable for portable or low cost analysis.[13,14]
- Mass Spectrometry, shown in Figure 1.3 c, as HPLC, allows low detection limits, but is a very expensive technique, not suitable for *in vivo* analysis.[13]
- Micro-dialysis is the most common method used for preparation of samples from brain extracellular fluid. A dialysis probe, shown in Figure 1.3 d, is placed into the region of the brain of interest; the probe is permeable to small molecules that can perfuse. This perfusate is then analyzed with HPLC. This technique cannot be used for assessing *in vivo* real-time analysis.[15]

These methods guarantee a good selectivity and a low LODs, but they also had lot of disadvantages, first and foremost the expensive instrumentations. Moreover these techniques require complex pre-treatment steps, without permitting the non-invasive and real time monitoring of the analytes. Nowadays, an inexpensive alternative to these techniques is the use of electrochemical sensors (Figure 1.3 e): one of the first electrochemical sensor was reported by Adams and coworkers in 1967, were they studied the oxidation mechanism of some catecholamines, as DA, NE and EPI, as function of pH.[16] Adams

and his coworkers were also the first to implant carbon electrodes in the brain, measuring in vivo the levels of catecholamines in extracellular fluid.[17]

Despite electrochemical measurements have been an effective method of measuring catecholamines, it has some disadvantages: first of all, brain is a challenging environment for chemical sensing, because of the presence of analytes with similar oxidation potentials (i.e. DA, UA, AA). Moreover, the oxidation products of catecholamines passivate the electrode surface, producing melanin-type polymer films, implying a poor selectivity and reproducibility. Finally, this technique does not allow the sensing down to the nanomolar range, needed in physiological and pathological conditions.[18] Concerning the *in vivo* measurements, problems with this technique are associated to the invasive probes and the poor temporal resolution per sample.

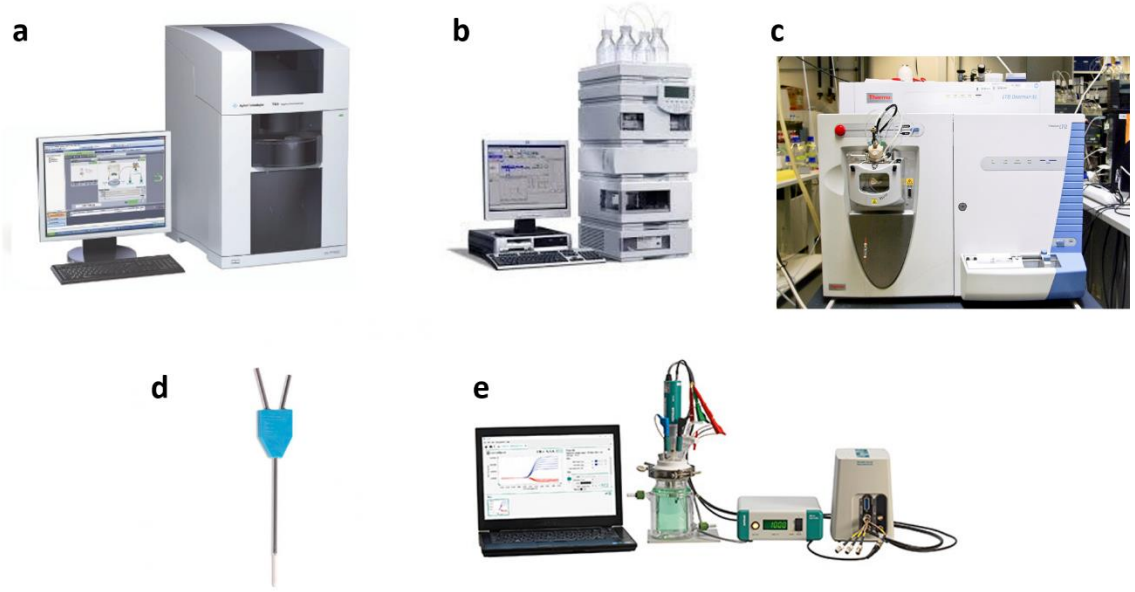

Figure 1.3 a) Capillary electrophoresis; b) HPLC; c) mass spectrometry; d) microdialysis probe; e) potentiostat.

1.2 Organic Electronics

Organic Electronics (OE) is an emerging field of research and technology in which organic semiconductors are employed as active material to transport charges in solid devices. The adjective "organic" refers to the main difference with traditional electronics, which is based on silicon, germanium, metal and metal oxides, instead of carbon-based conductive polymers.

The first breakthrough for OE was the development in 1977 of conjugated polymers in which the doping process was well controlled.[19] This discovery allowed new applications in organic materials, culminating

with the assignment of Nobel Prize to Alan J. Heeger, Hideki Shirakawa and Alan MacDiramid in 2000 “for the discovery and development of conductive polymers”.

The development of OE started with the first Organic Field Effect Transistor (OFET) based on polythiophene in 1986,[20] the first Organic Photovoltaic Cell (OPV)[21] and the first Organic Light Emitting Diode (OLED).[22]

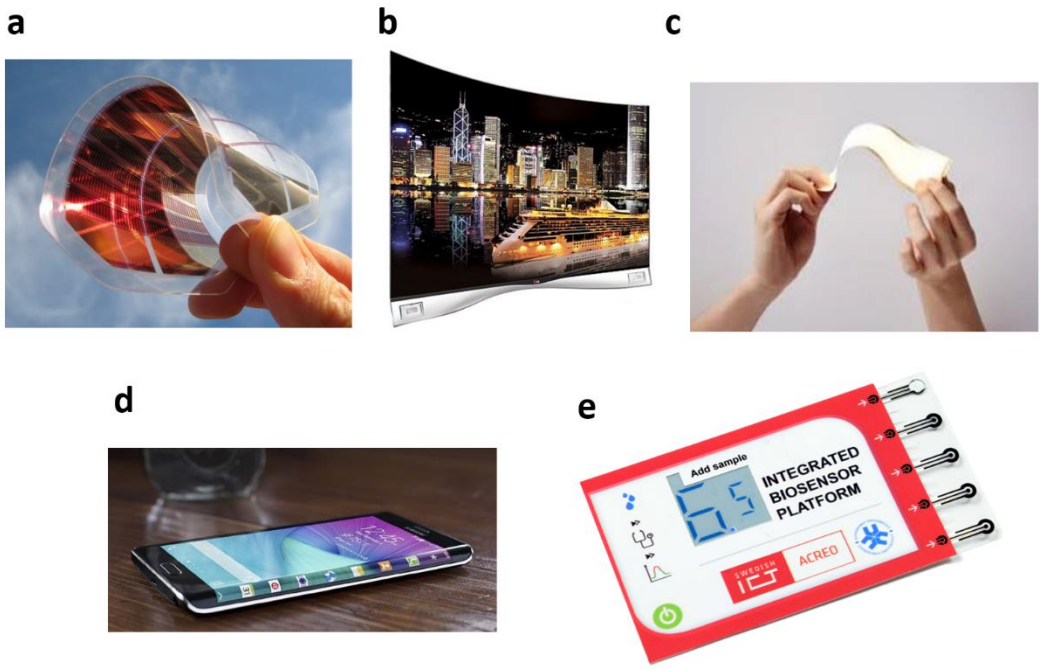

Figure 1.4 a) Organic Photovoltaic Cell on plastic films; b) curved OLED screen (LG electronics); c) flexible light source with OLED white light; d) OLED touch screen of a smartphone (Samsung); e) integrated printed organic electronics biosensor platform (RISE Acreo).

In the last three decades, OE had a growth in the performances of the devices and in the applications (examples of applications are showed in Figure 1.4), but it is still less efficient than the traditional electronics. The advantages of OE, with respect to the traditional silicon-based electronics are the fabrication of devices on a large scale with low costs, the possibility to tune the materials through molecular design and the possibility to use flexible and biodegradable substrates.[23]

1.2.1 Organic Bioelectronics

Organic bioelectronics is an emerging field in which soft materials interface with biology, merging Biology and OE; the resulting devices combine electronics to life science and/or healthcare (i.e. glucose monitors, pacemakers, neural implants).[24–26]

OE has lot of potentialities in this field with respect to the traditional silicon-based electronics, thanks to the possibility to tune the materials in order to exhibit the desired flexibility, elasticity, morphology and

stability. Moreover, OE is able to conduct ions, in addition to electrons and holes, opening a new channel of communication with biology.[27–29] Finally, organic electronics materials are based on Van der Waals interactions, that permits contacts with electrolytes, that are a very important part of the biological world.

1.2.2 Sensors and organic electronic sensors

The International Union of Pure and Applied Chemistry (IUPAC) defines a chemical sensor as *"a device that transforms chemical information […] into an analytically useful signal."* A schematic representation of a sensor is showed in Figure 1.5: a sensor recognized an analyte into a sample through a receptor, that is a part of the sensor in which the chemical reaction takes place; the energy of the chemical reaction is measured by the transducer, that convert the reaction energy into a useful analytical signal. [30]

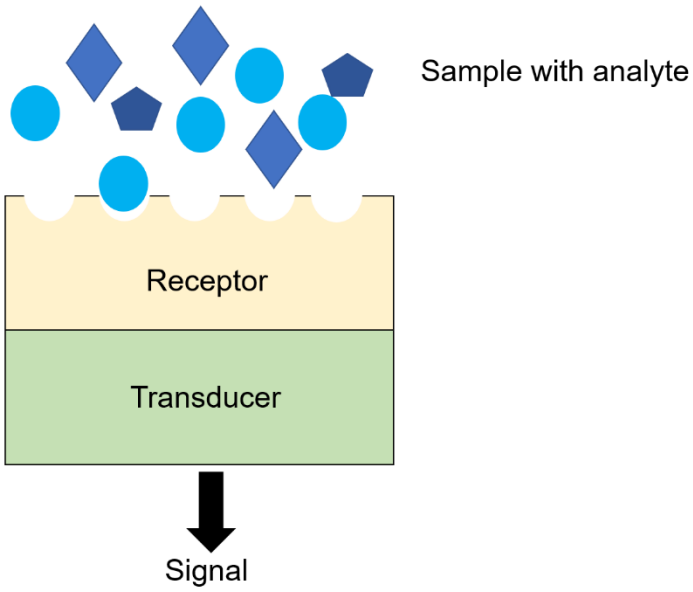

Figure 1.5: schematic representation of a sensor.

An ideal sensor should have:

- high selectivity, that is the capability of the sensor to discriminate a certain analyte into a sample;
- stability of the device in ambient conditions and to the stress of different cycles of measurements;
- a strong calibration method, that permits to evaluate the magnitude of the response to the analyte in comparison to a standard;
- quick response;
- low-cost of fabrication;
- portability;

- limit of detection, LOD, defined as the smallest detected signal over three standard deviations of the blank, and limit of quantification, LOQ, defined as the smallest detected signal over ten standard deviations of the blank, suitable with the analyte concentration in the sample.

Organic electronics, also thanks to the use of conducting polymers, is a good candidate to achieve this goals.[31,32]

In general, organic electronics permits to use different configurations, in order to pursue the aim: organic field effect transistors (OFETs) and electrolyte gated field effect transistors (EGOFETs) have been used with label free configurations or with specific recognition elements to sense different analytes (*i.e.* gas[33], metabolites[34], virus[35], proteins[36], etc.).

1.2.3 Organic electronics for dopamine sensing

OE is looking for alternatives to traditional sensing measurements for catecholamines. Few papers address DA detection with OE devices, most of them follow the trail of traditional sensing through electrochemical measurements: all these works are based on electrochemical microcells with a working electrode covered with PEDOT:PSS; performing cyclic voltammetry and differential pulse voltammetry, it is possible to distinguish DA from UA and AA, reaching a LOD of tens of µM.[37,38] Tybrandt *et al.* performed fast scan cyclic voltammetry, sensing 1 µM of DA.[39]

Organic electronic electrodes can be used *in vivo* performing electrochemical measurements, as described in the work of Wightman, the detection of DA was performed in the striatum with a carbon electrode covered with Nafion™. Nafion™ is a polymer that forms a cation selective structure, inhibiting the diffusion of the anions on the electrode surface. Nevertheless the detection limit is 30 nM in the extracellular fluid of caudate nucleus.[40]

Other works are based on Organic Electrochemical Transistors (OECTs) with channel covered with PEDOT:PSS, the minimum detection of DA reached is 5 nM.[13,41,42]

Casalini *et al.* in 2013 exploited an Electrolyte-Gated Field-Effect Transistor (EGOFET) with a gold working electrode on which are deposited self-assembled monolayer of cysteamine and 4-phormylphenyl boronic acid. DA and boronic acid do an esterification that changes the transconductance of the EGOFET, allowing the detection of DA down to the pM range. The non-oxidative approach allows the sensor to detect DA in presence of AA, because AA does not undergoes to esterification.[34]

Finally, biosensors used for DA detection exploit the tyrosinase, a multi-copper functional oxidoreductase. The presence of the enzyme reduces the problems of interference with other molecules present in biological fluids, however, the immobilization of the enzyme on organic polymers is challenging.[43]

1.2.4 Our strategy

Our detection strategy is based on two PEDOT:PSS electrodes directly patterned on a PDMS substrate. One of the electrodes is pulsed with a train of voltage square waves, while on the other electrode is measured the displacement current. From the current it is possible to extract a characteristic relaxation time τ, that is related to the concentration and the type of analyte in the solution. Thanks to this new method of sensing, the different catecholamines are well resolved, also in mixed solutions. Moreover the employment of biocompatible, flexible and transparent materials made the sensor a good candidate to implant and perform real time and *in vivo* measurements.

References

(1) Schwerdt, H. N.; Shimazu, H.; Amemori, K.; Amemori, S.; Tierney, P. L.; Gibson, D. J.; Hong, S.; Yoshida, T.; Langer, R.; Cima, M. J.; et al. Long-Term Dopamine Neurochemical Monitoring in Primates. *Proc. Natl. Acad. Sci.* **2017**, *114* (50), 13260–13265. https://doi.org/10.1073/pnas.1713756114.

(2) Schmalfuss, H. Tyramine Und Oxytyramin, Blutdrucksteigermde Schwarzvorstufen Des Beseginsters Sarothamnus Scoparius WIMM. *Biochem. Zeitrschr.* **1931**, *236*, 226–230.

(3) Blaschko, H. The Activity of l (-)-Dopa Decarboxylase. *J. Physiol.* **1942**, *101* (3), 337–349. https://doi.org/10.1113/jphysiol.1942.sp003988.

(4) Hornykiewicz, O. Dopamine Miracle: From Brain Homogenate to Dopamine Replacement. *Mov. Disord.* **2002**, *17* (3), 501–508. https://doi.org/10.1002/mds.10115.

(5) Carlsson, A. A Half-Century of Neurotransmitter Research: Impact on Neurology and Psychiatry (Nobel Lecture). *ChemBioChem* **2001**, *2* (7–8), 484–493. https://doi.org/10.1002/1439-7633(20010803)2:7/8<484::AID-CBIC484>3.0.CO;2-5.

(6) Blaschko, H. The Specific Action of L-DOPA Decarboxylase. *J. Physiol.* **1939**.

(7) Meiser, J.; Weindl, D.; Hiller, K. Complexity of Dopamine Metabolism. *Cell Commun. Signal.* **2013**, *11* (1), 34. https://doi.org/10.1186/1478-811X-11-34.

(8) Napolitano, A.; Manini, P.; D'Ischia, M. Oxidation Chemistry of Catecholamines and Neuronal Degeneration: An Update. *Curr. Med. Chem.* **2011**, *18* (12), 1832–1845. https://doi.org/10.2174/092986711795496863.

(9) Olanow, C. W.; Prusiner, S. B. Is Parkinson's Disease a Prion Disorder? *Proc. Natl. Acad. Sci.* **2009**, *106* (31), 12571–12572. https://doi.org/10.1073/pnas.0906759106.

(10) De Deurwaerdère, P.; Di Giovanni, G.; Millan, M. J. Expanding the Repertoire of L-DOPA's Actions: A Comprehensive Review of Its Functional Neurochemistry. *Prog. Neurobiol.* **2017**, *151*, 57–100. https://doi.org/10.1016/j.pneurobio.2016.07.002.

(11) Oertel, W.; Schulz, J. B. Current and Experimental Treatments of Parkinson Disease: A Guide for Neuroscientists. *J. Neurochem.* **2016**, *139*, 325–337. https://doi.org/10.1111/jnc.13750.

(12) Zhang, Q.; Gong, M. On-Line Preconcentration of Fluorescent Derivatives of Catecholamines in Cerebrospinal Fluid Using Flow-Gated Capillary Electrophoresis. *J. Chromatogr. A* **2016**, *1450*, 112–120. https://doi.org/10.1016/j.chroma.2016.04.080.

(13) Tang, H.; Lin, P.; Chan, H. L. W.; Yan, F. Highly Sensitive Dopamine Biosensors Based on Organic Electrochemical Transistors. *Biosens. Bioelectron.* **2011**, *26* (11), 4559–4563. https://doi.org/10.1016/j.bios.2011.05.025.

(14) Chan, E. C. .; Wee, P. .; Ho, P. .; Ho, P. . High-Performance Liquid Chromatographic Assay for Catecholamines and Metanephrines Using Fluorimetric Detection with Pre-Column 9-Fluorenylmethyloxycarbonyl Chloride Derivatization. *J. Chromatogr. B Biomed. Sci. Appl.* **2000**, *749* (2), 179–189. https://doi.org/10.1016/S0378-4347(00)00423-0.

(15) Robinson, D. L.; Venton, B. J.; Heien, M. L. A. V; Wightman, R. M. Detecting Subsecond Dopamine Release with Fast-Scan Cyclic Voltammetry in Vivo. *Clin. Chem.* **2003**, *49* (10), 1763–1773. https://doi.org/10.1373/49.10.1763.

(16) Hawley, M. D.; Tatawawadi, S. V; Piekarski, S.; Adams, R. N. Electrochemical Studies of the Oxidation Pathways of Catecholamines. *J. Am. Chem. Soc.* **1967**, *89* (2), 447–450. https://doi.org/10.1021/ja00978a051.

(17) Kissinger, P. T.; Hart, J. B.; Adams, R. N. Voltammetry in Brain Tissue — a New Neurophysiological Measurement. *Brain Res.* **1973**, *55* (1), 209–213. https://doi.org/10.1016/0006-8993(73)90503-9.

(18) Ribeiro, J. A.; Fernandes, P. M. V.; Pereira, C. M.; Silva, F. Electrochemical Sensors and Biosensors for Determination of Catecholamine Neurotransmitters: A Review. *Talanta* **2016**, *160*, 653–679. https://doi.org/10.1016/j.talanta.2016.06.066.

(19) Chiang, C. K.; Fincher, C. R.; Park, Y. W.; Heeger, A. J.; Shirakawa, H.; Louis, E. J.; Gau, S. C.; MacDiarmid, A. G. Electrical Conductivity in Doped Polyacetylene. *Phys. Rev. Lett.* **1977**, *39* (17), 1098–1101. https://doi.org/10.1103/PhysRevLett.39.1098.

(20) Tsumura, A.; Koezuka, H.; Ando, T. Macromolecular Electronic Device: Field-effect Transistor with a Polythiophene Thin Film. *Appl. Phys. Lett.* **1986**, *49* (18), 1210–1212. https://doi.org/10.1063/1.97417.

(21) Tang, C. W. Two-layer Organic Photovoltaic Cell. *Appl. Phys. Lett.* **1986**, *48* (2), 183–185. https://doi.org/10.1063/1.96937.

(22) Tang, C. W.; VanSlyke, S. A. Organic Electroluminescent Diodes. *Appl. Phys. Lett.* **1987**, *51* (12), 913–915. https://doi.org/10.1063/1.98799.

(23) Liao, C.; Mak, C.; Zhang, M.; Chan, H. L. W.; Yan, F. Flexible Organic Electrochemical Transistors for Highly Selective Enzyme Biosensors and Used for Saliva Testing. *Adv. Mater.* **2015**, *27* (4), 676–681. https://doi.org/10.1002/adma.201404378.

(24) Simon, D. T.; Gabrielsson, E. O.; Tybrandt, K.; Berggren, M. Organic Bioelectronics: Bridging the

Signaling Gap between Biology and Technology. *Chem. Rev.* **2016**, *116* (21), 13009–13041. https://doi.org/10.1021/acs.chemrev.6b00146.

(25) Owens, R. M.; Malliaras, G. G. Organic Electronics at the Interface with Biology. *MRS Bull.* **2010**, *35* (6), 449–456. https://doi.org/10.1557/mrs2010.583.

(26) Rivnay, J.; Owens, R. M.; Malliaras, G. G. The Rise of Organic Bioelectronics. *Chem. Mater.* **2014**, *26* (1), 679–685. https://doi.org/10.1021/cm4022003.

(27) Tarabella, G.; Mahvash Mohammadi, F.; Coppedè, N.; Barbero, F.; Iannotta, S.; Santato, C.; Cicoira, F. New Opportunities for Organic Electronics and Bioelectronics: Ions in Action. *Chem. Sci.* **2013**, *4* (4), 1395. https://doi.org/10.1039/c2sc21740f.

(28) deMello, J. C. What's in a Name? *Nat. Mater.* **2007**, *6* (11), 796–797. https://doi.org/10.1038/nmat2043.

(29) Leger, B. J. M. Organic Electronics : The Ions Have It **. **2008**, *1700*, 837–841. https://doi.org/10.1002/adma.200701874.

(30) Hulanicki, A.; Glab, S.; Ingman, F. Chemical Sensors: Definitions and Classification. *Pure Appl. Chem.* **1991**, *63* (9), 1247–1250. https://doi.org/10.1351/pac199163091247.

(31) Torsi, L.; Magliulo, M.; Manoli, K.; Palazzo, G. Organic Field-Effect Transistor Sensors: A Tutorial Review. *Chem. Soc. Rev.* **2013**, *42* (22), 8612. https://doi.org/10.1039/c3cs60127g.

(32) Garcia-Brejo, E.; Gomez-Lor Perez, B.; Cosseddu, P. *Organic Sensors*; Institution of Engineering and Technology, 2016.

(33) Yu, J.; Yu, X.; Zhang, L.; Zeng, H. Ammonia Gas Sensor Based on Pentacene Organic Field-Effect Transistor. *Sensors Actuators B Chem.* **2012**, *173*, 133–138. https://doi.org/10.1016/j.snb.2012.06.060.

(34) Casalini, S.; Leonardi, F.; Cramer, T.; Biscarini, F. Organic Field-Effect Transistor for Label-Free Dopamine Sensing. *Org. Electron. physics, Mater. Appl.* **2013**, *14* (1), 156–163. https://doi.org/10.1016/j.orgel.2012.10.027.

(35) Berto, M.; Vecchi, E.; Baiamonte, L.; Condò, C.; Sensi, M.; Di Lauro, M.; Sola, M.; De Stradis, A.; Biscarini, F.; Minafra, A.; et al. Label Free Detection of Plant Viruses with Organic Transistor Biosensors. *Sensors Actuators B Chem.* **2019**, *281*, 150–156. https://doi.org/10.1016/j.snb.2018.10.080.

(36) Diacci, C.; Berto, M.; Di Lauro, M.; Bianchini, E.; Pinti, M.; Simon, D. T.; Biscarini, F.; Bortolotti, C. A. Label-Free Detection of Interleukin-6 Using Electrolyte Gated Organic Field Effect Transistors. *Biointerphases* **2017**, *12* (5), 05F401. https://doi.org/10.1116/1.4997760.

(37) Belaidi, F. S.; Civélas, A.; Castagnola, V.; Tsopela, A.; Mazenq, L.; Gros, P.; Launay, J.; Temple-Boyer, P. PEDOT-Modified Integrated Microelectrodes for the Detection of Ascorbic Acid, Dopamine and Uric Acid. *Sensors Actuators B Chem.* **2015**, *214*, 1–9. https://doi.org/10.1016/j.snb.2015.03.005.

(38) Gualandi, I.; Tonelli, D.; Mariani, F.; Scavetta, E.; Marzocchi, M.; Fraboni, B. Selective Detection of Dopamine with an All PEDOT:PSS Organic Electrochemical Transistor. *Sci. Rep.* **2016**, *6* (October), 35419. https://doi.org/10.1038/srep35419.

(39) Tybrandt, K.; Kollipara, S. B.; Berggren, M. Organic Electrochemical Transistors for Signal Amplification in Fast Scan Cyclic Voltammetry. *Sensors Actuators, B Chem.* **2014**, *195*, 651–656. https://doi.org/10.1016/j.snb.2014.01.097.

(40) Wightman, R. M.; May, L. J.; Michael, a C. Detection of Dopamine Dynamics in the Brain. *Anal. Chem.* **1988**, *60* (13), 769A-779A. https://doi.org/10.1021/ac00164a001.

(41) Liao, C.; Zhang, M.; Niu, L.; Zheng, Z.; Yan, F. Organic Electrochemical Transistors with Graphene-Modified Gate Electrodes for Highly Sensitive and Selective Dopamine Sensors. *J. Mater. Chem. B* **2014**, *2* (2), 191–200. https://doi.org/10.1039/C3TB21079K.

(42) Gualandi, I.; Marzocchi, M.; Achilli, A.; Cavedale, D.; Bonfiglio, A.; Fraboni, B. Textile Organic Electrochemical Transistors as a Platform for Wearable Biosensors. *Sci. Rep.* **2016**, *6* (August), 33637. https://doi.org/10.1038/srep33637.

(43) Jackowska, K.; Krysinski, P. New Trends in the Electrochemical Sensing of Dopamine. *Anal. Bioanal. Chem.* **2013**, *405* (11), 3753–3771. https://doi.org/10.1007/s00216-012-6578-2.

2 NEUROMORPHIC DEVICES

In this chapter are presented neuromorphic devices from their birth, to the development they had in organic electronics. The different functions they fulfil is compared to the physiological one in the nervous system.

2.1 PHYSIOLOGICAL NEUROMORPHIC FUNCTIONS

Learning and memory are human functions possible thanks to neurons functions. A neuron, or nerve cell, is a cell of nervous system specialized in receiving, elaborating and transmitting electrical and chemical signals. Neurons are the primary functional units of the brain. Each one of them is made up of different parts, sketched in Figure 2.1: *soma*, the body of the cell, that contains organelles and in which metabolic pathways take place, *dendrites*, the branches starting from the soma, which duty is to receive signals from neighboring neurons through the synapses that cover them and *axons*, a specialized part of the neurons dedicated to the transport of information, as action potentials, to the target cells through synapses .[1]

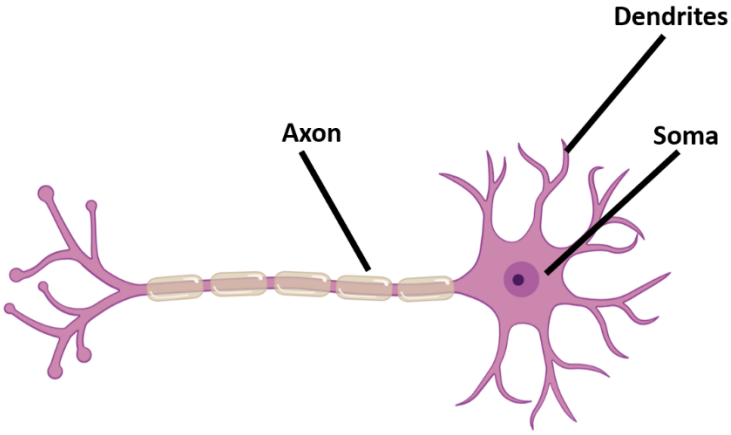

Figure 2.6 Schematic sketch of the different part of a neuron.

Thus, interactions between neurons occur by synapses that ensure brain functionality. Synaptic transmission can happen both electrically and chemically: electrical synapses need the connection between the two cells through gap junctions that ensure the flow of currents, while chemical synapses occur between two adjacent cells. The latter requires a presynaptic cell that regulates the release of neurotransmitters when action potentials arrive to the terminal and a postsynaptic cell with proper receptors that can detect and translate the message into various events (Figure 2.2).[2]

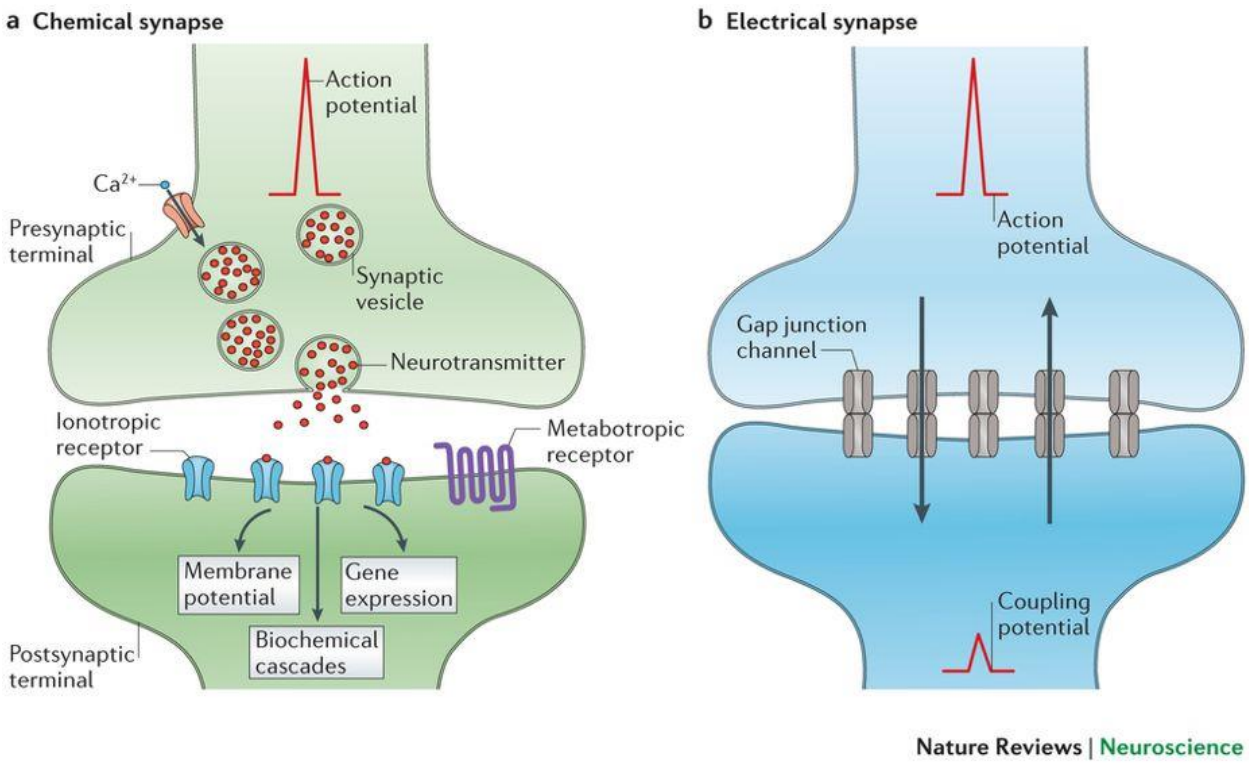

Figure 2.7 Schematic representation of a) chemical and b) electrical synapses. (From: Pereda, Nat Rev Neurosci. 2014[2])

Action potentials are generated when different gradients of ions are present at the two side of the cell membrane. The membrane is a phospholipid bilayer, thus charged molecules cannot pass through it without specific carriers. There are several transmembrane proteins that can help the transport of ions, as active transport pumps and ions channels, that are activated by electrical or chemical signals. These proteins generate a transmembrane potential, regulating the concentration of sodium, potassium and chloride ions. This condition determines a resting membrane potential, V_m, of -65 mV, measured as a potential across the cell membrane. As shown in Figure 2.3, when the cell is resting, the concentration of Na^+ outside the cell is 10 times greater than outside, while K^+ concentration is greater outside the cell, anions are generally part of the inner cell membrane. The action potential begins with a temporary depolarization of the membrane, caused by a sudden flow of Na^+ ions through the channels, that brings the membrane potential to +30 mV, then, after about 2 ms, a counter-flow of K^+ ions repolarizes the membrane.[3]

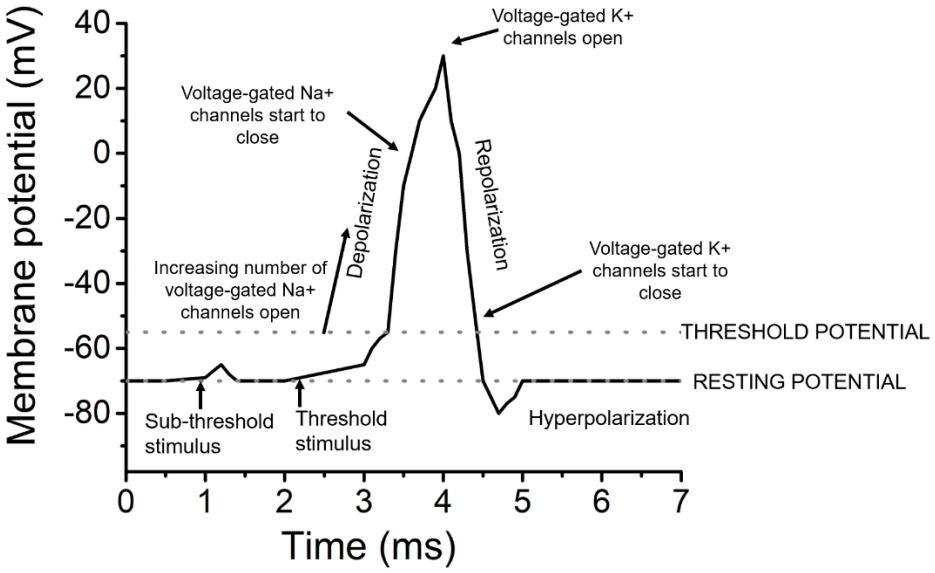

Figure 2.8 Evolution of an action potential.

When the active pre-synaptic cell of a chemical synapse releases neurotransmitters, that bind the post-synaptic cell and evoke an excitatory post-synaptic potential (EPSP) that makes the cell more likely to fire an action potential. Conversely, the outflow of positive charges induces inhibitory post-synaptic potentials (IPSP), thus a decrease of the possibility to fire an action potential. Those mechanisms have additive effect, so series of EPSPs or IPSPs can add up enhancing or diminishing the ability to fire action potentials.[4]

Small and coherent modifications of chemical synapses are the key mechanism of learning and memory; in fact, synapses are not static, but, due to repetitive stimulation, they can potentiate, thus increasing the synaptic strength, making them more effective, or, vice versa, depress, thus decreasing the synaptic strength, making them weaker.[5]

There are different types of memory: long-term memory (LTM), short-term memory (STM) and working memory. LTM consists in the store of knowledge, in this case the potentiation of the synapse lasts days, weeks or years; STM refers to a limited amount of information accessible for a limited time (seconds, minutes or hours); lastly, working memory is used to plan and carry out behavior, but is not completely distinct from STM. The main differences between LTM and STM rely on duration, i.e. information stored in memory decay as a function of time, memory capacity, namely the limit in the number of items that can be memorized, and intracellular modifications.[5,6]

Studies on invertebrates have shown that STM does not requires the synthesis of new proteins, but neurotransmitters activate the synthesis of intracellular messengers that can covalently bind intracellular proteins already present. The modification lasts until the bond lasts. On the other hand, a LTM

requirement is the synthesis of new proteins, that, if are not synthetized anymore cause the deletion of the information stored.

Therefore, is not a clear separation between neurotransmitter that produce STM or LTM, but the synthesis of genes and proteins activated for LTM, distinguish it from STM.[7]

STM can occur in different ways depending on the pre-synaptic train patterns to the post-synaptic neuron: they can change both time duration and frequency and the two resulting mechanisms (i.e. facilitation and depression, shown in figure 2.4) act like a filter for information transmission through neurons.[8] In facilitation mechanism, each subsequent post-synaptic potential (PSP) is higher in magnitude than the previous and the signal plateau occurs after about 100 ms; conversely, depression mechanism operates in the opposite direction of facilitation, thus decreasing the amplitude of PSPs due to the reduction of the releasable vesicles of neurotransmitters.[5]

LTM has been explained in 1981 by the BCM theory (Bienenstock, Cooper, Munro): it proposes a sliding threshold for Long-Term Potentiation (LTP) and Long-Term Depression (LTD) induction. Accordingly, LTP occurs following a high activity state (high frequency pre-synaptic firing), while LTD needs a lower activity state (low frequency pre-synaptic firing). Thus, LTP or LTD can occur both depending on the stimulation protocol applied by the pre-synaptic neuron. Generally, a single facilitation stimulation enhances the synaptic transmission from minutes to hours (STM), while LTM requires more than four stimulations to store memory for more than 24 hours.[7,9,10] Long-term changes at the basis of learning and memory can be assessed by spike-timing-dependent plasticity (STDP). The general paradigm of STDP is *"neurons wire together if they fire together"* [11], therefore if there is a more or less simultaneous response between pre- and post-synaptic neuron, it is possible to assume that there is a common cause for firing and so an increase of the synapse weight, defined as the depolarization peak produced at the soma.[12] The distinction between LTP or LTD depends on three factors:

i. The synchronization between pre and post-synaptic spikes;
ii. The dendritic and axonal propagation delays;
iii. The number of paired spikes.

In a canonical STDP, a pre-synaptic spike followed by a post-synaptic response in a time window of about 20 ms leads LTP, conversely, in a time window of 20-100 ms it leads to LTD.[10,13–15]

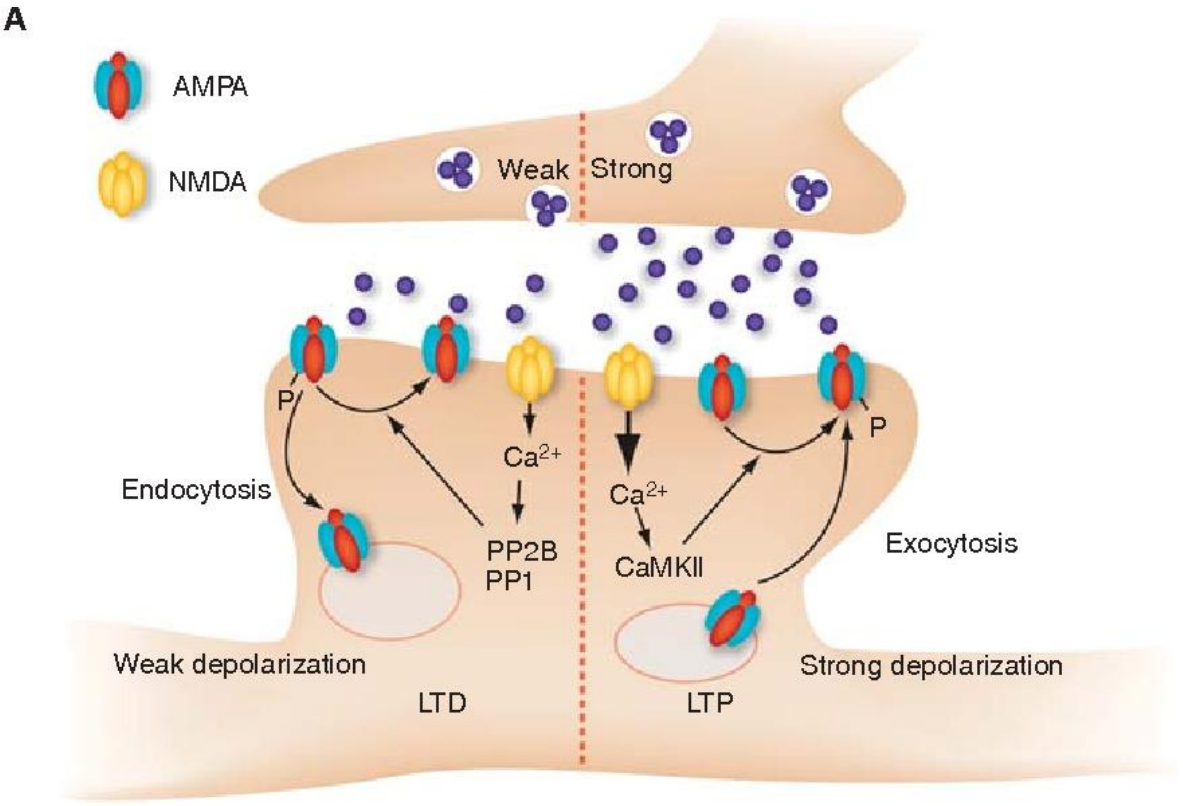

Figure 2.4 Postsynaptic expression mechanisms of LTP and LTD. Weak activity of the presynaptic neuron leads to modest depolarization, while strong activity paired with strong depolarization triggers LTP. (From: Lüscher et al. "Depression (LTP/LTD) NMDA Receptor-Dependent Long-Term Potentiation and Long-Term." (2012)).

2.2 History of Neuromorphic Devices

The term "Neuromorphic Electronic System" was coined by Carver Mead [16] in 1990 to envision a new paradigm in digital technologies. Since biological system could manage complex data processing in an extremely more effective way than silicon-based devices in terms of energy consumption, interconnectivity between single computation units (neurons and synapses in the brain, transistors in a chip) and ability to adapt and learn, Mead proposed to mimic brain functionality with digital systems. In the 1990 paper, Mead tried to describe his idea for future application of CMOS technologies in bio-mimetism of the brain, but that remained just an ideal future for several years. A similar destiny has occurred to the "Memristor", the circuit element theorized by Chua[17] in 1971, tested several times from 1979 by the work of Potember *et al.*[18] and demonstrated experimentally only in 2008 by Strukov and co-workers[19]: memristors (a contraction of memory resistors) are devices characterized by a variable (non-volatile) electrical resistance, which depends on the memorized history of the device, in terms of applied electrical stress (voltage and current).[20] The demonstration of the memristor together with the work by Chua and co-worker on silicon transistor synapses paved the way to the realization of neural network

algorithms and artificial synaptic functionality through hardware elements, thus no more limited to software implementation.

Moving from silicon to carbon-based technology, some of the first proposed devices exploited a controlled variation of electrical conductivity of allotropes of carbon, due to electrical or optical stimulation (or a combination of opto-electronic stimuli).[21–24] In particular, in 2004, Singh and co-workers demonstrated the possibility to use organic field-effect transistors with polymeric dielectric and fullerenes as active material as non-volatile memory devices[21]: in the proposed working mechanism, charges are trapped in the dielectric layer upon gate voltage application, resulting in a large metastable hysteresis in the drain current. The output current can be read as information with a longer retention time of hours. The combination of carbon nanotubes with light-sensitive polymers in transistor architectures has been shown to be good strategy to produce opto-electronic memory devices. [22,25] Two strategies are reported: in the first one, showed in Figure 2.4 a, information (i.e. electric charges that are created at the interface between polymer and CNT) can be written upon UV illumination and stored in the nanotubes even for 16 hours, while read and erase processes are performed through application of a voltage potential across the channel;[25] in the second one, showed in Figure 2.4 b, information is written in the form on electrical charges created upon visible laser illumination (from 476 to 647 nm), but a constant gate voltage application is needed to store information or to erase it. The work showed that the time needed for relaxation of the stored charges is strongly dependent to the gate voltage applied.[22] Those strategies have demonstrated that varying the coating polymer, it is possible to change the wavelength, thus the energy, needed to write information.

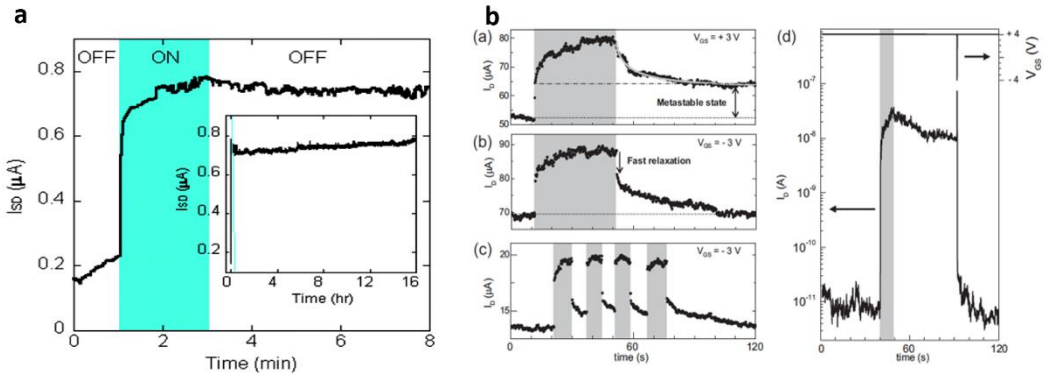

Figure 2.9: different strategies to write information. a) the device is illuminated with UV light and record the information, then, also with light off, the information is retained. (From: Star et al., Nano Letters, 2004)[25] b) laser illumination added to constant gate voltage to store or to erase memory.(From Borghetti, Advanced Materials, 2006)[22]

The combination of metal nanocluster and organic polymers have been exploited to build memory devices.[26,27] In particular, three-layered and two-layered architectures have shown similar characteristics

in term of electrical performances and proposed working mechanism even though based on different materials: in the work of Ma, a thin aluminum layer is embedded within the organic material (i.e. 2-amino-4,5-imidazoledicarbonitrile), as the active medium and connected with two Al electrodes, while Tondelier and co-worker used a single pentacene layer as active material between two Al electrodes. Those devices work as memory elements thanks to their capability to operate with two different conductive states at the same applied potential; in particular, their conductivities differ by several orders of magnitude and once the devices reach either state, they tend to remain in the state for a long period of time, showing a good stability.

The two states (viz. high and low conductivity) can be selected controlling the applied potential: in the work of Ma, application of positive or negative potentials changes in a reversible way the redox state of the polymer from an high conductivity state (ON state) to a low conductivity state (OFF state) and vice-versa.[26] To obtain the same result, Tondelier exploited the Al nanoparticles included in pentacene during the deposition of the electrodes: application of potentials causes a switching to the ON state (high conductivity) due to the formation of a nano-filamentary metallic pathways through the pentacene layer, while the switch off of the potential drive the relaxation of nanoparticles and the return of the device to the OFF state (low conductivity).[27]

Three-terminal architectures (transistors or transistors-like) has been used to demonstrate the feasibility to tune electrical characteristics of organic devices through reversible redox properties of conductive polymers in order to obtain writable and erasable memory systems, as shown in Figure 2.5. The work of Kaneto *et al.*[28] demonstrated a device, whose conductance can be tuned electrochemically, based on three electrodes, a redox conductive polymer (i.e. poly(3-methyltiophene)) and a solid electrolyte between the gate electrode and the conductive layer. This strategy was later demonstrated by Nilsson *et al.*[29] in 2002 using PEDOT:PSS as active material and polyelectrolyte gel in a transistor configuration, and in 2005 by Erokhin *et al.*[30] with a three-electrodes device based on HCl p-doped polyaniline (PANI) conducting polymer interfaced with $LiClO_4$/poly(ethylene oxide) solid electrolyte.

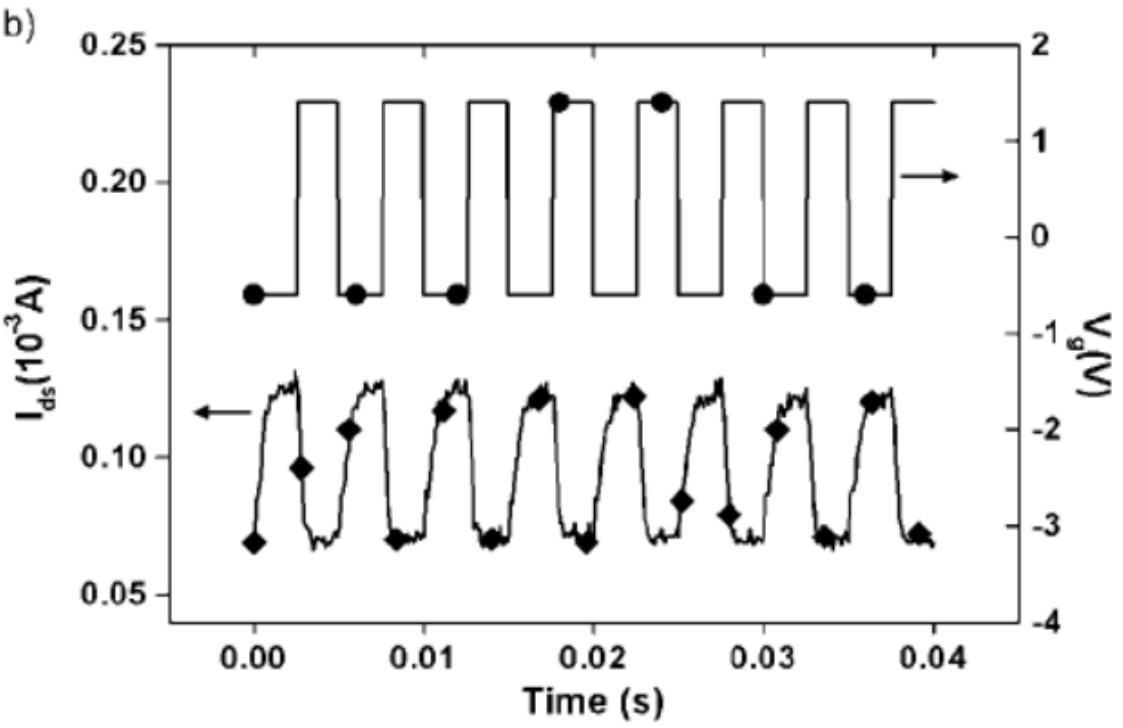

Figure 2.10 example of a bi-stable three-terminal device.(From: Nilsson, Advanced Materials, 2002)[29]

The work of Tondelier showed the potentialities of hybrid metal/organic devices as memory elements and this concept was demonstrated with two strategies based on pentacene-based organic transistors: in 2004, Schroeder *et al.*[31] realized a memory cell, the so-called FerrOFET, with pentacene transistor in which the gate insulator was nylon poly(m-xylene adipamide, a ferroelectric-like polymer; in 2008 Novembre *et al.*[32] showed the result obtained embedding gold nanoparticles in the pentacene layer of an organic transistor. In both works, the effect of ferroelectric-like layer[31] or metal particles[32] is a controlled modulation of the electrical behavior of the transistor, in terms of hysteresis in the current response, threshold voltage shift and ON/OFF ratio. Writing and erasing processes are done with the application of DC voltages[31] or pulsed voltages at the gate electrode.[32]

All the works reported are attempts to realize non-volatile memory elements based on those previous demonstration, the group of Fontana[33] and Vuillaume[34] proposed the first example of organic electronic devices driven to mimic synaptic behaviors.

2.3 ORGANIC NEUROMORPHIC DEVICES

2.3.1 Excitatory Post-Synaptic Current (EPSC)

Excitatory Post-Synaptic Current (EPSC) is one of the most mimicked synaptic function with organic neuromorphic devices. Generally one of the electrodes acts as a pre-synaptic neuron being triggered with a stimulus that drive ions in the electrolyte at the interface between the organic semiconductor and the dielectric. The ions behave as neurotransmitters in the synaptic cleft and produce a current response, that is typically measured as a current in the channel and mimics the response of the post-synaptic neuron. Once the stimulus ends, ions return to the equilibrium state through an exponential decay that can be fitted with a stretched exponential, shown in Equation 2.1:

$$I = I_0 \exp -\left(\frac{t}{\tau}\right) + I_\infty \tag{2.1}$$

In which I_0 is the maximum current, I_∞ is the current value at the plateau, t is the time and τ is the characteristic relaxation time of the system, in which ions return to the equilibrium, and represents also the period in which the device stores the information.

Different strategies have been used to trigger the pre-synaptic electrode, especially using light[35] or applied voltage potentials to the gate electrode.[36–39]

In 2012 Alibart *et al.* firstly simulated EPSC using a pseudo-two terminal device based on a transistor with drain and gate electrodes short-circuited, with a channel of pentacene with gold nanoparticles embedded; in this work, a voltage stimulus of -35 V was applied to the drain electrode and at the source electrode was measured the resulting current. As shown in Figure 2.6, the current response of the device has a decaying evolution.[40]

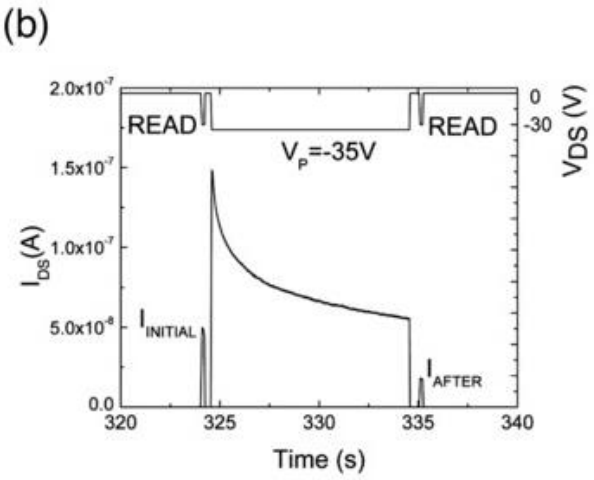

Figure 2.11 Simulation of a EPSC spike.(From: Alibart et al., Adv. Funct. Mater. 2012 [40])

In transistor-based devices, the gate simulates the pre-synaptic neuron, the channel between source and drain the post-synaptic neuron and the electrolytic solution, through which ions migrate, simulates the synaptic cleft. Applying a spike of voltage to the gate and a constant voltage to the drain it is possible to mimic the EPSC characteristic trend, due to the migration of ions in the electrolyte.[36–39]

Dai *et al.* in 2018 used UV light to mimic the pre-synaptic neuron: the device was an organic field-effect transistor (OFET), in which poly-acrylonitrile (PAN) was used as a dielectric. Polar groups of PAN interacted with the organic semiconductor 2,7-diocty[1benzothieno[3,2-b]benzotiophene] (C8-BTBT). Light, coupled with a V_G = 2 V, induced a current that behaved like an EPSC. UV-light generated electron-hole pairs in C8-BTBT channel and at the interface C8-BTBT/PAN the charge trap states were filled by the holes introduced by the light. Once the stimulus ended the holes were gradually de-trapped.[35]

In 2018 Lee *et al.* Fabricated a stretchable organic nanowire synaptic transistor (s-ONWST) in which a light source stimulated the gate, that acted as a pre-synaptic neuron, generating an EPSC, measured as a current in the channel.[41]

In all the works, the pre-synaptic stimulus duration was extended in order to evaluate if there would be a growth in the output current: as a response, current increased linearly with the increase of the duration of the stimulus until it reached a saturation and, in this case, even if the stimulus continued, the current did not increase, because of the saturation of the charge-trapping sites.

2.3.2 Long-Term Memory (LTM)

The enabling of Long-Term Memory (LTM) in organic electronic devices cannot be evaluated as in physiology with the strengthen of a certain circuitry of the synapses, so, potentiation and depression are evaluated as numbers, generally identified by the amplitude of the measured current evoked by the pre-

synaptic terminal,[38,41,42] by the change of conductance of the active material [39,43] or both.[44] The change of the conductance is a consequence of irreversible changes of morphological structure of the active device, due to a certain train of voltage pulses.

Gerasimov *et al.* with an Organic Electrochemical Transistor (OECT) with poly sodium 4-(2-(2,5-bis(2,3-dihydrothienol[3,4-b][1,4]dioxin-5-yl)thiophen-3-yl)ethoxy)butane-1-sulfonate (PETE) observed that LTM was enabled after irreversible modification of the self-doped polymer; in particular, LTP occurred by electro-polymerization, while LTP by the over-oxidation of it (Figure 2.7).[45]

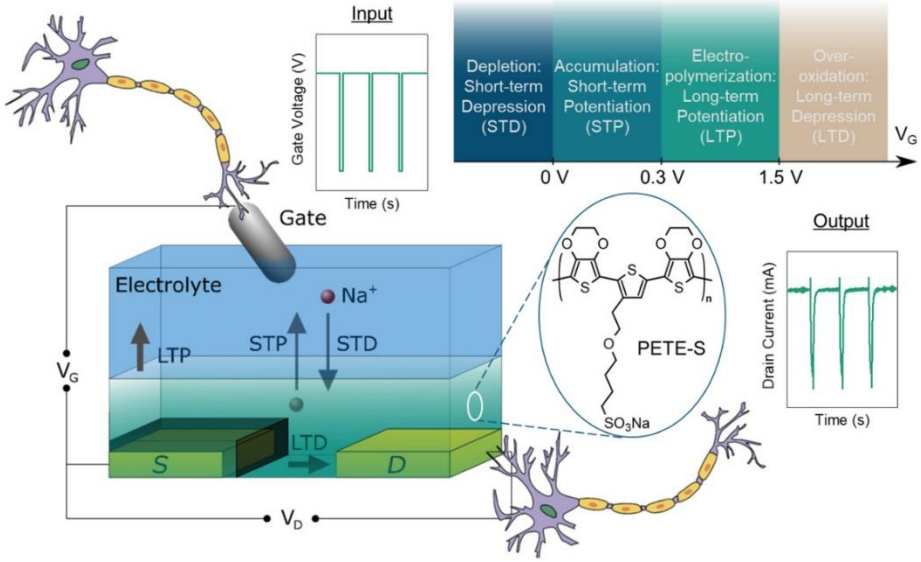

Figure 2.12 Explanation of the mechanisms that make the device able to mimic STM and LTM (From: Gerasimov et al., Adv. Sci., 2019 [45])

As demonstrated by Gkoupedenis *et al.* in 2015 using a poly(3,4-ethylendioxy-tiophene):poly(tetrahydofuran (PEDOT:PTHF) device, LTM was induced through specific pattern of positive and negative potentials that modify the morphology of the active material and consequently the conductivity of the device, that varies as a function of the voltage pulses. They saw that outdistanced training pulses did not enable LTM, conversely a train of close pulses did. To demonstrate the permanent change in the PEDOT:PTHF they applied single pulses, in order to simulate an EPSC, and the current returned to the state set after LTM training and not to the initial one, demonstrating that brief stimulations do not affect the memory of the device.[38]

In the works of Battistoni and Xu was observed that the application of few random stimuli did not affect the conductive state of the device, that, after the stimulation, returned in the initial state of current, demonstrating that the device did not memorized anything. Conversely, was observed depressing or facilitating behavior after a tight and precise training through the pre-synaptic terminal. [42,46]

Van de Burgt *et al.* in 2017 and in 2019, using a PEDOT:PSS/PEI (poly(ethylenimine)) device, demonstrated an artificial synapse that exhibited more than 500 non-volatile reproducible states of LTM that, once programmed, retained the memorized levels even after 30 days after encapsulation of the device. The induction of LTM occurred applying a positive pre-synaptic potentials to PEDOT:PSS electrode, enabling the flow of cations into the post-synaptic terminal, resulting in a protonation of the amine group of PEI, that reduced the conductivity. The reaction was reversible applying negative voltage pulses. All the changes were monitored by the variation of conductance (Figure 2.8).[39,47]

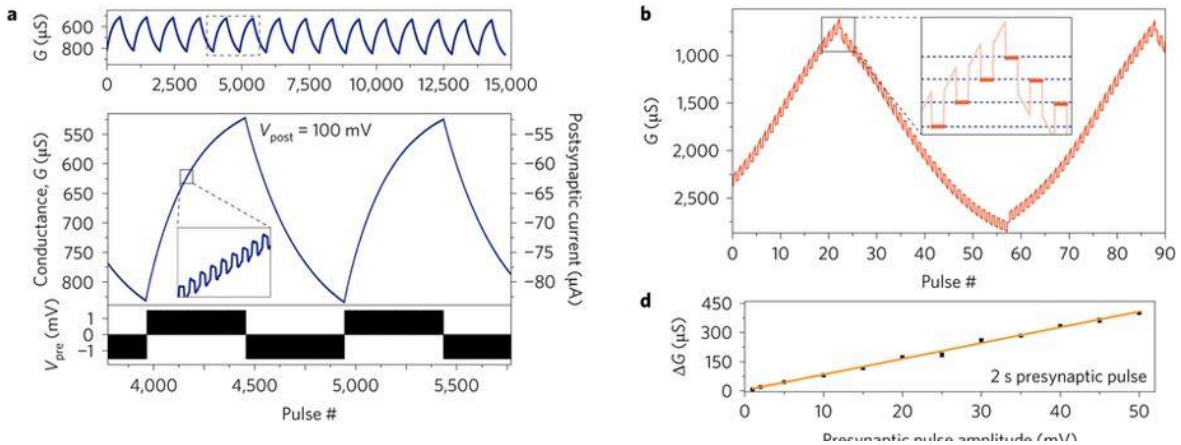

Figure 2.13 Induction of LTM in PEDOT:PSS/PEI devices and the exhibition of the 500 non-voltatile states of memory. (From: van de Burgt et al., Nat. Com., 2017 [39])

2.3.3 Short-Term Memory (STM)

Short-Term memory (STM) is the ability of organic electronic devices to retain memory from few to thousands seconds. Application of a particular training of voltage pulses to the pre-synaptic terminal enables potentiation or depression in the post-synaptic terminal. It is called potentiation the behavior of the artificial synapse in which the output signal has an increasing trend, while it is called depression when the output signal has a decaying trend. The output signal can be fitted, as well as ESPC, with the Equation 2.1, where τ represents the relaxation time of the system.

STP behavior is induced by the voltage pulses applied to the pre-synaptic terminal that push the ions flowing into the semiconductor. When the pre-synaptic pulse ends ions return into the electrolyte, if the frequency of pulsing of the pre-synaptic electrode is high, the system does not have the time to return completely at the initial state, and so, the subsequent pulse does not generate a current as high as the previous, conversely, if the frequency is low the current will have an increase.

This is the equivalent of the biological process: in fact, in each synapse there is a finite amount of neurotransmitters available, that need a certain time to recover after discharge. The recover occurs in a

characteristic time τ, so in neuromorphic devices, as well as in biological synapses, if the spiking frequency is lower than τ^{-1} the release of neurotransmitters will be the same or larger; on the contrary, if it is larger, the second spike will be smaller than the previous one, because the amount of neurotransmitters available is not complete.

The group of Vuillaume in 2010 firstly designed the protocol to induce STP in organic electronic neuromorphic devices. They used a pseudo-two terminal device in which in the active channel was made of pentacene with Au nanoparticles embedded in the film. The gold nanoparticles where used as capacitors to store electrical charges. The holes and the electrons injected by the negative or positive voltage, respectively, applied to the gate before the measure, played the same role of neurotransmitters in biological synapses, therefore they modified the current on post-synaptic terminal, inducing potentiation or depression. The two behavior were induced by a protocol that alternated high and low frequencies, from 0.01 to 10 Hz. The higher were the frequencies the more evident was the depression curve; on the other hand, the facilitating behavior was better at lower frequencies, as seen in Figure 2.9. [34,48]

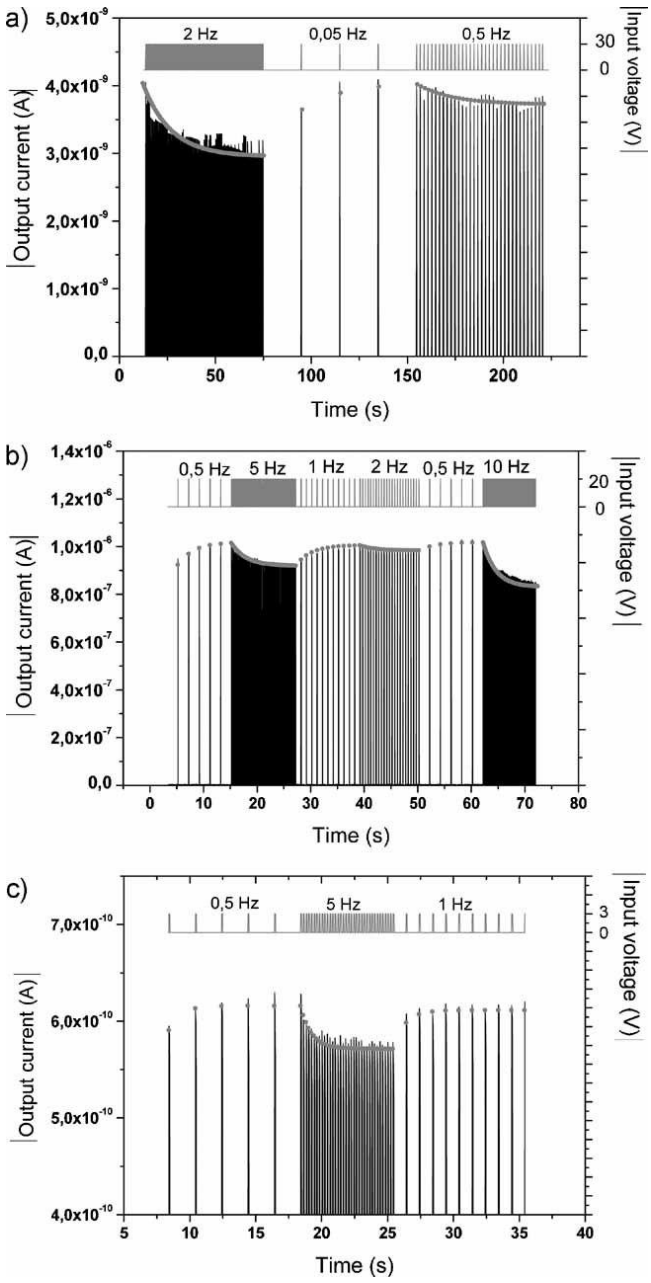

Figure 2.14 First protocol of STP proposed on a pentacene with Au nanoparticles embedded. The device show depressing behavior in the case of high frequency potential applied, on the contrary facilitating behavior. (From: Alibart et al., Adv. Mat., 2010 [34])

In 2016 Desbief *et al.* using electrolyte-gated organic synapstor (EGOS) exploited the same protocol to stimulate the devices interfaced with neurons grown and differentiated from neuroblastoma stem cells. The presence of cells did not affect the performances of neuromorphic device. The experiments with cell were made possible because of the low voltage of operation, as low as 50 mV.[49]

Other works were inspired by the work of Vuillaume: Di Lauro *et al.* in 2017 developed an EGOS based on C8-BTBT-C8 that mimicked the short-term potentiation and depression when the frequency of the gate

voltage was changed; similar results were achieved by Kim *et al.* with an OFET based on dinaphtho[2,3-b:2',3'-f]thieno[3,2-b]thiophene (DNTT).[50,51]

Giordani *et al.* used the STP protocol, in particular the depressing behavior, as a method of biosensing for dopamine by a two terminal device made of PEDOT:PSS electrodes. One of the electrodes were pulsed with negative square waves at a frequency of 500 Hz, while on the other were measured the displacement current. The characteristic relaxation time of the device τ varied with the concentration of dopamine in solution and, thanks to the properties of PEDOT:PSS of not binding the anions, the sensor discriminated dopamine from uric acid and ascorbic acid, the most important electrochemical interfering agents.[52–54]

The STM can be induced also in transistors, modulating the ionic concentrations into the channel between source and drain. In particular, Gerasimov *et al.* induced STP in OECT by accumulation of anions thanks the application of negative pulses to the gate, that induced a higher spike of current; on the other hand, STD was achieved applying positive potential and depleting the channel of negative charges.[45]

2.3.4 Spike-Timing Dependent Plasticity (STDP)

Spike-timing dependent plasticity (STDP) tunes the response of synapses as a function of pre- and post-synaptic activity and it is strongly implemented in bio-inspired devices.

In 2012 Alibart *et al.* using a nanoparticle organic memory field-effect transistor (NOMFET) checked the changes in the conductivity after applying stimuli at different Δt and they observed that: i) when the presynaptic neuron fired alone, the weight of the synapse did not change; ii)when the presynaptic spike was correlated with the post-synaptic spike, the conductivity increased, iii) when the post-synaptic spike occurred before the pre-synaptic spike, the conductivity decreased.[34]

Similar experiments were led by Fu *et al.* in 2018 with a OECT made of Poly(3-hexylthiopene-2,5-diyl) (P3HT) (Figure 2.10). They performed symmetric learning, in which the weight of the synapse is related to Δt between pre- and post-synaptic spikes.[55]

Jang and co-workers in 2019 coupled OFET architecture based on pentacene semiconductor and a poly(vinyldenedifluoride)-trifluoroethylene (PVDF-TrFE) ferroelectric layer as dielectric in the so-called Ferroelectric Organic Neuromorphic Transistor (FONT): the work shower how application of voltage stimuli to the gate electrode (pre-synpatic neuron) leads to a variation of the ferroelectrics degree of polarization, resulting in a modulation of the conductance of pentacene layer.[56]

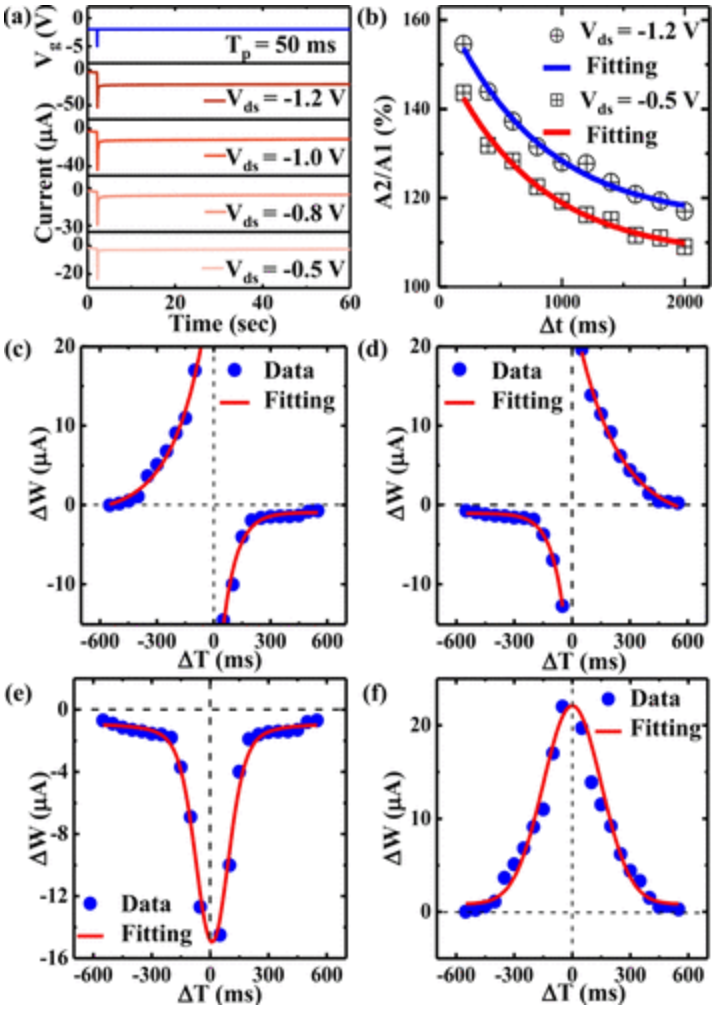

Figure 2.15 Typical example of the STDP behavior. (From: Fu et al., ACS Appl. Mater. Interfaces, 2018 [55])

2.3.5 Training and associative learning

Neuromorphic devices have been employed to mimic the associative learning process, described in 1927 by Ivan Pavlov using the classic conditioning and associative learning on his dog. In the classic conditioning, a neutral stimulus (NS) like the ring of a bell, is associated to the unconditioned stimulus (US) of food presence. The salivation of the dog (unconditioned response (UR) is a consequence of the US but the association of the bell ring to the food (training), makes the NS a conditioned stimulus.[57] Therefore, the conditioned stimulus can induce the salivation (conditioned response, CR) in absence of food. The process has not been completely explained by neuroscientists[58], but it's related to an interconnection between neurons involving polarizations and depolarizations, that induce long-form functional and structural modifications of the neural cells. Many studies have been performed to reproduce associative learning with inorganic and organic devices, with the aim to study the brain processes and to build artificial memories. As shown by the works presented in this section, the learning process is tightly bound to the

concept of spike-timing dependent plasticity (STDP), since the learning is usually achieved only after association of a pre-synaptic spike with a post-synaptic spike.

Erokhin *et al.* in 2011 reproduced the associative learning observed in pond snails, where amyl-acetate was the CS, by using two PANI based memristors in cascade. To obtain the synaptic behavior two input potentials where applied, a sinusoidal potential (representing the CS) on the first memristor and a transient DC potential (representing the US). The transient introduction of the DC potential induces the training by switching the second memristor and increasing five times the overall output current generated only by the CS.[59]

As shown in figure 2.11, the Pavlov's dog experiment was demonstrated by Bichler *et al.* by using two NOMFETs with pentacene semi-conductive channels. The salivation was defined as an output current higher than a threshold, reached only in presence of the US condition (input 1). When both inputs are active at the same time, the association is reached and the output of input 2 (the bell) increases above the threshold value, which was not possible for the input 2 alone. This process is possible only thanks to a feedback from the output that mimics the effect of the post-synaptic spike on the pre-synaptic one (STPD).[60]

Recently Minnekhanov *et al.* realized a Cu/Parylene/ITO memristor able to reproduce neuromorphic behaviors like STDP, thanks to resistive switches. The authors demonstrate the applications of the device by reproducing a classical Pavlovian conditioning experiment. The circuit is composed by two pre-synaptic neurons, N1 connected through a resistor (US) and N2 connected by the memristor (NS) are connected to a post synaptic neuron N3. Spiking only N2, the resistance of the memristor is too high to reach a threshold current that induces the spiking of the post-synaptic neuron N3. When both N1 and N3 potentials are spiked, the current that arrives at N3 induces the spiking of the post-synaptic neuron. This process reduces the resistance of the memristor, which becomes a conditioned stimulus and is able to generate the threshold current without N1 spiking.[61]

The flexibility of organic devices is one of their point of strength and it's a fundamental characteristic to realize wearable applications. The flexible electrochemical neuromorphic organic device (ENODe) with PEDOT:PSS active material developed by van de Burgt *et al.* in 2017 was tested by emulating the Pavlovian associative learning.[39] The device is characterized by a PEDOT:PSS presynaptic electrode, a PEDOT:PSS/PEI post-synaptic electrode, a Nafion electrolyte between the two and a pet substrate. The authors created a Pavlov model by using two firing "neurons" N1 and N2 with a pulsed potential, one connected to a synapse (N1) as the unconditioned stimulus, the other to the ENODe (N2) as neutral stimulus, and an output receiving "neuron" N3. The output post-synaptic current at N3 induced by the ENODe alone was possible

only after the transient association with the N1 firing, which increases the conductance of the ENODe channel, demonstrating the learning process.

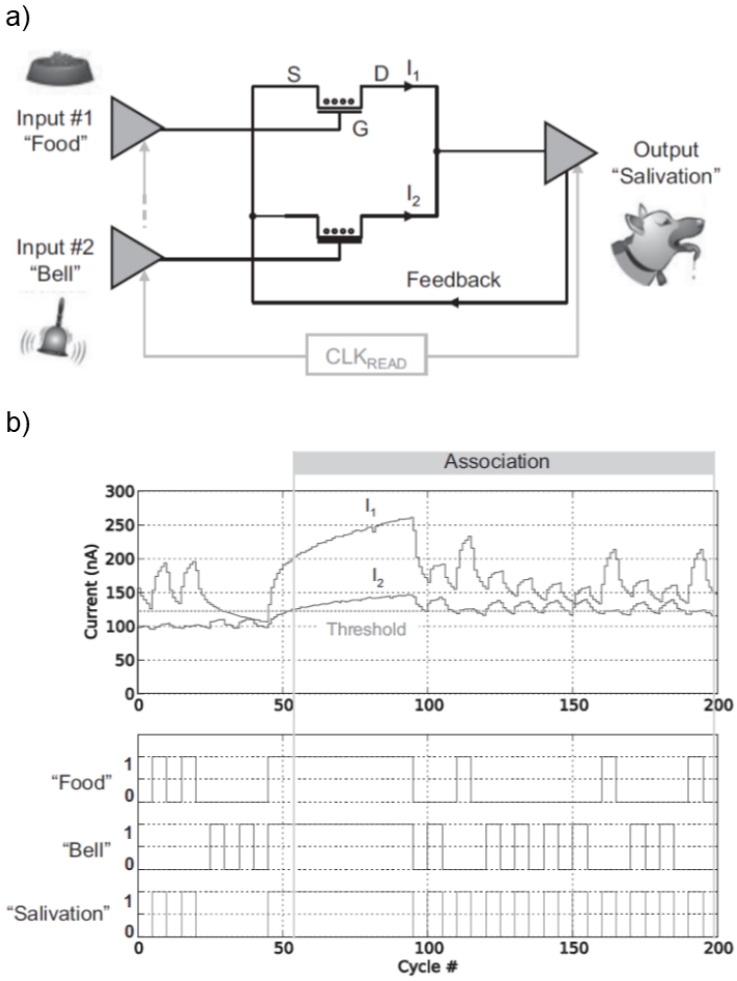

Figure 2.16: Pavlov's dog experiment reproduced with two NOMFETs. a) Circuit scheme. b)Drain-Source currents generated by the two NOMFETS, where I_1 is generated by the US and I_2 by the NS. Adapted from "Bichler et al 2013, Neural Computation" [60]

Jang *et al.* developed in 2019 a wearable artificial synapse, able to emulate the behavior of human synapses. The authors fabricated an ultrathin ferroelectric organic neuromorphic transistor (FONT) with Au bottom gate, a ferroelectric and biocompatible poly(vinylidenedifluoride)−trifluoroethylene (PVDF−TrFE) copolymer as dielectric and pentacene as the active material. FONTS are able to show modulable STDP behavior also in folded condition and can emulate a typical LTP and LDP response, where the strength of the potentiation or depression depends on both pre-post synaptic spike order and Δt between the spikes (smaller = stronger). These flexible artificial synapses are an example of components that will be applied in the realization of intelligent wearable devices.[56]

2.3.6 Application and perspectives

Since the first demonstrations just few years ago, organic neuromorphic devices have undergone great development, in terms of possible applications and performances, thanks to their features such as low energy consumption, low cost, high tunability and biocompatibility. Notwithstanding the initial proposed strategy were based on modified traditional electronics, recent studies have produced a miscellaneous set of new architectures and applications; in particular, one of the major aims of is to implement brain-like computing through neuromorphic circuitry in order to cross the limitations of silicon based circuits based on von Neumann architectures. The final goal is to obtain hybrid computing/memory devices capable to process information in more specialized ways and to store the results. [34,35,37–39,43–46,48,51]

Other possible applications are in the field of (neuro)prosthetics, robotics and bioinspired soft electronics, thanks to the wide selection of flexible, transparent and biocompatible materials that can be used. These devices can be implanted easily to mimic and restore lost physiological functionalities. [41,42,55,62]

Biosensing based on neuro-inspired mechanisms is still a novel approach that allows to sense in a label-free way chemical molecules without the use of electrochemical techniques.[52–54]

A great effort has been made to study and test new materials and new technological architectures, to mimic neurological functions with electronic devices. Important goals have been the use of biocompatible, environmental-friendly materials for dielectrics, such as chitosan[63] or gelatin,[64] and the demonstration of neuromorphic devices working with an extremely low energy consumption,[65] comparable to that of biological synapses.[46]

Lastly, some works exploited the development of novel architectures and measurement protocols[35,50] to interface organic electronic devices and biological environments, such as neuronal cell cultures.[49]

References

(1) Yamada, K. M.; Spooner, B. S.; Wessells, N. K. Ultrastructure and Function of Growth Cones and Axons of Cultured Nerve Cells. *J. Cell Biol.* **1971**, *49* (3), 614–635. https://doi.org/10.1083/jcb.49.3.614.

(2) Pereda, A. E. Electrical Synapses and Their Functional Interactions with Chemical Synapses. *Nat. Rev. Neurosci.* **2014**, *15* (4), 250–263. https://doi.org/10.1038/nrn3708.

(3) Cohen, L. B. Changes in Neuron Structure during Action Potential Propagation and Synaptic Transmission. *Physiol. Rev.* **1973**, *53* (2), 373–418. https://doi.org/10.1152/physrev.1973.53.2.373.

(4) Takagi, H. Roles of Ion Channels in EPSP Integration at Neuronal Dendrites. *Neurosci. Researcj* **2000**, *37*, 167–171. https://doi.org/10.1016/S0168-0102(00)00120-6.

(5) Zucker, R. S.; Regehr, W. G. Short-Term Synaptic Plasticity. *Annu. Rev. Physiol.* **2002**, *64* (1), 355–405. https://doi.org/10.1146/annurev.physiol.64.092501.114547.

(6) Cowan, N. Chapter 20 What Are the Differences between Long-Term, Short-Term, and Working Memory? In *Progress in Brain Research*; Elsevier, 2008; Vol. 169, pp 323–338. https://doi.org/10.1016/S0079-6123(07)00020-9.

(7) Goelet, P.; Castellucci, V. F.; Schacher, S.; Kandel, E. R. The Long and the Short of Long–Term Memory—a Molecular Framework. *Nature* **1986**, *322* (6078), 419–422. https://doi.org/10.1038/322419a0.

(8) MacLeod, K. M. Short-Term Synaptic Plasticity and Intensity Coding. *Hear. Res.* **2011**, *279* (1–2), 13–21. https://doi.org/10.1016/j.heares.2011.03.001.

(9) Cooper, L. N.; Bear, M. F. The BCM Theory of Synapse Modification at 30: Interaction of Theory with Experiment. *Nat. Rev. Neurosci.* **2012**, *13* (11), 798–810. https://doi.org/10.1038/nrn3353.

(10) Feldman, D. E. The Spike-Timing Dependence of Plasticity. *Neuron* **2012**, *75* (4), 556–571. https://doi.org/10.1016/j.neuron.2012.08.001.

(11) Lowel, S.; Singer, W. Selection of Intrinsic Horizontal Connections in the Visual Cortex by Correlated Neuronal Activity. *Science (80-.).* **1992**, *255* (5041), 209–212. https://doi.org/10.1126/science.1372754.

(12) Barbour, B.; Brunel, N.; Hakim, V.; Nadal, J. P. What Can We Learn from Synaptic Weight Distributions? *Trends Neurosci.* **2007**, *30* (12), 622–629.

https://doi.org/10.1016/j.tins.2007.09.005.

(13) Markram, H.; Gerstner, W.; Sjöström, P. J. Spike-Timing-Dependent Plasticity: A Comprehensive Overview. *Front. Synaptic Neurosci.* **2012**, *4* (July), 2010–2012. https://doi.org/10.3389/fnsyn.2012.00002.

(14) Cui, Y.; Prokin, I.; Mendes, A.; Berry, H.; Venance, L. Robustness of STDP to Spike Timing Jitter. *Sci. Rep.* **2018**, *8* (1), 1–15. https://doi.org/10.1038/s41598-018-26436-y.

(15) Shouval, H. Spike Timing Dependent Plasticity: A Consequence of More Fundamental Learning Rules. *Front. Comput. Neurosci.* **2010**, *4* (July), 1–13. https://doi.org/10.3389/fncom.2010.00019.

(16) C. Mead. Neuromorphic Electronic Systems. *Proc. IEEE* **1990**, *78* (10), 1629–1636.

(17) Chua, L. Memristor. The Missinf. *IEEE Trans. Circuit Theory* **1971**, *C* (5), 507–519.

(18) Potember, R. S.; Poehler, T. O.; Cowan, D. O. Electrical Switching and Memory Phenomena in Cu-TCNQ Thin Films. *Appl. Phys. Lett.* **1979**, *34* (6), 405–407. https://doi.org/10.1063/1.90814.

(19) Strukov, D. B.; Snider, G. S.; Stewart, D. R.; Williams, R. S. The Missing Memristor Found. *Nature* **2008**, *453* (7191), 80–83. https://doi.org/10.1038/nature06932.

(20) Di Ventra, M.; Pershin, Y. V.; Chua, L. O. Circuit Elements With Memory: Memristors, Memcapacitors, and Meminductors. *Proc. IEEE* **2009**, *97* (10), 1717–1724. https://doi.org/10.1109/JPROC.2009.2021077.

(21) Singh, T. B.; Marjanović, N.; Matt, G. J.; Sariciftci, N. S.; Schwödiauer, R.; Bauer, S. Nonvolatile Organic Field-Effect Transistor Memory Element with a Polymeric Gate Electret. *Appl. Phys. Lett.* **2004**, *85* (22), 5409–5411. https://doi.org/10.1063/1.1828236.

(22) Borghetti, J.; Derycke, V.; Lenfant, S.; Chenevier, P.; Filoramo, A.; Goffman, M.; Vuillaume, D.; Bourgoin, J.-P. Optoelectronic Switch and Memory Devices Based on Polymer-Functionalized Carbon Nanotube Transistors. *Adv. Mater.* **2006**, *18* (19), 2535–2540. https://doi.org/10.1002/adma.200601138.

(23) Bichoutskaia, E.; Popov, A. M.; Lozovik, Y. E. Nanotube-Based Data Storage Devices. *Mater. Today* **2008**, *11* (6), 38–43. https://doi.org/10.1016/S1369-7021(08)70120-2.

(24) Gacem, K.; Retrouvey, J.-M.; Chabi, D.; Filoramo, A.; Zhao, W.; Klein, J.-O.; Derycke, V. Neuromorphic Function Learning with Carbon Nanotube Based Synapses. *Nanotechnology* **2013**, *24* (38), 384013. https://doi.org/10.1088/0957-4484/24/38/384013.

(25) Star, A.; Lu, Y.; Bradley, K.; Grüner, G. Nanotube Optoelectronic Memory Devices. *Nano Lett.* **2004**, *4* (9), 1587–1591. https://doi.org/10.1021/nl049337f.

(26) Ma, L. P.; Liu, J.; Yang, Y. Organic Electrical Bistable Devices and Rewritable Memory Cells. *Appl.*

Phys. Lett. **2002**, *80* (16), 2997–2999. https://doi.org/10.1063/1.1473234.

(27) Tondelier, D.; Lmimouni, K.; Vuillaume, D.; Fery, C.; Haas, G. Metal⁄organic⁄metal Bistable Memory Devices. *Appl. Phys. Lett.* **2004**, *85* (23), 5763–5765. https://doi.org/10.1063/1.1829166.

(28) Kaneto, K.; Asano, T.; Takashima, W. Memory Device Using a Conducting Polymer and Solid Polymer Electrolyte. *Jpn. J. Appl. Phys.* **1991**, *30* (Part 2, No. 2A), L215–L217. https://doi.org/10.1143/JJAP.30.L215.

(29) Nilsson, D.; Chen, M.; Kugler, T.; Remonen, T.; Armgarth, M.; Berggren, M. Bi-Stable and Dynamic Current Modulation in Electrochemical Organic Transistors. *Adv. Mater.* **2002**, *14* (1), 51–54. https://doi.org/10.1002/1521-4095(20020104)14:1<51::AID-ADMA51>3.0.CO;2-#.

(30) Erokhin, V.; Berzina, T.; Fontana, M. P. Hybrid Electronic Device Based on Polyaniline-Polyethyleneoxide Junction. *J. Appl. Phys.* **2005**, *97* (6), 064501. https://doi.org/10.1063/1.1861508.

(31) Schroeder, R.; Majewski, L. A.; Grell, M. All-Organic Permanent Memory Transistor Using an Amorphous, Spin-Cast Ferroelectric-like Gate Insulator. *Adv. Mater.* **2004**, *16* (7), 633–636. https://doi.org/10.1002/adma.200306187.

(32) Novembre, C.; Guérin, D.; Lmimouni, K.; Gamrat, C.; Vuillaume, D. Gold Nanoparticle-Pentacene Memory Transistors. *Appl. Phys. Lett.* **2008**, *92* (10), 103314. https://doi.org/10.1063/1.2896602.

(33) Smerieri, A.; Berzina, T.; Erokhin, V.; Fontana, M. P. Polymeric Electrochemical Element for Adaptive Networks: Pulse Mode. *J. Appl. Phys.* **2008**, *104* (11), 114513. https://doi.org/10.1063/1.3033399.

(34) Alibart, F.; Pleutin, S.; Guérin, D.; Novembre, C.; Lenfant, S.; Lmimouni, K.; Gamrat, C.; Vuillaume, D. An Organic Nanoparticle Transistor Behaving as a Biological Spiking Synapse. *Adv. Funct. Mater.* **2010**, *20* (2), 330–337. https://doi.org/10.1002/adfm.200901335.

(35) Dai, S.; Wu, X.; Liu, D.; Chu, Y.; Wang, K.; Yang, B.; Huang, J. Light-Stimulated Synaptic Devices Utilizing Interfacial Effect of Organic Field-Effect Transistors. *ACS Appl. Mater. Interfaces* **2018**, *10* (25), 21472–21480. https://doi.org/10.1021/acsami.8b05036.

(36) Qian, C.; Kong, L.; Yang, J.; Gao, Y.; Sun, J. Multi-Gate Organic Neuron Transistors for Spatiotemporal Information Processing. *Appl. Phys. Lett.* **2017**, *110* (8), 083302. https://doi.org/10.1063/1.4977069.

(37) Wan, C. J.; Zhu, L. Q.; Liu, Y. H.; Feng, P.; Liu, Z. P.; Cao, H. L.; Xiao, P.; Shi, Y.; Wan, Q. Proton-Conducting Graphene Oxide-Coupled Neuron Transistors for Brain-Inspired Cognitive Systems. *Adv. Mater.* **2016**, *28* (18), 3557–3563. https://doi.org/10.1002/adma.201505898.

(38) Gkoupidenis, P.; Schaefer, N.; Strakosas, X.; Fairfield, J. A.; Malliaras, G. G. Synaptic Plasticity Functions in an Organic Electrochemical Transistor. *Appl. Phys. Lett.* **2015**, *107* (26), 263302. https://doi.org/10.1063/1.4938553.

(39) van de Burgt, Y.; Lubberman, E.; Fuller, E. J.; Keene, S. T.; Faria, G. C.; Agarwal, S.; Marinella, M. J.; Alec Talin, A.; Salleo, A. A Non-Volatile Organic Electrochemical Device as a Low-Voltage Artificial Synapse for Neuromorphic Computing. *Nat. Mater.* **2017**, *16* (4), 414–418. https://doi.org/10.1038/nmat4856.

(40) Alibart, F.; Pleutin, S.; Bichler, O.; Gamrat, C.; Serrano-Gotarredona, T.; Linares-Barranco, B.; Vuillaume, D. A Memristive Nanoparticle/Organic Hybrid Synapstor for Neuroinspired Computing. *Adv. Funct. Mater.* **2012**, *22* (3), 609–616. https://doi.org/10.1002/adfm.201101935.

(41) Lee, Y.; Oh, J. Y.; Xu, W.; Kim, O.; Kim, T. R.; Kang, J.; Kim, Y.; Son, D.; Tok, J. B.-H.; Park, M. J.; et al. Stretchable Organic Optoelectronic Sensorimotor Synapse. *Sci. Adv.* **2018**, *4* (11), eaat7387. https://doi.org/10.1126/sciadv.aat7387.

(42) Battistoni, S.; Erokhin, V.; Iannotta, S. Frequency Driven Organic Memristive Devices for Neuromorphic Short Term and Long Term Plasticity. *Org. Electron.* **2019**, *65* (November 2018), 434–438. https://doi.org/10.1016/j.orgel.2018.11.033.

(43) Kim, S.; Lim, M.; Kim, Y.; Kim, H.-D.; Choi, S.-J. Impact of Synaptic Device Variations on Pattern Recognition Accuracy in a Hardware Neural Network. *Sci. Rep.* **2018**, *8* (1), 2638. https://doi.org/10.1038/s41598-018-21057-x.

(44) Wang, T.-Y.; He, Z.-Y.; Chen, L.; Zhu, H.; Sun, Q.-Q.; Ding, S.-J.; Zhou, P.; Zhang, D. An Organic Flexible Artificial Bio-Synapses with Long-Term Plasticity for Neuromorphic Computing. *Micromachines* **2018**, *9* (5), 239. https://doi.org/10.3390/mi9050239.

(45) Gerasimov, J. Y.; Gabrielsson, R.; Forchheimer, R.; Stavrinidou, E.; Simon, D. T.; Berggren, M.; Fabiano, S. An Evolvable Organic Electrochemical Transistor for Neuromorphic Applications. *Adv. Sci.* **2019**, *6* (7), 1801339. https://doi.org/10.1002/advs.201801339.

(46) Xu, W.; Min, S.-Y.; Hwang, H.; Lee, T.-W. Organic Core-Sheath Nanowire Artificial Synapses with Femtojoule Energy Consumption. *Sci. Adv.* **2016**, *2* (6), e1501326. https://doi.org/10.1126/sciadv.1501326.

(47) Keene, S. T.; Melianas, A.; van de Burgt, Y.; Salleo, A. Mechanisms for Enhanced State Retention and Stability in Redox-Gated Organic Neuromorphic Devices. *Adv. Electron. Mater.* **2019**, *5* (2), 1–10. https://doi.org/10.1002/aelm.201800686.

(48) Bichler, O.; Zhao, W.; Alibart, F.; Pleutin, S.; Vuillaume, D.; Gamrat, C. Functional Model of a

Nanoparticle Organic Memory Transistor for Use as a Spiking Synapse. *IEEE Trans. Electron Devices* **2010**, *57* (11), 3115–3122. https://doi.org/10.1109/TED.2010.2065951.

(49) Desbief, S.; di Lauro, M.; Casalini, S.; Guerin, D.; Tortorella, S.; Barbalinardo, M.; Kyndiah, A.; Murgia, M.; Cramer, T.; Biscarini, F.; et al. Electrolyte-Gated Organic Synapse Transistor Interfaced with Neurons. *Org. Electron.* **2016**, *38*, 21–28. https://doi.org/10.1016/j.orgel.2016.07.028.

(50) Di Lauro, M.; Berto, M.; Giordani, M.; Benaglia, S.; Schweicher, G.; Vuillaume, D.; Bortolotti, C. A.; Geerts, Y. H.; Biscarini, F. Liquid-Gated Organic Electronic Devices Based on High-Performance Solution-Processed Molecular Semiconductor. *Adv. Electron. Mater.* **2017**, *3* (9), 1700159. https://doi.org/10.1002/aelm.201700159.

(51) Kim, C.-H.; Sung, S.; Yoon, M.-H. Synaptic Organic Transistors with a Vacuum-Deposited Charge-Trapping Nanosheet. *Sci. Rep.* **2016**, *6* (1), 33355. https://doi.org/10.1038/srep33355.

(52) Giordani, M.; Berto, M.; Di Lauro, M.; Bortolotti, C. A.; Zoli, M.; Biscarini, F. Specific Dopamine Sensing Based on Short-Term Plasticity Behavior of a Whole Organic Artificial Synapse. *ACS Sensors* **2017**, *2* (12), 1756–1760. https://doi.org/10.1021/acssensors.7b00542.

(53) Giordani, M.; Di Lauro, M.; Berto, M.; Bortolotti, C. A.; Vuillaume, D.; Gomes, H. L.; Zoli, M.; Biscarini, F. Whole Organic Electronic Synapses for Dopamine Detection; Kymissis, I., Shinar, R., Torsi, L., Eds.; 2016; Vol. 9944, p 99440P. https://doi.org/10.1117/12.2239532.

(54) Giordani, M.; Sensi, M.; Berto, M.; Di Lauro, M.; Bortolotti, C. A.; Gomes, H. L.; Zoli, M.; Zerbetto, F.; Fadiga, L.; Biscarini, F. Neuromorphic Organic Devices That Specifically Discriminate Dopamine from Its Metabolites by Nonspecific Interactions. *Adv. Funct. Mater.* **2020**, *2002141*, 2002141. https://doi.org/10.1002/adfm.202002141.

(55) Fu, Y.; Kong, L.; Chen, Y.; Wang, J.; Qian, C.; Yuan, Y.; Sun, J.; Gao, Y.; Wan, Q. Flexible Neuromorphic Architectures Based on Self-Supported Multiterminal Organic Transistors. *ACS Appl. Mater. Interfaces* **2018**, *10* (31), 26443–26450. https://doi.org/10.1021/acsami.8b07443.

(56) Jang, S.; Jang, S.; Lee, E. H.; Kang, M.; Wang, G.; Kim, T. W. Ultrathin Conformable Organic Artificial Synapse for Wearable Intelligent Device Applications. *ACS Appl. Mater. Interfaces* **2019**, *11* (1), 1071–1080. https://doi.org/10.1021/acsami.8b12092.

(57) Pavlov, I. P. Conditioned Reflexes: An Investigation of the Physiological Activity of the Cerebral Cortex. *Ann. Neurosci.* **2010**, *17* (3). https://doi.org/10.5214/ans.0972-7531.1017309.

(58) Grewe, B. F.; Gründemann, J.; Kitch, L. J.; Lecoq, J. A.; Parker, J. G.; Marshall, J. D.; Larkin, M. C.; Jercog, P. E.; Grenier, F.; Li, J. Z.; et al. Neural Ensemble Dynamics Underlying a Long-Term

Associative Memory. *Nature* **2017**, *543* (7647), 670–675. https://doi.org/10.1038/nature21682.

(59) Erokhin, V.; Berzina, T.; Camorani, P.; Smerieri, A.; Vavoulis, D.; Feng, J.; Fontana, M. P. Material Memristive Device Circuits with Synaptic Plasticity: Learning and Memory. *Bionanoscience* **2011**, *1* (1–2), 24–30. https://doi.org/10.1007/s12668-011-0004-7.

(60) Bichler, O.; Zhao, W.; Alibart, F.; Pleutin, S.; Lenfant, S.; Vuillaume, D.; Gamrat, C. Pavlov's Dog Associative Learning Demonstrated on Synaptic-like Organic Transistors. *Neural Comput.* **2013**, *25* (2), 549–566. https://doi.org/10.1162/NECO_a_00377.

(61) Minnekhanov, A. A.; Emelyanov, A. V.; Lapkin, D. A.; Nikiruy, K. E.; Shvetsov, B. S.; Nesmelov, A. A.; Rylkov, V. V.; Demin, V. A.; Erokhin, V. V. Parylene Based Memristive Devices with Multilevel Resistive Switching for Neuromorphic Applications. *Sci. Rep.* **2019**, *9* (1), 10800. https://doi.org/10.1038/s41598-019-47263-9.

(62) Kim, Y.; Chortos, A.; Xu, W.; Liu, Y.; Oh, J. Y.; Son, D.; Kang, J.; Foudeh, A. M.; Zhu, C.; Lee, Y.; et al. A Bioinspired Flexible Organic Artificial Afferent Nerve. *Science (80-.).* **2018**, *360* (6392), 998–1003. https://doi.org/10.1126/science.aao0098.

(63) Feng, P.; Xu, W.; Yang, Y.; Wan, X.; Shi, Y.; Wan, Q.; Zhao, J.; Cui, Z. Printed Neuromorphic Devices Based on Printed Carbon Nanotube Thin-Film Transistors. *Adv. Funct. Mater.* **2017**, *27* (5), 1604447. https://doi.org/10.1002/adfm.201604447.

(64) Lai, D.; Li, E.; Yan, Y.; Liu, Y.; Zhong, J.; Lv, D.; Ke, Y.; Chen, H.; Guo, T. Gelatin-Hydrogel Based Organic Synaptic Transistor. *Org. Electron.* **2019**, *75* (May), 105409. https://doi.org/10.1016/j.orgel.2019.105409.

(65) Ling, H.; Wang, N.; Yang, A.; Liu, Y.; Song, J.; Yan, F. Dynamically Reconfigurable Short-Term Synapse with Millivolt Stimulus Resolution Based on Organic Electrochemical Transistors. *Adv. Mater. Technol.* **2019**, *4* (9), 1900471. https://doi.org/10.1002/admt.201900471.

3 MATERIALS AND METHODS

The following chapter presents the organic materials that has been used in this work of thesis and the techniques of deposition, patterning and electrical characterization.

3.1 ORGANIC MATERIALS

3.1.1 PDMS

Polydimethylsiloxane (PDMS) is a silicon elastomer widely used in fabrication of devices and microfluidics, because it is thermally stable, simple to manipulate, chemical inert, stretchable, flexible and transparent; in addition, it is used for biomedical applications thanks to its biocompatibility. The surface properties can be tuned by the exposure to UV light, ozone or plasma discharge.

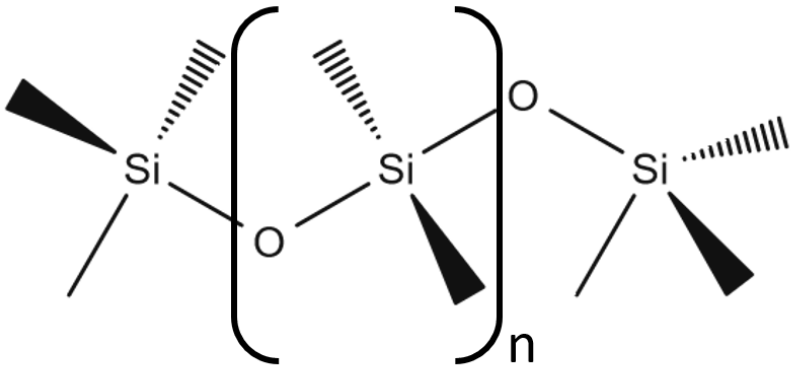

Figure 3.17 Chemical structure of PDMS.

As seen in Figure 3.1 PDMS is formed by an inorganic backbone of silicon and oxygen atoms, two methyl groups are attached to each silicon. Its structure implies a low surface energy (19.8 mN/m).

PDMS used in this thesis is Sylgard 184® Silicon Elastomer Kit (Dow Corning Corporation), purchased by Sigma-Aldrich, composed by two separated liquid components: the silicon and the reticulating agent. The preparation of the polymer is made by mixing the two components in a 9:1 ratio; after mixing, the product has to be degassed for 30 minutes, in order to eliminate the bubbles; finally it can be cast using different methods and then cured in thermostatic oven, adjusting time and temperature depending on the application.[1,2]

3.1.2 PEDOT:PSS

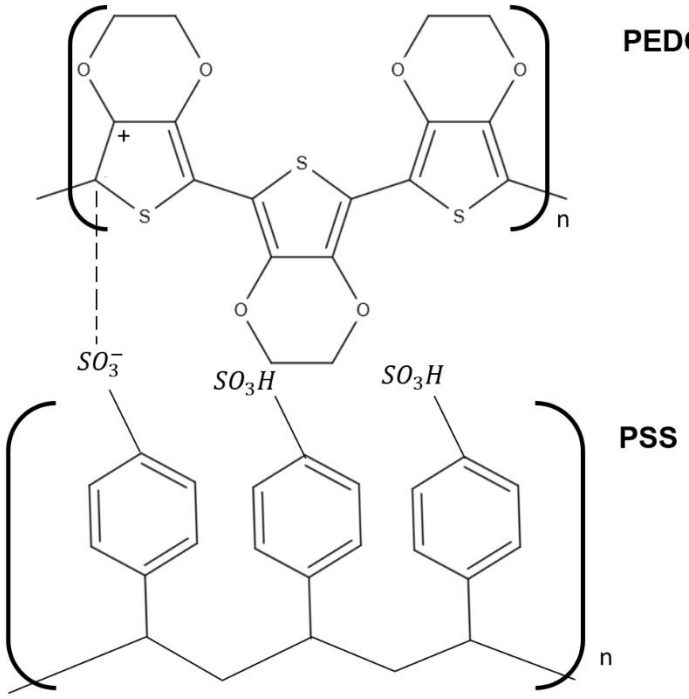

Figure 3.18 Chemical structure of PEDOT:PSS.

Poly(3,4-ethylenedioxythiophene):poly(styrenesulfonate) (PEDOT:PSS), shown in Figure 3.2, is a conductive polymer prepared using oxidative chemical or electrochemical polymerization. When PEDOT was discovered, it was found to be insoluble, but this inconvenient was circumvented doping it with PSS, which is a water soluble polyelectrolyte. In aqueous solution PEDOT forms a hydrophobic core, surrounded by PSS chains, forming a micelle structure.[3] This combination resulted in a water soluble conductive polymer with high conductivity and good stability. [4]

The conductivity of PEDOT:PSS is ensured by the thiophene rings of PEDOT that form a conjugated π system, heavily p-doped, while PSS does not participate to charge transport.

The conductivity of PEDOT:PSS is determined by the PEDOT:PSS ratio, that affects the density of sites of charge transport.

Nowadays, PEDOT:PSS is used in different industrial applications as conductive electrode in solid electrolyte capacitors, solar cells, antistatic coatings, bioelectronics devices or in OLEDs.[5]

In this thesis, we used two different formulations of PEDOT:PSS PH1000, one from Clevios (Heraeus, Deutschland, GmbH & co. KG) and one from Ossila Ltd. (Sheffield, UK). Both batches were added with 5%

w/w of dimethyl sulfoxide (DMSO) to increase the electrical conductivity and 0.2% w/w of (3-glycidyloxypropyl)trimethoxysilane to improve the mechanical stability and the adhesion to the substrate.[6] The aqueous solution is deposited by spin casting and the cured in thermostatic oven.

3.1.3 HMDS

Hexamethyldisalazane (HMDS), shown in Figure 3.3, has been used in order to modify the surface energy of glass, making the substrate more hydrophobic, and making the PDMS easier to peel off from the glass substrate.

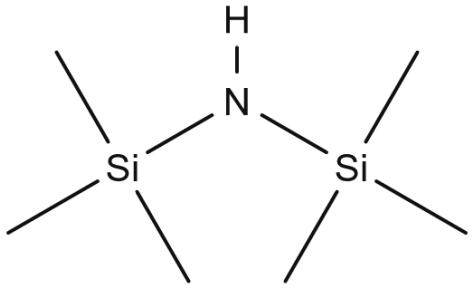

Figure 3.19 Chemical structure of HMDS.

3.2 FABRICATION TECHNIQUES

3.2.1 Spin coating

Spin coating is a technique to cast organic thin films from solutions. A drop of solution is put on a controlled rotating substrate and then spread by centrifugal force that permits to eject off the edges the excess and form the film on the substrate. [7] The technique is sketched in Figure 3.4.

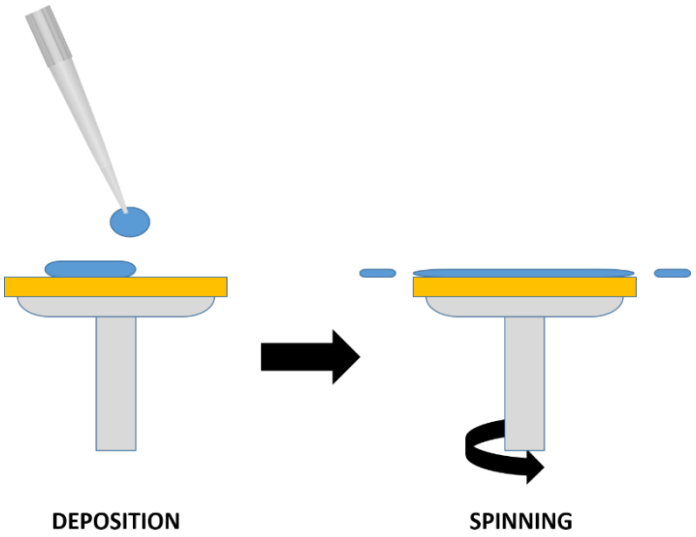

Figure 3.20 Sketch of spin coating process.

In general, the thickness of a spin coated film is described by Equation 3.1:

$$h = k_1 \omega^{\alpha} \qquad (3.1)$$

where h is the thickness of the film, ω is the angular velocity, k_1 and α are empirically determined constants.

However the exact thickness depends on the material solvent evaporation rate and viscosity and on the local temperature and humidity. [8]

We used a spin coater Model ws 400b-6npp/lite (Laurell, North Wales, USA), showed in Figure 3.5.

Figure 3.21 Spin coater Model ws-400b-6npp/lite by Laurell.

3.2.2 Laser ablation

The fabrication of the sensors was performed with ScribaR® (Scriba Nanotecnologie Srl, Bologna, Italy), showed in Figure 3.6, a laser scan marker that features a pulsed Nd:YAG class IV laser with a λ = 1064 nm, thus it is possible to pattern IR-absorbing materials. The machine has a sample holder controlled with three inertial micrometrical motors for x-, y- and z-displacements.

A Computer-Aided Design (CAD) drawing guides the movement of the sample holder, while, through a custom software it is possible to control laser power, marking speed, pulse width and pulse frequency.[9,10] The typical operation parameters are a marking speed of 2000 µm/s, a pulse width of 10 ns, a laser power of 8300 mV and a repetition frequency of 15500 Hz.

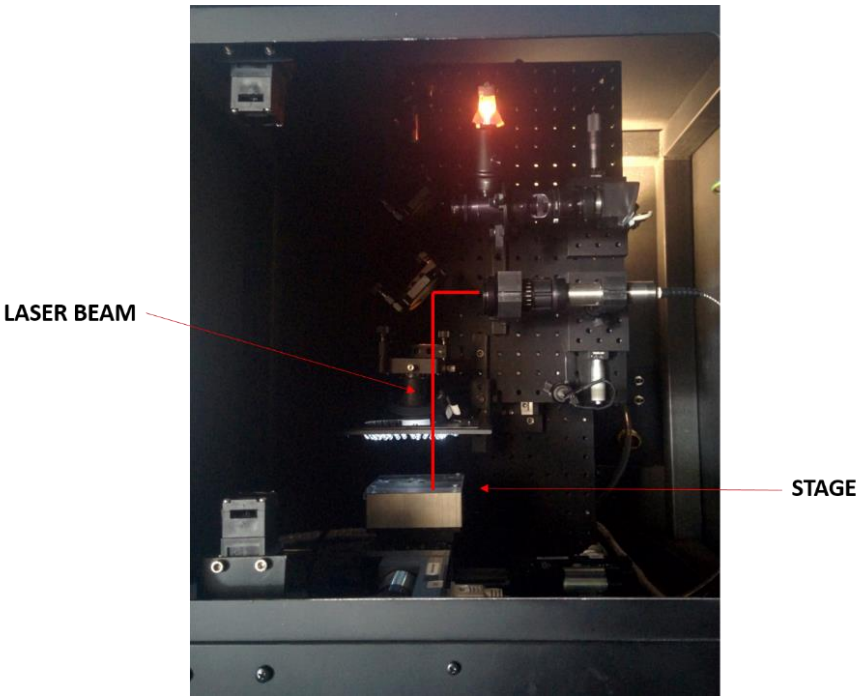

Figure 3.22 ScribaR® Laser Marker.

3.2.3 N_2 plasma

Plasma is defined as a ionized gas, thus the neutral atoms of the gas are split into anions and cations. The necessary energy to separate atoms is provided thermally, derived from electric current and from radiation. In the process of fabrication used during this thesis, we employed a N_2 plasma (Diener electronic GmbH and co. KG) and all the process was performed in vacuum.

N_2 plasma is used as a cleaning method (sketched in Figure 3.7) for removing contaminants and adsorbed molecules from the PDMS surface, moreover it makes the substrate more hydrophilic, making easier to spin coat PEDOT:PSS.

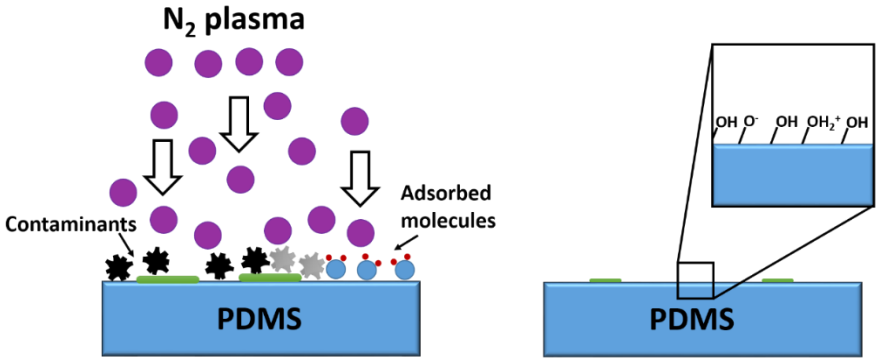

Figure 3.23 Schematic representation of N_2 plasma on PDMS.

3.3 FABRICATION OF THE DEVICES

3.3.1 DA sensor

The sensor fabrication starts with the use of a glass substrate that helps in the preparation of the substrate of PDMS and to maintain the films stretched.

First of all the glass is cleaned with the following procedure:

- Rub the glass with ethanol (EtOH), until it is perfectly transparent;
- Sonicate in EtOH for 15';
- Dry with N_2.

Then the glass is treated with HMDS for 4 hours in a chamber saturated of silane vapors, in order to obtain a hydrophobic surface.

Then PDMS substrate is prepared as follows:

- Spin-coating at 500 rpm for 3', acceleration 500 rpm/s;
- Curing for 1h at 120 °C in the thermostatic oven;
- Treat with N_2 plasma for 5'.

After the treatment PEDOT:PSS is spin coated for 3" at 500 rpm, acceleration 500 rpm/s and then 20" at 2200 rpm, acceleration 1000 rpm/s. The films are cured for 45' at 120 °C in the thermostatic oven.

We measured the thickness of the films with a profilometer P-6 Stylus Porfiler (KLA Technologies, California, USA) and PDMS resulted to be ca. 80 µm, while PEDOT:PSS ca. 400 nm.

The devices are then laser ablated with ScribaR® following the CAD drawing showed in Figure 3.7 in order to create the PEDOT:PSS electrodes.

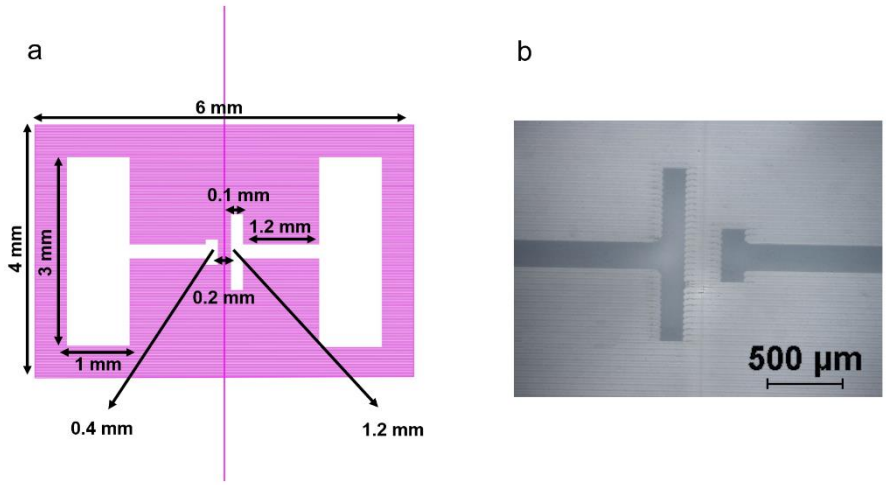

Figure 3.24 a) CAD drawing of the sensors. Fuchsia lines represent the material removed by the laser. b) Optical micrography of the sensor electrodes.

Figure 3.8 shows a) the overall fabrication process, b) the sketch of the complete sensor and c) the final flexible sensor.

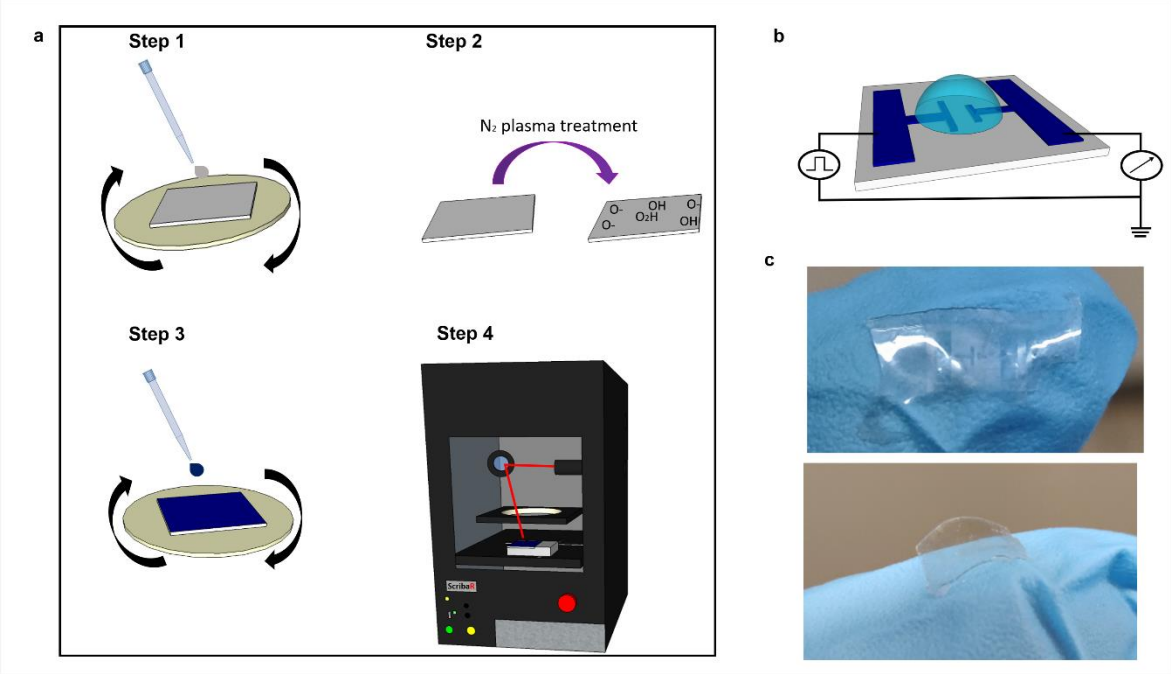

Figure 3.25 a) steps of fabrication of the sensor; b) sketch of the sensor and scheme of the measurement protocol; c) final flexible sensor.

3.4 ELECTRICAL CHARACTERIZATION

In this work, the electrical characterization of the sensors was performed with an Agilent (California, USA) model B2912A Source-Measure Unit (SMU), shown in Figure 3.11 b, which permits to apply potentials

and recording current with a high resolution (up to 10 fA/100nV) and low noise. The parameters of the measurements are set through a custom-designed software (Figure 3.11 a).

The SMU is connected through triaxial cables to a Faraday cage (Figure 3.11 b) yielding a pA base noise level. To characterize the device, it is placed inside the Faraday cage and then connected through high-precision spring-probe contacts.

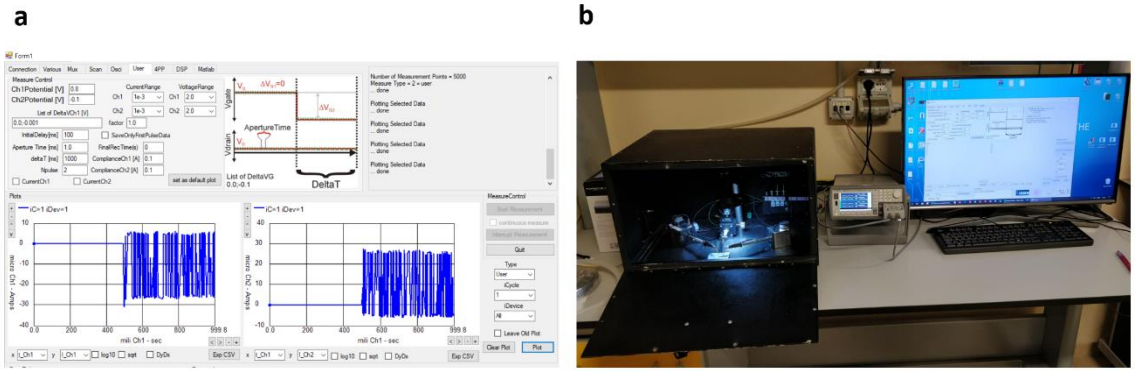

Figure 3.26 a) screen of the custom-designed software; b) stage for electrical characterization composed by a Faraday cage, a SMU and a computer.

3.4.1 Short-Term Plasticity (STP)

The DA sensor electrical measurements mimic the Short-Term Plasticity (STP) behavior, typical of synapses. Unipolar rectangular voltage pulses (-200 mV) are generated at the pre-synaptic electrode at a frequency of 500 Hz for 1 s, while at the post-synaptic electrode is measured the displacement current, that shows an exponential decay: the peak current intensity decreases from one pulse to the next, until it reaches a plateau (Figure 3.12).

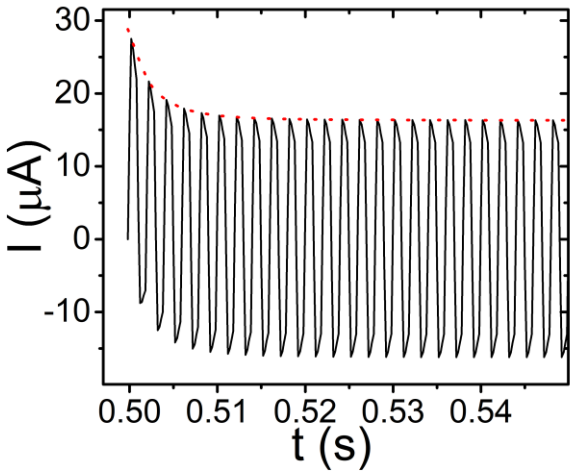

Figure 3.27 Typical current response of the device. The red dots represent the maxima.

The current response is analyzed by RStudio (RStudio, Inc.), that through a self-made script extract the maxima of the current that are then fitted with the equation 3.2, in order to extract the characteristic relaxation time of the system, τ.

$$I(t) = I_{\infty} + I_0 \cdot e^{-t/\tau} \tag{3.2}$$

In this work of thesis we tested the sensor for dopamine, ascorbic acid, uric acid, epinephrine, norepinephrine, homovanillic acid, 3-methoxytyramine and 3,4-dihydroxyphenilacetic acid, individually to build a dose curve and in mixed solution with increasing concentrations of DA and the physiological concentration of one of the listed molecules. For each analyte, the dose curves are tested at least 5 times and then the standard deviation or the standard error of the mean are calculated. The solutions were all prepared in Phosphate-buffered Saline (PBS) 50 mM at a pH 7.4. All the reagents were purchased by Sigma-Aldrich.

References

(1) Mata, A.; Fleischman, A. J.; Roy, S. Characterization of Polydimethylsiloxane (PDMS) Properties for Biomedical Micro/Nanosystems. *Biomed. Microdevices* **2005**, *7* (4), 281–293. https://doi.org/10.1007/s10544-005-6070-2.

(2) Lacour, S. P. Stretchable Thin-Film Electronics. In *Stretchable Electronics*; Wiley-VCH Verlag GmbH & Co. KGaA: Weinheim, Germany, 2012; pp 81–109. https://doi.org/10.1002/9783527646982.ch4.

(3) Zabihi, F.; Xie, Y.; Gao, S.; Eslamian, M. Morphology, Conductivity, and Wetting Characteristics of PEDOT:PSS Thin Films Deposited by Spin and Spray Coating. *Appl. Surf. Sci.* **2015**, *338*, 163–177. https://doi.org/10.1016/j.apsusc.2015.02.128.

(4) Groenendaal, L.; Jonas, F.; Freitag, D.; Pielartzik, H.; Reynolds, J. R. Poly(3,4-Ethylenedioxythiophene) and Its Derivatives: Past, Present, and Future. *Adv. Mater.* **2000**, *12* (7), 481–494. https://doi.org/10.1002/(SICI)1521-4095(200004)12:7<481::AID-ADMA481>3.0.CO;2-C.

(5) Elshner, Andreas; Kirchmeyer, Stephan; Lovenich, Wilfried; Merker, Udo; Reuter, K. *PEDOT. Principles and Applications of an Intrinsically Conductive Polymer*; CRC Press, 2010.

(6) Zhang, S.; Kumar, P.; Nouas, A. S.; Fontaine, L.; Tang, H.; Cicoira, F. Solvent-Induced Changes in PEDOT:PSS Films for Organic Electrochemical Transistors. *APL Mater.* **2015**, *3* (1), 014911. https://doi.org/10.1063/1.4905154.

(7) Kotsuki, K.; Tanaka, H.; Obata, S.; Stauss, S.; Terashima, K.; Saiki, K. The Importance of Spinning Speed in Fabrication of Spin-Coated Organic Thin Film Transistors: Film Morphology and Field Effect Mobility. *Appl. Phys. Lett.* **2014**, *104* (23). https://doi.org/10.1063/1.4883216.

(8) Hall, D. B.; Underhill, P.; Torkelson, J. M. Spin Coating. **1998**, *38* (12), 2039–2045. https://doi.org/10.1002/pen.10373.

(9) Campana, A.; Cramer, T.; Greco, P.; Foschi, G.; Murgia, M.; Biscarini, F. Facile Maskless Fabrication of Organic Field Effect Transistors on Biodegradable Substrates. *Appl. Phys. Lett.* **2013**, *103* (7), 073302. https://doi.org/10.1063/1.4818549.

(10) Giordani, M.; Di Lauro, M.; Berto, M.; Bortolotti, C. A.; Vuillaume, D.; Gomes, H. L.; Zoli, M.; Biscarini, F. Whole Organic Electronic Synapses for Dopamine Detection; Kymissis, I., Shinar, R., Torsi, L., Eds.; 2016; Vol. 9944, p 99440P. https://doi.org/10.1117/12.2239532.

4 RESULTS

In the following chapter are reported the papers and the results produced during the period of PhD.

In particular:

- *Section 4.1 is from ''Giordani et al., Proceeding of SPIE, 9944, (2016)''*
- *Section 4.2 is from ''Giordani et al., ACS Sensor, 2(12), 1756-1760, (2017)''*
- *Section 4.3 is from ''Giordani et al., Advanced Functional Materials, 2002141, (2020)''*

4.1 WHOLE ORGANIC ELECTRONIC SYNAPSES FOR DOPAMINE DETECTION

In this first work, we tested the artificial synapse with a wide STP protocol, in order to understand the behavior and to set the best frequency to work with. The frequency was chosen as the less noisy and the one with the most significant variations through the different concentrations of analytes. Then, the sensor was operated to discriminate DA from AA, that is one of the most important electrochemical interfering agents. The dose curve was limited to 50 nM to 500 µM.

The whole organic artificial synapses showed a robust and reproducible STP response throughout a wide range of pulse amplitude and frequency as shown in Figure **4.1**.

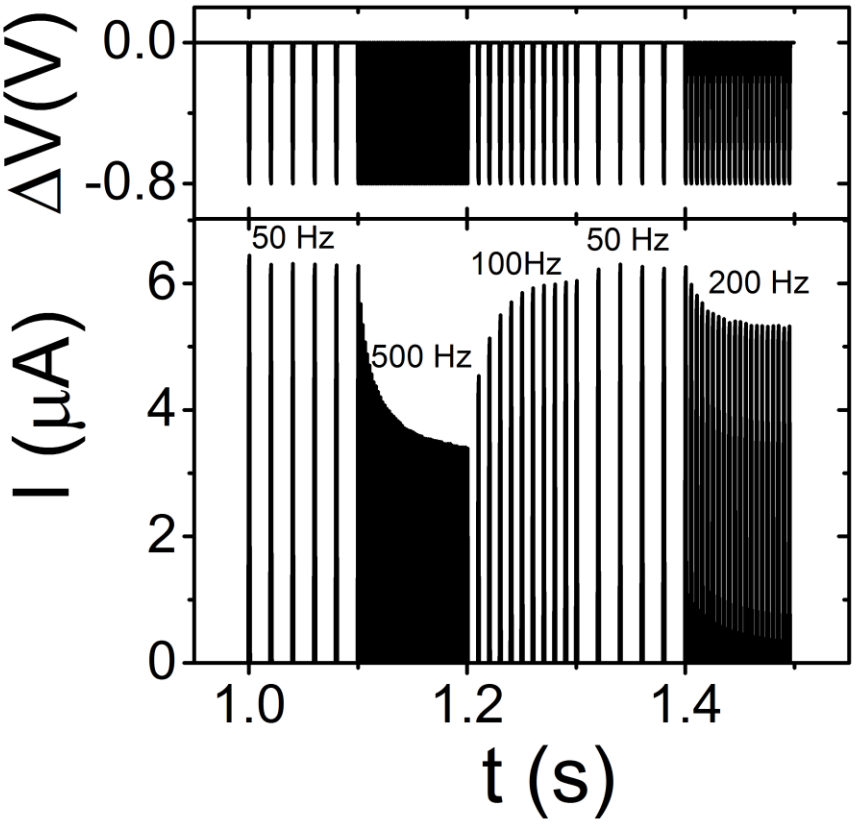

Figure 4.28 Typical STP response of the device to impulses at different frequencies (see top) and the corresponding current responses (bottom). Depressing behavior is observed at the highest frequencies (i.e. 500 Hz and 200 Hz).

Different pulse trains were tested, changing frequency and pulse amplitude, in order to maximize the dynamic response of the depressing region of the STP. This optimization led to the development of a fast and effective protocol for operating the synapse as a sensor exclusively under suppressing behavior.[1,2] The protocol contemplates one second of buffer time followed by one second of square wave stimulation

at 500Hz, with pulse amplitude as low as 200mV. This protocol was applied to devices in electrolytic solutions containing increasing concentration of DA and AA, starting from 50nM up to 500µM.

Evolution of the suppressing behavior in response to different analyte concentrations is shown in Figure **4.2**.

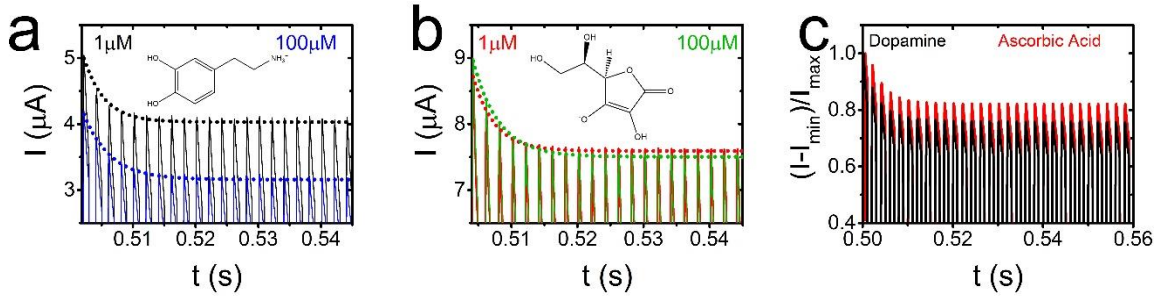

Figure 4.29 : (a) STP current responses to a 500 Hz stimulation (depressing behavior) for 1 µM and 100 µM solutions of DA and (b) AA and fit curves (dotted lines) from eq. 4.1. The current response changes at different DA concentrations (a), while it does not undergo a variation vs AA concentration (b). (c) Normalized current response for equal concentrations of DA and AA (viz. 250 µM).

Figure 4.2 a and 4.2 b show the response of the device by varying by two orders of magnitude the concentration of DA and AA, respectively; as regards DA a significant change of the response was observed, while the tracks recorded for AA are superimposable. These results hint that the decay timescale depends on the concentration of DA, and that there is no, or marginal, dependence on the concentration of AA. Furthermore, in Figure 4.2 c the plot of the normalized current responses of devices exposed to DA and AA is shown. It appears that the decay of AA maxima is slower than the decay of DA. This means that the chemical nature of the analyte affects the decay rate of the synapse depressing behavior.

In order to express quantitatively the evolution of the current vs characteristic time in response to the variation of analyte concentration, we extract the characteristic time of the suppressing behavior, τ as detailed in the following. First of all, the maximum current value In for each (n-th) spike was extracted from the STP characteristic and all the maxima were plotted vs time t. The observed trend of the maxima was then fitted according to:

$$I_n(t_n) = (I_0 - I_{DC}) \cdot exp\left(-\frac{t_n}{\tau}\right) + I_{DC} \qquad (4.1)$$

where I_0 is the magnitude of the current in response to the first voltage spike, and I_{DC} is the long-time (direct current DC) plateau that is asymptotically reached upon the exponential decay. Example of best fit curves are shown in Figure 4.2 as dotted lines.

In Figure 4.3 the dose-response curves are shown.

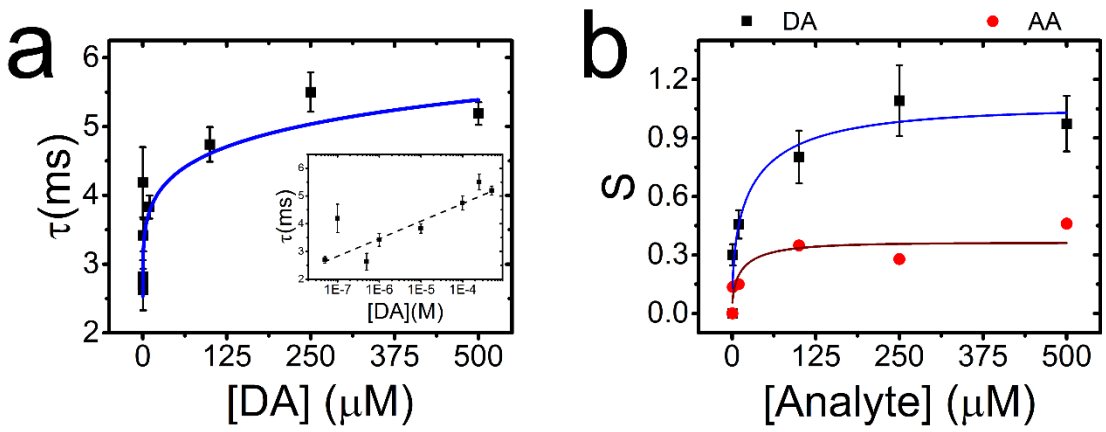

Figure 4.30 (a) τ values extracted at different DA concentrations (i.e. from 0 to 500 μM). The blue curve is the best fit obtained with function eq. 2; the inset shows the lin-log dependence of τ on [DA]. (b) S variation for same concentrations of DA (black squares) and AA (red circles, error bars are comparable to the marker size); continuous lines are the best fits obtained with function eq.3.

Figure 4.3 a shows the correlation between τ and DA concentration. The observed strong dependence indicates how the characteristic time τ of the PEDOT:PSS/DA system substantially changes upon increasing DA concentration. Changes of τ can be ascribed to the increased impedance of the system, due to the cation-π interaction that immobilizes positive charges in the polymeric PEDOT:PSS network thus lowering its conductivity and leading to the progressive neutralization of the sulfonate anions. The dose-response curve was fitted according to equation 4.2, and the result of the fit is shown as solid blue line in Figure 4.3 a.

$$\tau = \tau_0 + \tau_\infty \left(1 - e^{-\left(\frac{[DA]}{\xi}\right)^\beta}\right) \qquad (4.2)$$

Here the exponent β indicates the steepness of the rise in the lower concentration range, τ_∞ is the asymptotic plateau corresponding to the upper detection limit of the sensor, τ_0 is the intrinsic τ value when no DA is present in solution, ξ is the concentration of DA corresponding to the crossover from rising branch to the plateau. The inset of Fig. 4.3 a highlights the "power-law" trend implicit in equation 4.2, since the first non-zero expansion term of the factor in parenthesis of equation 4.2 is proportional to [DA] β.

In order to suppress device-to-device variation, a normalization of τ has been operated adapting a method originally developed by Ishikawa et al.[3], to yield a signal variation $S = \frac{\tau - \tau_0}{\tau_0}$ which results to be robust from device to device. Its dependence on [DA] can be fitted as follows:

$$S = \frac{\tau_\infty}{\tau_0}\left(1 - e^{-\left(\frac{[DA]}{\xi}\right)^\beta}\right) \tag{4.3}$$

Comparison of S vs [Analyte] plots for DA and AA and their respective fits are shown in Figure 4.3 b. It evidences the sensitivity of the artificial synapse and the specificity towards DA vs AA. In Table 4.1 the comparison of the best-fit parameters ξ, β, and τ_∞/τ_0 is reported.

Table 4.1. Best fit parameters for S vs [Analyte].

Analyte	β	ξ (μM)	τ_∞/τ_0
Dopamine	0.49±0.18	32±12	1.05±0.18
Ascorbic Acid	0.52±0.23	22±17	0.38±0.04

It is important to notice how ξ and β values are not statistically different, while τ_∞/τ_0 more than doubles from AA to DA. We may argue that both ξ and β are characteristic of the device, while τ_∞/τ_0 is strongly related to the PEDOT:PSS/Analyte interaction.

It is possible to infer that the two possible pathways of interaction between PEDOT:PSS and DA (i.e. cation-π and π-π) influence constructively the resistance of PEDOT:PSS electrodes and, subsequently, the τ of the device. This does not seem to occur in the case of AA, which may interact only by π-π interaction. The negative charge of AA is repelled by PSS- which, according to studies of the micromorphology of PEDOT:PSS, is exposed to the electrolyte, whereas PEDOT forms the core of the domains. This may cause the PEDOT:PSS to be also ion-charge selective, which enhances the discrimination of the two species.

The sensitivity, being the derivative of the function S Eq. 4.3 with respect to the analyte concentration, in the case of DA will read:

$$\frac{dS}{d[DA]} = \frac{\beta}{[DA]}\frac{\tau_\infty}{\tau_0}\left(\frac{[DA]}{\xi}\right)^\beta e^{-\left(\frac{[DA]}{\xi}\right)^\beta} \tag{4.4}$$

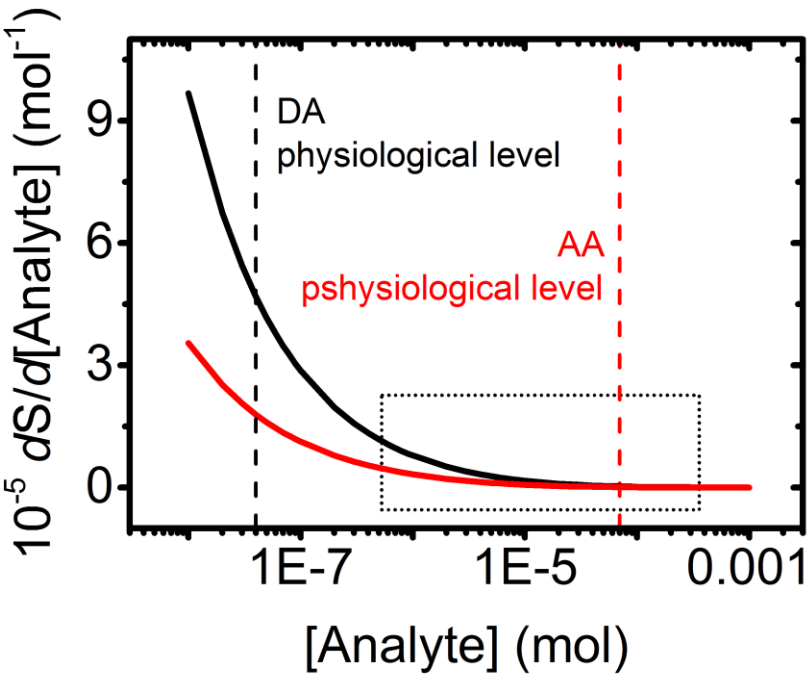

Figure 4.31 plots of the theoretical sensitivity from eq. 4.4 calculated with best-fit parameters of the curve in 4.3b (corresponding to the equation 4.3) for DA (black) and AA (red). In the graph the average physiological levels of the two analytes are highlighted with dashed lines (black and red respectively), the dotted rectangle highlights the concentration range for which comparison has been experimentally evaluated (see fig. 4.3 b).

The curves in Figure 4.4, obtained from equation 4.4, show that the sensitivity is much higher at lower concentrations, and that it scales as τ_∞/τ_0 at each concentration. At the physiological/pathological levels of DA (hundreds of nM to few nM), the latter have not been explored in this work, the sensitivity is estimated to be on the order of 5 x 10^5 mol^{-1}. Because the physiological concentration of AA in the body is on the order of µM vs nM concentration of DA, we expect that our device will be sensitive and selective to DA in physiological conditions, being the sensitivity for DA more than 200 times larger than the one for AA at their respective physiological levels. The sensitivity should be even higher at pathological levels of DA (low nM). This sensitivity towards DA greatly in excess of the sensitivity of AA is indeed responsible for the selectivity of our device, and supports the preferential interaction of DA vs AA towards PEDOT:PSS. and τ_∞/τ_0 is reported.

The possibility to discriminate DA from AA by exploiting different interactions of the analyte with the active material is extremely attractive. The standard fast-scan cyclic voltammetry characterization does not allow one to resolve the two species, being the redox potentials of the two species close to each other. There, the sensitivity is ≈ 10^8 mol^{-1}.[4] Their discrimination requires a separation that may be implemented with an ion-selective Nafion coating of the electrode. Our organic synapse has the advantage that it

integrates both the electrical transduction and the ion selectivity through the multifunctionality of PEDOT:PSS. These results herald PEDOT:PSS as a promising material for dopamine, and possibly other catecholamines, ultra-high sensitive detection.

4.2 SPECIFIC DOPAMINE SENSING BASED ON SHORT-TERM PLASTICITY BEHAVIOR OF A WHOLE ORGANIC ARTIFICIAL SYNAPSE

In this work we increased the concentration of the dose curve (form 1 pM to 1 mM) in order to include the physio-pathological concentrations of DA, moreover, within this wide range are comprised also the physiological concentration of AA and uric acid (UA). With these two moieties we tested the standard electrochemical interfering agents present in extracellular and cerebrospinal fluids.

In order to construct the dose curve, the STP curve was recorded for solutions containing increasing concentrations of DA, AA and UA. AA and UA are considered standard interfering agents in DA detection with electrochemical approaches, because their redox potentials are close to the DA one.[5,6] The concentration of DA, AA and UA was systematically varied across nine orders of magnitude from 1pM to 1mM (see Figure 4.5a).

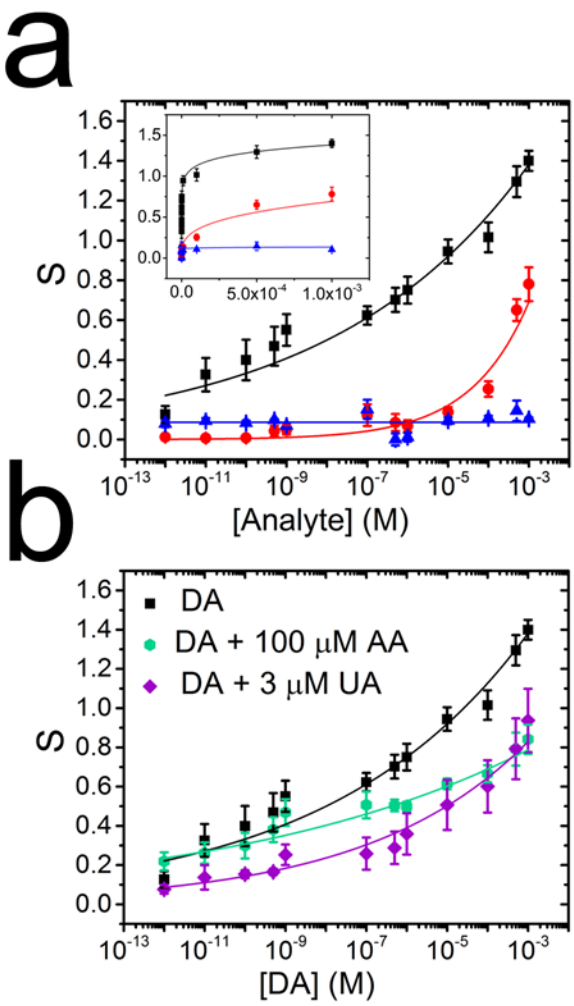

Figure 4.32 Dose responses: a) plot of S vs [DA] (black squares) and the same concentrations of two interfering agents [AA] (red circles) and [UA] (blue triangles); in the inset the lin-lin plot of S vs [DA], [AA] and [UA]. b) Overlay of the dose curves in response to DA (black squares) and DA in mixed solutions: DA+100 µM AA (green hexagons) and DA+3 µM UA (purple lozenges). Solid lines are phenomenological exponential trends, obtained by fitting data with the functional $S = K_{res} \cdot [Analyte]^n$ *(*R^2 *value for DA is 0.9756, for DA+100 µM AA is 0.9517 and for DA + 3 µM UA is 0.9483), where* K_{res} *is an apparent constant related to the interactions between analyte and PEDOT:PSS and n is a growth exponent related to the number of interaction sites.*[7]

The reference characteristic relaxation time, $\tau_{STP,0}$, is extracted with the electrolyte in the absence of the analyte; S is averaged over five distinct devices and error bars are reported as SEM.

The dose curve of DA (Figure 4.5a, black squares) shows an increasing trend of S vs [DA] in a range from 0.1 to 1.5. The dose curve of AA (Figure 4.5a, red circles) is almost constant for [AA]<100 µM, and rises up to 0.8 for larger concentrations, the signal being about 50% of that of DA alone. The dose curve of UA (Figure 4.5a, blue triangles) exhibits an almost constant signal whose value is much smaller than DA signal recorded with [DA]>1 pM.

These data show that our sensor is selectively responding to DA with respect to both AA and UA across the whole range of concentrations.

The rise of S vs [DA] is very steep at the lowest concentrations up to 10 µM, then S keeps on increasing at a lower rate (see inset of Figure 4.5a). Conversely, S changes slowly by 0.1 across 6 decades of [AA] up to 10 µM (red dots) then it rises by 0.6 in two decades. The slopes of the dose curves are $4 \cdot 10^{8}$ M^{-1} at [DA]=0.1 nM, $8 \cdot 10^{7}$ M^{-1} at [DA]=1 nM, $4 \cdot 10^{5}$ M^{-1} at [DA]=100 nM and $1 \cdot 10^{3}$ M^{-1} at [AA]= 100 µM, respectively. The limits of detection (LOD) are 1 pM for DA 100 µM for AA, while we cannot extract it for UA. These numbers confirm that our device should discriminate DA from AA and UA because the sensitivity is much larger in the case of DA at the pathological and physiological (both tonic and phasic) DA concentrations.[8,9]

Since DA, AA and UA are co-present in the brain and their relative levels change over time and within specific brain regions, we assessed the sensor response to [DA] in the presence of [AA] = 100 µM as in the CSF, at [UA] =3 µM, as in the striatum, and [UA] = 30 µM as in the CSF.[10] The results are shown in Figure 4.5b (green hexagons for AA, purple lozenges for [UA]= 3 µM, and pink triangles for [UA]= 30 µM in Figure 4.6).

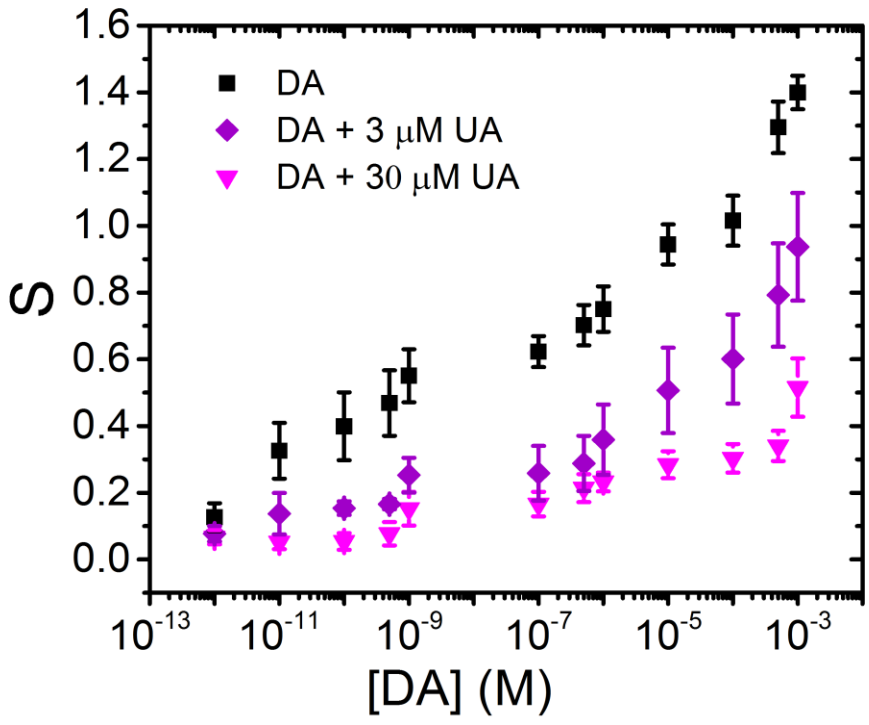

Figure 4.33 Overlay of the dose curves in response to DA (black squares) and DA in mixed solutions: DA + 3 µM UA (purple lozenges) and DA + 30 µM UA (pink triangles).

The dose curve of the mixture with AA lies in between the DA and AA curves, closer to the one vs [DA] and much above the one vs [AA]. At the lowest [DA], dose curve of the mixed solutions overlaps the curve of “sole” DA, while at the highest [DA] it tends to the curve of AA. In Figure 4.7 we evidence the correlations by plotting the signal recorded at each DA concentration in the mixtures vs the signal of the “sole” DA solutions. It is apparent from the adherence of the data points to the straight line at 45° in Figure 4.7a that there is a strong correlation between the signal recorded in the presence of AA with the one of “sole” DA in the range of [DA]<100 µM, at which the signal deviates by about 30% with respect to the one of the “sole” DA. The dopamine LOD in [AA] 100 µM is estimated as low as 1 pM. Sensitivity towards [DA] variations in AA mixed solution is retained at [DA] values above 1 nM, which is the concentration range reached after physiological phasic activation of dopaminergic neurons. At the concentrations below 1 nM, the response of the mixture appears dominated by DA-induced response only, irrespectively of the presence of a much larger concentration of AA.

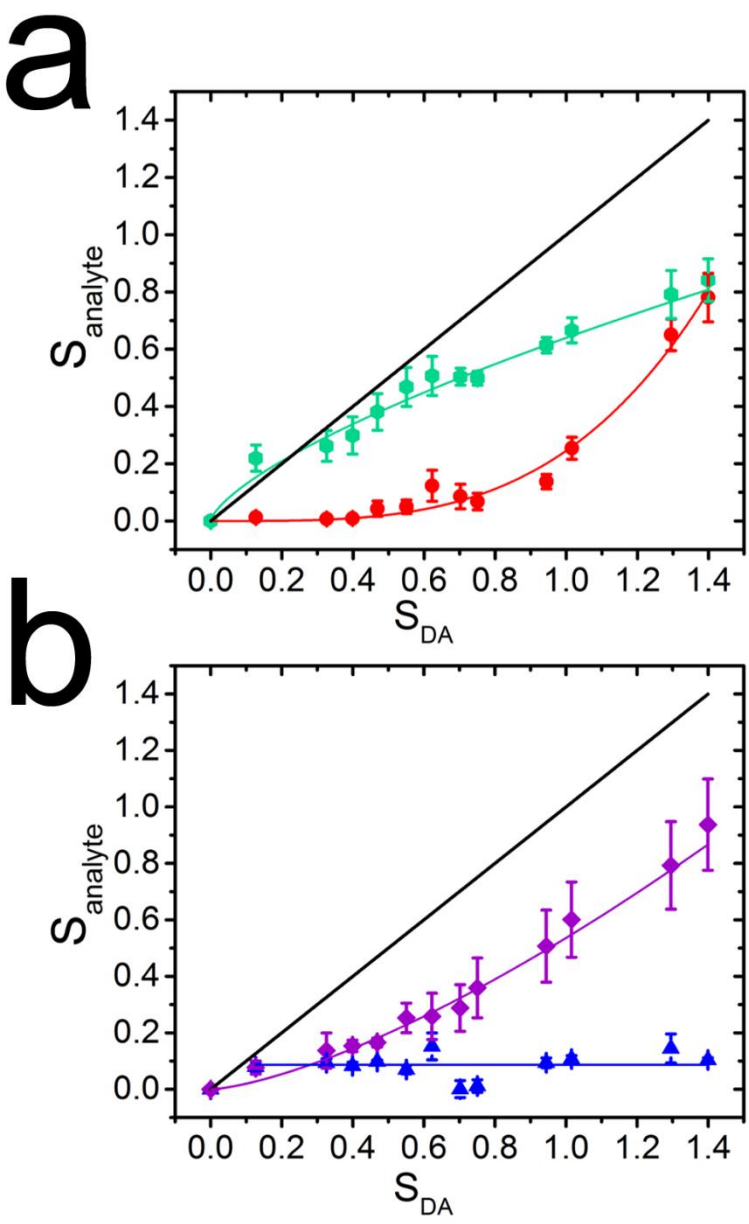

Figure 4.34 Correlation plots: a) signal response S recorded for [DA] (black line), [AA] (red circles) and [DA] + AA 100 µM (green hexagons) vs S for [DA]. b) signal response S recorded for [DA] (black line), [UA] (blue triangles) and [DA] + UA 3 µM (purple lozenges) vs S for [DA].

The dose curve of the mixture with [UA] = 3 µM has the same trend as the "sole" DA solution dose curve, albeit the signal is lower at any [DA]. A greater lowering is observed at [UA] = 30 µM (Figures 4.6 and 4.8).

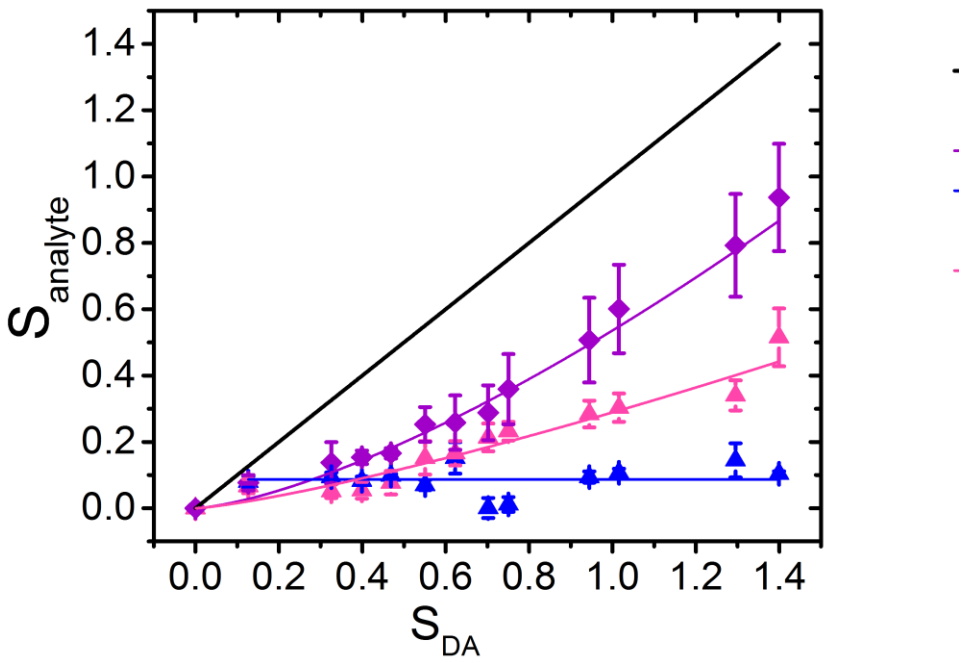

Figure 4.35 Correlation plots: signal response S recorded for [DA] (black line), [UA] (blue triangles), [DA] + UA 3 µM (purple lozenges) and [DA] + UA 30 µM (pink triangles) vs S for [DA].

This, together with the insensitivity of PEDOT:PSS to UA alone, suggests that UA may compete with PEDOT:PSS in the interaction with DA, thus DA decreasing the DA available to PEDOT:PSS. It turns out that the DA level of detection increases to 100pM when measured in [UA]=3 µM, and to 100 nM when measured in [UA]=30 µM . The agonist role of UA vs PEDOT:PSS towards DA is also apparent from the correlation plots in Figure 4.7b and Figure 4.8.

Finally, we tested the repeatability of our sensing strategy over 7 devices measured five times each resulting in a relative standard deviation of 2% (1.76 ± 0.04 ms) when the device is operated in PBS only and 14% (2.2 ± 0.3 ms for mixed solutions with AA and 2.3 ± 0.3 ms for mixed solutions with UA) when operated in mixed solutions. The deviation values are lower than the recommended value from the Association of Official Analytical Chemists (AOAC) (15%).[11,12]

We now discuss a possible origin for the selectivity of DA vs AA by our PEDOT:PSS based artificial synapse, that works even without a specific recognition moiety for DA. The sensing mechanism may rely on a preferential, stronger interaction of DA with PEDOT:PSS at the PEDOT:PSS/electrolyte interface. DA is a cation at physiological pH, thus two energetically favorable interactions take place: a π-π interaction between the aromatic rings of PEDOT:PSS and the DA catechol group on one hand, and a cation-π interaction between the ammonium group of DA and PEDOT:PSS on the other hand. PSS is a well-known

cation exchange polymer, and cations are also known to strongly interact with large π conjugated system as the one of PEDOT.[13] The latter interactions, that can be as high as hundred kJ mol^{-1}, can strongly distort the electronic density of states of the polymeric conductor, modulating the dynamics of current response. The inherent transient character of the STP measurement protocol allows sampling of this at-tractive interaction, and highlights it as an increase of the relaxation time τ_{STP}. Both AA and UA undergo the first protic dissociation at physiological conditions (pKa,1 = 4.7 and 5.4 respectively), hence they are anions at physiological conditions. Although they retain the π-π inter-action, which may explain the response of the device at the highest [AA], the negative charge leads to electrostatic repulsion with PSS. This may explain the shorter timescales τ_{STP} observed for both AA and UA with respect to DA, especially in the lowest concentration range. We have not elements either from literature or from our experiments to date, to discuss the interaction between DA and UA that competes with the one between DA and PEDOT:PSS. We just report it as a possible justification to these observations and aim to study it into more details in a follow-up.

4.3 NEUROMORPHIC ORGANIC DEVICES THAT SPECIFICALLY SENSE DOPAMINE VS ITS METABOLITES BY NON-SPECIFIC INTERACTIONS

In this work we tested the sensor towards the most important metabolites and neurotransmitters present in caudate-putamen extracellular fluid (ECF) (whose composition is similar to the one of the cerebrospinal fluid (CSF)). We demonstrated the specific label-free detection of DA with respect to the products of its catabolism and other catecholamine neurotransmitters produced by DA metabolic routes. This set of molecules is a challenging breadboard as they share comparable masses and charges, are present at ultra-low concentration levels in ECF and CSF and differ from one another only by a single functional group. In particular, at physiological pH, DA, 3-methoxytyramine (3-MT), norepinephrine (NE) and epinephrine (EPI) bear the same positive charge in the ammonium group,[14] and differ because of mono-methylation of the catechol (3-MT), the presence of hydroxyl group in beta position of the chain (NE and EPI), and methylation of the amino group (EPI).

The main result is that the STP response of our organic neuromorphic device to DA exhibits always longer STP timescales than the response to its catabolites and other catecholamine neurotransmitters. This implies that the device is sensitive not only to the presence of ionic charges, but also to more subtle differences in non-covalent interactions, each of a few kcal/mol. DFT calculations on a small cluster model of PEDOT:PSS rationalize the observed trend of STP timescales, offering a simple explanation in terms of

changes in hydrogen bonding and pi-stacking motives. Conversely, we find that the neuromorphic device is insensitive to 3,4-dihydroxyphenylacetic acid (DOPAC) and homovanillic acid (HVA) that according to their pK_a are anionic catabolites at physiological pH. This is expected by analogy with the sensing response of our device towards AA and UA.[15,16]

Table 4.2 Physiological concentrations of DA and DA metabolites in extracellular fluid (ECF) and cerebrospinal fluid (CSF).

Molecule	**Concentration (M)**		**Refs.**
	ECF	**CSF**	
Dopamine (DA)	$1.0x10^{-9}$ – $3.0x10^{-8}$	$9.0x10^{-11}$	[17,18]
3-Methoxytyramine (3-MT)	$4.0x10^{-9}$	$2.0x10^{-8}$	[19–21]
Homovanillic Acid (HVA)	$1.0x10^{-6}$	$1.5x10^{-7}$	[20,22,23]
3,4-Dihydroxyphenylacetic Acid (DOPAC)	$1.0x10^{-6}$	$2.8x10^{-7}$	[20,22]
Norepinephrine (NE)	$2.8x10^{-10}$	$3.7x10^{-10}$	[24,25]
Epinephrine (EPI)	$1.8x10^{-10}$	$1.5x10^{-10}$	[25,26]

4.3.1 Computational details

To strengthen our data, we performed Density Functional Theory (DFT) calculations. DFT calculations were performed using the PBE[27] functional as implemented in the TURBOMOLE suite of programs.[28] The resolution-of-identity (RI) technique has been used to speed up computations. Def-SVP basis set has been adopted for all atoms. To obtain reliable results in terms of geometry, orbital distribution and energy values, we performed geometry optimizations in implicit solvent (water) with Screening Model (COSMO) approach:[29] the system was solvated in water by setting the dielectric constant equal to 80. We adopted the empirical D3 dispersion correction proposed by Grimme62 to describe dispersion forces that are relevant to the model. Molecular orbitals and energy values for PEDOT (charge +1) and PSS (charge -1) models are in good agreement with previous works for describing the polaron state.[30,31] The Mulliken charges distribution of the system showed that most of the negative charge (-0.64) in PSS is localized on the sulfonate anion. Then, starting from PEDOT and PSS models, we converged to an optimized PEDOT:PSS model.

4.3.2 Comparison of STP response of DA and its metabolites

Figure 4.9 shows the experimental pulses and STP current response of a representative organic neuromorphic device. Monophasic (negative) rectangular voltage pulses $v_A(t)$ (blue line in Figure 4.9 a) are generated at the pre-synaptic electrode. The external applied voltage waveform generates a corresponding current waveform i_S (t) measured at the post-synaptic electrode. Initially, the current pulses have their origin at zero amps, however, with the application of subsequent pulses the current waveform begins to drift towards more negative values (Figure 4.9 a red line). Figure 4.9 b shows the behavior of the current upon the application of a very long train of voltages pulses. The envelope of the current peaks, both maxima and minima, decays rapidly within a few pulses and approaches a saturation limit after the application of several pulses. This behavior is often reported in the literature of neuromorphic devices.**6,65,66**

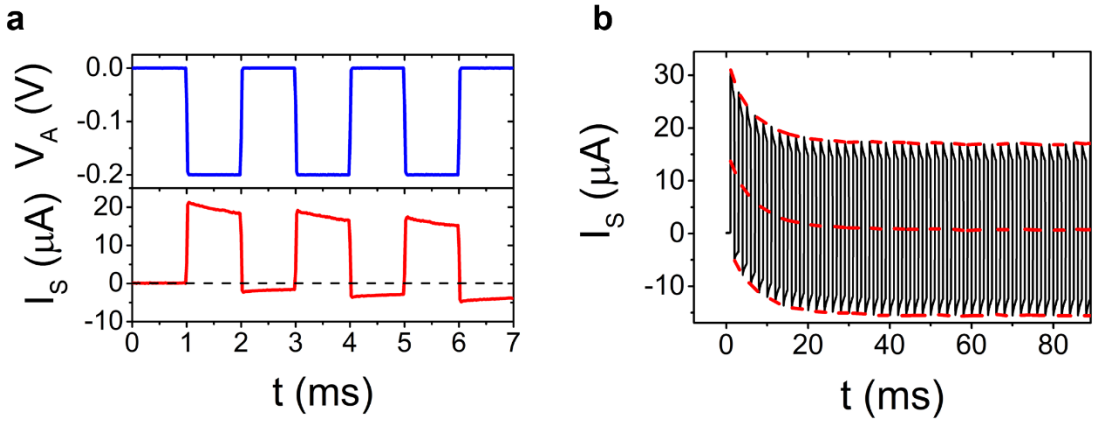

Figure 4.36 STP response of the neuromorphic device: (a) top blue line, the square voltage pulses generated by the pre-synaptic electrode; bottom red line, the current pulses produced at the post-synaptic electrode after application of voltage pulses. Notice the drift of the current base line and the current spikes, both drifting towards more negative values; (b) transient in the current waveform upon the application of unipolar voltage pulses at 500 Hz. Dashed red lines are the envelopes of the maxima, minima, and average value of the current peaks. In this case the best fit values according to eq.1 are: τ_{STP} = 7.40 ± 0.01 ms, I_∞ = 1.6777 ·10-5 ± 8·10-10 A and ΔI_0 = 1.568 ·10-5 ± 2·10-8 A for the upper envelope, τ_{STP} = 7.66 ± 0.01 ms, , I_∞ = 0.574 ·10-6 ± 5·10-10 and ΔI_0 = 1.412 ·10-5 ± 1·10-8 A for the average envelope and τ_{STP}=7.54 ± 0.01 ms, I_∞ = -1.5628 ·10-5 ± 7·10-10 A and ΔI_0 = 1.347 ·10-5 ± 1·10-8 A for the lower envelope.

We observed that the STP response timescale is modulated when a solute, that has a strong interaction with PEDOT:PSS, is introduced. Initially, the solute is partitioned between the solution and the electrodes. The first voltage pulse moves one of the electrodes out of equilibrium, causing either outflow or inflow (depending on the voltage sign) of ionic species at the polymeric electrode. Depending on the strength of the interaction, we expect the STP timescale to become greater as the interaction with the solute and its concentration gets larger.

In Figure 4.10 we show the signal *S* vs concentration for DA and its metabolites. For sake of clarity, in Figure 4.10 a we overlay the dose curves of DA with the ones from cationic species,[14] namely NE, 3-MT and EPI. Instead, Figure 4.10 b provides the comparison between the same DA dose curve as in Figure 4.10 a and the dose curves of anionic catabolites, DOPAC and HVA. We notice that the signal *S* associated to the presence of DA is always larger than the signal obtained in the presence of any metabolite, regardless of the net charge of the prevailing form, and also that the cations produce larger signal values than anions. Focusing on Figure 4.10 a, the fact that the dose curve of DA is always well above that from the cationic metabolites indicates a longer retention time across the whole range. It should also be noticed that both NE and 3-MT exhibit dose curves with a trend similar to that of DA, although they are shifted down vertically. Moreover, NE is always above the values of 3-MT. As the two catecholamines have similar pK_a values, we can infer that the methylation in 3-MT has a role in decreasing the interaction with PEDOT:PSS, with respect to NE. A possible reason is the steric hindrance of methyl group that weakens pi-stacking and prevents additional H-bond formation with the hydroxyl of the catechol group. The dose curve for EPI exhibits smoother variation, thus suggesting that the sterically hindered ammonium group in the secondary catecholamine is weakly coupled to PEDOT:PSS.

The comparison between DA and the anionic catabolites DOPAC and HVA in Figure 4.10 b supports our expectations, i.e., that the anionic catabolites exhibit much shorter retention times and their curves are largely superimposed, thus indicating that the interaction of both DOPAC and HVA with the electrode is rather non-specific.

To quantify the trends of the dose curves, we fit the signal *S vs* the molar concentration *C* of each substance as:

$$S = 1 - \exp\left[-\left(\frac{C}{C_0}\right)^n\right] \tag{4.5a}$$

whose first non-zero term is the power-law for $\frac{C}{C_0} \ll 1$:

$$S \approx \left(\frac{C}{C_0}\right)^n \tag{4.5b}$$

Hence the timescale can be approximated as:

$$\tau_{STP} \approx \tau_0 \left[1 + \left(\frac{C}{C_0}\right)^n\right] \quad (4.5c)$$

The characteristic molar concentration C_0 and the exponent *n* are two fitting parameters whose best fit values extracted from the linear fit of *lnS* vs *lnC* in Equation 4.5b, together with the estimated errors, are reported in Table 4.3. One can immediately notice that these parameters are characteristic of each metabolite and that the larger values of $1/C_0$ correlates with the longer characteristic timescales, in particular DA>NE>3-MT>DOPAC>HVA>EPI. According to equation 4.5a, C_0 represents an upper limit of detection, since the signal tends to saturation for $C \gg C_0$.

The sensitivity of each dose curve is estimated as the derivative of the best fit curve in Figure 4.10, viz. $\frac{dS}{dC} \approx \frac{n}{C_0}\left(\frac{C}{C_0}\right)^{n-1}$ hence is concentration-dependent. Because of the exponent n<1, the largest sensitivity is achieved at the lowest concentrations. Thus, in Table 4.3 we report the sensitivity values at the two limits of the patho-physiological concentration range of DA, viz. 100 pM and 10 nM. At the lower concentration, the sensitivity for DA, 3-MT, NE, is similar, while for EPI is one order of magnitude smaller.

Comparing the response to DA to the ones to HVA and to DOPAC in the patho-physiological concentration range, we observe that the dose curve response shows about 4 times lower sensitivity to the anionic form at physiological pH with respect to DA. This behavior is consistent with the one observed in our previous work with AA and UA.[15]

The DA curve also reveals a theoretical limit of detection, calculated as the mean blank signal value + three times the associated standard deviation, lower than 1 pM (while the lowest DA concentration tested is 1 pM) and 2-4 times larger sensitivity in the whole patho-physiological concentration range (from 100 pM to 10 nM) with respect to cationic catabolites or other catecholamine neurotransmitters.

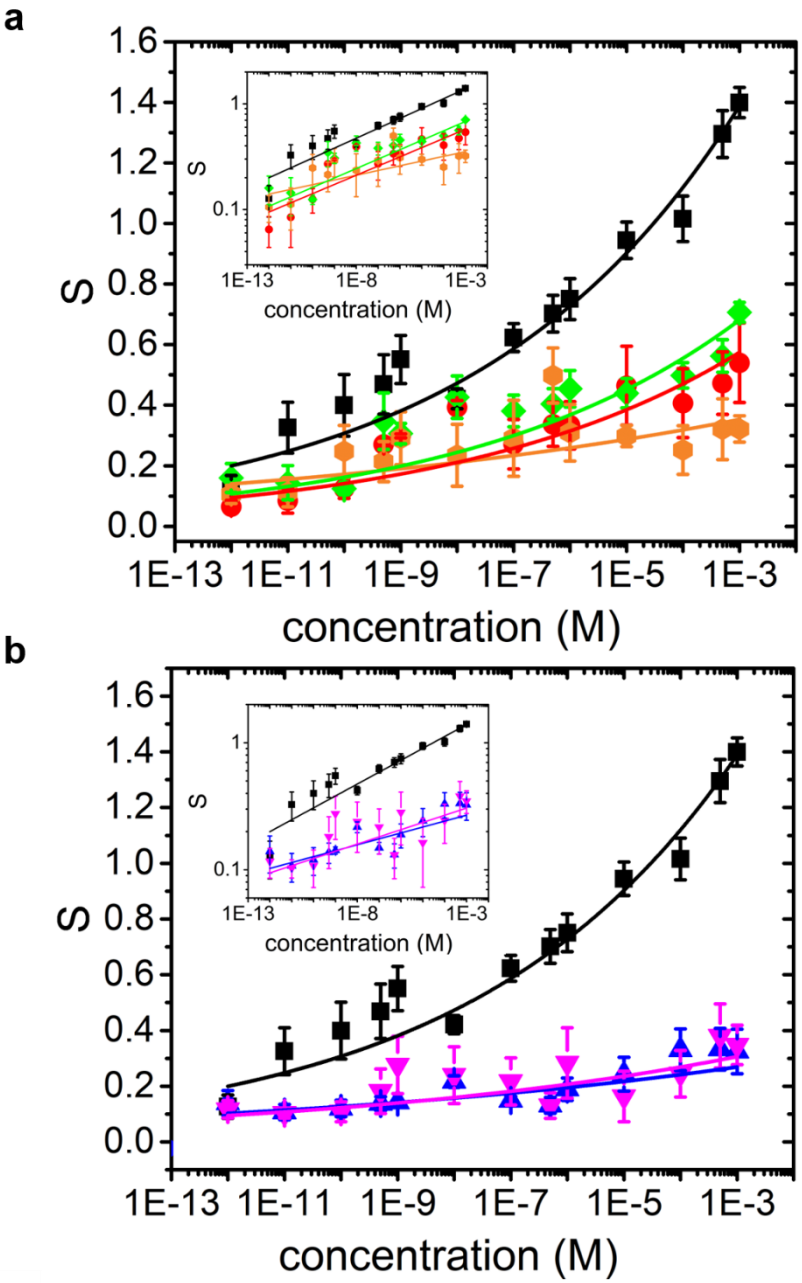

Figure 4.37 Signal S, lin-log plots for concentrations of DA (black squares) vs (a) cationic: 3-MT (red circles), NE (green lozenges) and EPI (orange hexagons), and (b) anionic catabolites: DOPAC (pink inverted triangles) and HVA (blue triangles). Error bars correspond to the SEM of S averaged over five devices. Continuous lines are functions $S=(C/C_0)^n$, where the parameters C_0 and n are obtained from linear regression as $lnS=(-n\cdot lnC0)+n\cdot lnC$. The insets showing the log-log plots of the main overlays evidence that the exponent n of DA, 3-MT, and NE takes similar values, the one of EPI is smaller, as well as the ones of the anionic catabolites DOPAC and HVA. In summary the ordering of n is DA≈ 3-MT ≈ NE >DOPAC≈HVA>EPI.

Table 4.3 Sensitivity in the patho-physiological range to the different DA catabolites, and best fit parameters of the dose curves.

Molecule	Sensitivity at 100 pM (M^{-1})	Sensitivity at 10 nM (M^{-1})	$\ln(C_0/M)$ $\pm \delta \ln(C_0/M)$	n
DA	2.9E+08	4.4E+06	-4.56±0.34	0.089±0.05
3-MT	1.4E+08	2.2E+06	-0.55±1.66	0.087±0.01
NE	1.6E+08	2.2E+06	-0.89±0.69	0.079±0.01
EPI	7.7E+07	9.4E+05	10.21±2.40	0.034±0.01
HVA	5.9E+07	7.3E+05	7.21±1.85	0.051±0.01
DOPAC	7.0E+07	9.0E+05	4.93±1.18	0.059±0.01

4.3.3 Correlation between binding energies and STP timescales

A molecular scale explanation of the observed selectivity of the STP response can be given by relating the timescales to non-equilibrium phenomena of transport and interaction within PEDOT:PSS. PEDOT:PSS exhibits an extended active interface with the electrolyte, that involves the whole volume. This characteristics was studied by Rivnay and co-workers and termed "volumetric capacitance of PEDOT:PSS".[32] At the outer interface with the electrolyte, PSS^- acts as a surfactant and does not contribute to the hole conductivity. Ion diffusion there occurs on a fast time-scale, the non-equilibrium state generated by the voltage pulses being then rapidly re-equilibrated. Conversely, at the PEDOT:PSS/electrolyte interface which lies deeper inside the film, where hole conduction takes place, ion diffusion is slowed down because of the longer pathways from the free electrolyte solution and constricted environment. The consequence is that a longer time is needed for the system to attain again equilibrium once it has been displaced from it upon a voltage pulse. If the time between pulses is short, the system cannot relax back to the absolute minimum of free energy, thus, pulse after pulse, the current drifts and the capacitance slowly changes. The out of equilibrium population at PEDOT:PSS interface produces the drift of conductance in time of the device. These arguments hint to the capacitance as the main contributor to the timescale τ_{STP} of the envelope Equation 4.10. This explanation seems consistent with the discussion reported later.

$$I_{env}(t) = I_\infty + \Delta I_0 \cdot e^{-t/\tau_{STP}} \qquad (4.10)$$

I_∞ is the long-time plateau, $I_\infty+\Delta I_0$ is the current response to the first voltage pulse, t is the time from that of the first voltage pulse t_0, and τ_{STP} is the characteristic relaxation time of the depressive response.[15]

The interaction of PEDOT:PSS with catabolites affects the timescale for their desorption from the active layer, hence the time scale that is exponentially related to the desorption free energy ΔG_{des} is exponentially contributed by the binding energy E_b of the molecule to PEDOT:PSS, in other words the enthalpic term ΔH_{des}=-E_b of the reaction PEDOT:PSS/DA -> DA + PEDOT:PSS.

Following the kinetic Eyring theory, in the transition state type of approach, a generic rate constant, ν, can be written as

$$\nu \propto exp\left(-\frac{\Delta G_{des}}{RT}\right) = exp\left(+\frac{\Delta S_{des}}{R}\right) \cdot exp\left(-\frac{\Delta H_{des}}{RT}\right) \qquad (4.11)$$
$$= exp\left(+\frac{\Delta S_{des}}{R}\right) \cdot exp\left(+\frac{\mathrm{E}_b}{RT}\right)$$

where the enthalpic term can be obtained by quantum chemical calculations of the purely electronic energies E_b. We then establish how E_b changes with the nature of the DA derivative. For this, we performed a DFT calculation, adopting a cluster model of the polymer with three styrene sulfonate (SS) and three monomers of 3,4-ethylenedioxythiophene (EDOT). The central SS is in the anionic form, offering a SO_3^- group towards PEDOT, while two lateral SS are protonated (SO_3H). Both PEDOT and PSS are truncated and capped with methyl groups. In this system, the overall charge is taken as 0, since PEDOT has a formal charge +1 and PSS -1. Defining the geometry of PEDOT:PSS is not trivial, therefore we first optimized the geometry of the single monomers and then used the resulting structures as starting point for optimizing the geometry of the pair.

The results of the DFT calculation show that for this minimum PEDOT:PSS model, the HOMO-LUMO energy gap is small (<1 eV), underlining the conductive character of the polymer. The HOMO and LUMO orbitals are mainly localized on PEDOT (see Figure 4.11). The binding energy of PSS^- to $PEDOT^+$ in water, calculated as the total energy of PEDOT:PSS minus the sum of the total energies of $PEDOT^+$ and of PSS^-, is -26.5 kcal/mol.

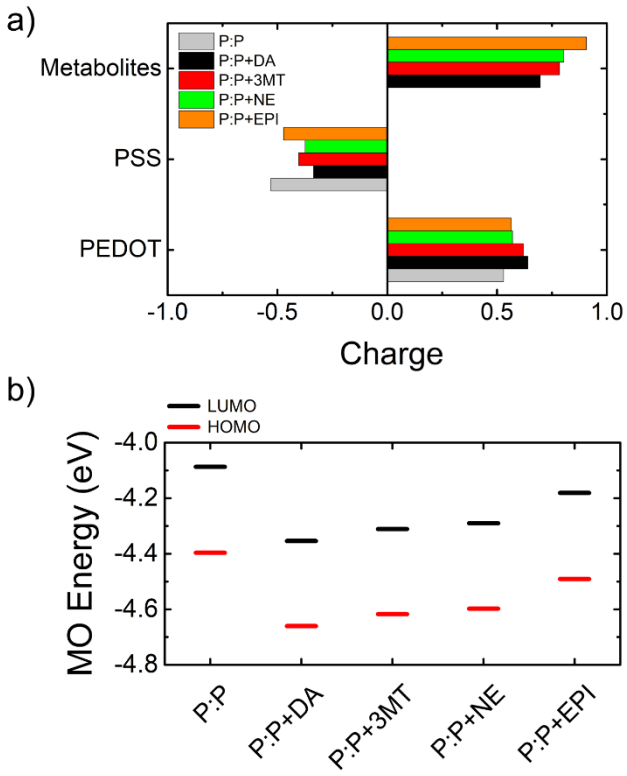

Figure 4.38 a) Mulliken charges populations on the metabolites, PEDOT and PSS. b) HOMO and LUMO orbitals of PEDOT:PSS and of PEDOT:PSS bound to Dopamine, 3-Methoxy-tyramine, Norepinephrine and Epinephrine.

To elucidate the mechanism, we investigated the binding of DA and other catabolites to PEDOT:PSS. In particular, we focused the attention of DFT calculations on the catabolites that are cations at the operational experimental pH (7.4). DA, NE and 3-MT feature a positively charged ammonium group. For this reason, we evaluated the electrostatic interaction and hydrogen bonds (H-bonds) formation between the sulfonate anion of PSS and the ammonium group of the catabolites.

In the initial geometry of the PEDOT:PSS/DA system, we placed the N atom of ammonium in DA 4.5 Å away from the sulfonate anion of PSS. Upon optimization in implicit solvent, the three H atoms of the ammonium group form three H-bonds: one with an oxygen of the central sulfonate anion, one with an oxygen of a lateral sulfonate and the last one with an oxygen atom of PEDOT (see Figure 4.12 and Table 4.4 for distances). The binding of the DA cation induces a decrease of the negative charge on PSS and an increase of positive charge on PEDOT, whose charge is less effectively compensated by PSS. The HOMO of the solvated system decreases upon DA binding and is partially localized on DA.

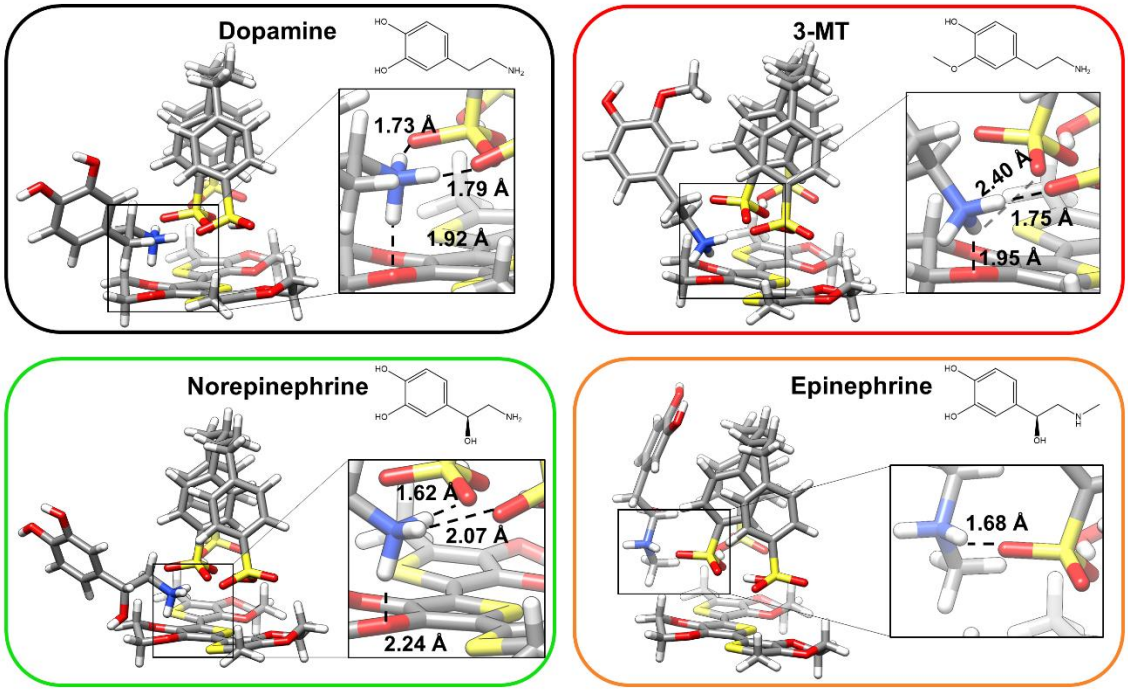

Figure 4.39 Binding of DA catabolites to PEDOT:PSS. Optimized structures of PEDOT:PSS(P:P) and catabolites: DA, 3MT, NE and EPI.

Table 4.4 Binding energies and bond distances for the interaction of the PEDOT:PSS model with DA and its cationic catabolites.

Catabolite bound to PEDOT:PSS	**Binding Energy (Kcal/mol)**	**H-bonds**
DA	-23.3	-NH_3^+---O(SS^-) = 1.73 Å - NH_3^+---O(SSH) = 1.79 Å - NH_3^+---O(PEDOT) = 1.92 Å
3-MT	-21.6	- NH_3^+---O(SS-) = 2.40 Å* - NH_3^+---O(SSH) = 1.95 Å* - NH_3^+---O(PEDOT) = 1.75 Å
NE	-19.9	- NH_3^+---O(SS-) = 1.62 Å - NH_3^+---O(SSH) = 2.07 Å - NH_3^+---O(PEDOT) = 2.24 Å
EPI	-9.3	- NH_3^+---O(SS-) = 1.68 Å

With same starting configuration, we then investigated the binding geometries and energies of 3-MT, NE, and EPI to PEDOT:PSS (Figure 4.12 and Table 4.4). Three H-bonds with PEDOT:PSS are also formed by 3-MT and NE. However, these H-bonds exhibit longer distances than those with DA, suggesting the presence of weaker bonds. EPI, which presents a methylated amine, can form only one weak bond with PSS. If we compare charges and orbitals of PEDOT:PSS with and without the catabolites (see figure 4.11), we can conclude that in our model, the PEDOT:PSS system is affected more by DA binding than by binding to the other catabolites and neurotransmitters.

As shown in Table 4, DA has the highest binding energy (-23.3 kcal/mol) to PEDOT:PSS, few kcal/mol more than 3-MT (-21.6 kcal/mol) and NE (-19.9 kcal/mol). EPI has much smaller binding energy, -9.3 kcal/mol, in line with the trend observed with charges and orbitals energies. These differences can be understood in terms of the contributions of the three H-bonds of the ammonium ion: in the case of 3-MT, the H-bond to the central SS- elongates substantially, while in the case of NE are the two side H-bonds to SSH and PEDOT that are weakened by the elongation. In the case of EPI, only the H-bond with SS^- forms. Calculations show that EPI has a much weaker interaction with PEDOT:PSS in agreement with the experimental data. The strong non-covalent binding, due to the interactions between the ammonium group of catecholamines and the sulfonate group is a conserved feature for the ammonium-terminated metabolites. The similar binding energies and charge distributions in the models where PEDOT:PSS is bound to DA, 3-MT or NE, suggest that the longer DA retention observed experimentally may be ascribed to other contributions, like π-stacking and cation-π interactions.

The results of DFT calculations evidence that DA forms the strongest bond with PEDOT:PSS. The ordering of the (absolute value of the) binding energy to PEDOT:PSS is

DA> 3-MT>NE>EPI.

This sequence resembles the ordering of $1/C_0$- and n- values fitting the dose curves from STP response.

4.3.4 Origin of STP timescale

We attempt a simple explanation for the origin of the observed STP timescales. Following kinetic Eyring theory, we can envision that the timescales governing the dynamics of ions interacting with a solid matrix arise from a distribution of free energy barriers, where the binding energy E_b is assumed to be the dominant enthalpic contribution. By neglecting possible differences in the entropic contribution and assuming that desorption of DA or metabolite is the rate limiting step, one expects at any concentration that an Arrhenius dependence between C_0 and E_b holds. We first write the STP time scale (in terms of

frequency ν) as emerging from the thermal average of individual processes governed by the Arrhenius dependence:

$$\langle \nu \rangle = \frac{1}{\tau_{STP}} = \frac{h}{RT} \sum_{sites\ i=1}^{N} \frac{N_{occ,i}}{N} exp\left(-\frac{\Delta G_{des,i}}{RT}\right) \approx A \frac{h}{RT} \sum_{sites\ i=1}^{N} \frac{N_{occ,i}}{N} exp\left(+\frac{E_{b,i}}{RT}\right) \qquad (4.12)$$

where $\frac{N_{occ,i}}{N}$ is the fraction of PEDOT:PSS sites occupied with binding energy $E_{b,i}$; it also termed population or occupancy. *A* is a constant containing the entropic contributions. The occupancy is then dependent on the concentration *C* and on the presence of competitors/antagonists that can subtract the binding sites upon a much stronger binding (e.g. divalent cations). By fixing the composition of the electrolyte solution, and assuming that the occupancy is smoothly energy-dependent, we can approximate the occupancy as being just a function of the concentration $\frac{N_{occ}}{N}(C)$ and neglect the variability with the specific site (energy). For a large number *N* of sites, a continuous average can replace the sum in Equation 4.12:

$$\begin{aligned} \langle \nu \rangle &= \frac{N_{occ}}{N}(C) \frac{h}{RT} \langle exp\left(-\frac{\Delta G_{des}}{RT}\right) \rangle \approx A \frac{N_{occ}}{N}(C) \frac{h}{RT} \langle exp\left(\frac{E_b}{RT}\right) \rangle \\ &= A \frac{N_{occ}}{N}(C) \frac{h}{RT} exp\left\{ \langle exp\left(\frac{E_b}{RT}\right) - 1 \rangle_c \right\} \end{aligned} \qquad (4.13)$$

The *c* subscript of the right-most identity implies the averaging of the Arrhenius factor in terms of the cumulant average of the term in bracket.[33,34] The first terms of the cumulant expansion are:

$$\langle \nu \rangle = A \frac{N_{occ}}{N}(C) \frac{h}{RT} exp\left\{ \frac{\langle E_b \rangle}{RT} \left[1 - \frac{1}{2RT} \frac{\sigma^2}{\langle E_b \rangle} + \frac{1}{6(RT)^2} \left(\frac{\langle {E_b}^3 \rangle - 3\sigma^2 \langle E_b \rangle - \langle E_b \rangle^3}{\langle E_b \rangle} \right) - \cdots . \right] \right\} \qquad (4.14)$$

The first term of the expansion in square brackets represents the "pure" Arrhenius behavior dependent only on the mean binding energy $\langle E_b \rangle$; the second term contains the second cumulant or variance $k_2=\sigma^2$ (square of the standard deviation σ); the third term is the third cumulant whose leading term is the skewness $\frac{\langle {E_b}^3 \rangle}{\sigma^3}$. Equation 4.13 states that the distribution of the binding energies (here described through its cumulants or combination of moments) introduces deviations from the "pure" Arrhenius behavior. The cumulants of order ≥2 quantify the "energy disorder". Based on this analogy, one we can state that "energy disorder" in the binding sites of the PEDOT:PSS layer introduces deviations from the expected 1/RT exponential rate. The consequence is that the exponential Arrhenius behavior transforms into a stretched exponential:

$$S \propto \tau_{STP} \propto exp\left[-\frac{1-f\left(\frac{\sigma^2}{\langle E_b\rangle};\ldots\right)}{RT}\langle E_b\rangle\right] \tag{4.15}$$

For a symmetric (central) distribution of the binding energy (for instance, gaussian energy disorder), then the only cumulant beyond the mean $\langle E_b\rangle$ surviving is the variance σ^2; if the active material is highly ordered, viz. $\sigma \to 0$, the Arrhenius behavior is recovered because the function $f \to 0$. Noticeably, for a gaussian or central distribution of the binding energy there is not deviation from the Arrhenius behavior, as the binding energy disappears in the second cumulant contribution and the cumulant correction enters only in the pre-exponential term. Then, it is non-central energy disorder with the third cumulant that introduces a non-Arrhenius correlation with the binding energy.

As we have described the signal *S* with the power law in equation 9b, then we expect a linear correlation of $-nlnC_0$ vs E_b, with the slope being smaller than the inverse thermal energy, that is 1.7 kcal/mol at RT, due to the energy disorder:

$$-nlnC_0 \ \propto -\frac{1-f\left(\frac{\sigma^2}{\langle E_b\rangle};\ldots\right)}{RT}\langle E_b\rangle \tag{4.16}$$

To confirm this prediction, in Figure 4.13 we plot $-nlnC_0$ vs the binding energy $-E_b$ from DFT (which is not necessarily the closest estimate for $<E_b>$ because of the simplicity of our model). We observe a positive correlation whose estimated slope (from the dashed straight line) is about 0.06 mol/kcal, i.e. smaller than 1/RT as it should be for a "pure" Arrhenius model. The model we propose is therefore that PEDOT:PSS is a material with a distribution of sites with different binding energies for the tested metabolites (thus not only with one binding energy) which originates an exponential correlation between the "mean" binding energy and the measured timescale. The deviation from a pure Arrhenius model is due to the disorder of the binding energy distribution. Above all, this correlation hints that both the microscopic origin of the differential response, as well as the sensitivity and resolution of the device, depend on the subtle differences of the binding energies of each molecule of this study with PEDOT:PSS. Interestingly, our simple DFT model provides a reasonable insight on the origin of the specific response, in particular, it hints to possibility of distinguishing differences in the binding energy with PEDOT:PSS of just a few kcal/mol.

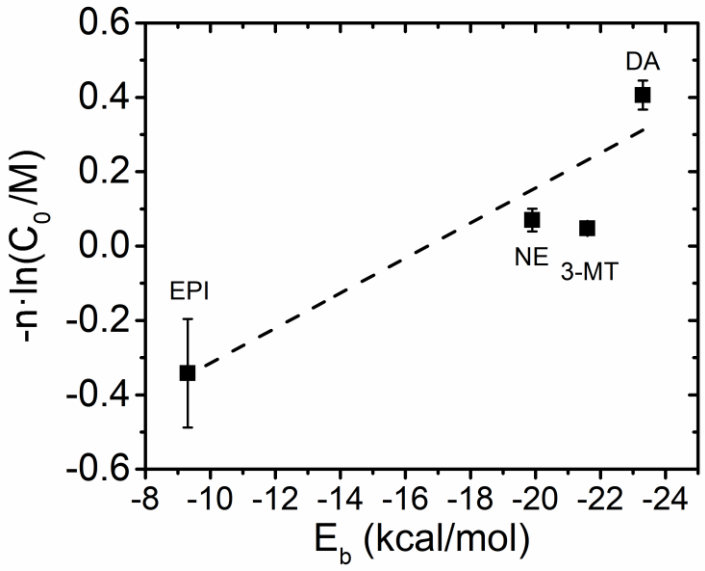

Figure 4.40 Correlation plot between the fitting parameters and the binding energy with PEDOT:PSS. The error bars are calculated from error propagation.

4.3.5 STP response

Finally, we comment on the meaning of the STP response in Figure 4.9 using a simple equivalent circuit (Figure 4.14 a), which allows us to establish a connection between macroscopic circuit properties and the microscopic interactions discussed in Section 4.3.3. The transient effect on the current waveform recorded at the post-synaptic terminal occurs because the input voltage signal is a short pulse. Here, short means that the period T of the input signal has to be shorter than 5 times the device time constant ($T<5\tau$). In circuit analysis, 5 τ is generally assumed as the time that must elapse after the impulse for the voltage across the capacitor to effectively reach the steady state. Upon these conditions the circuit requires several voltage pulses to reach the steady state, viz. the amount of charge flowing into the capacitor during charging half cycle equals the amount of charge flowing out of the capacitor during discharging half cycle.

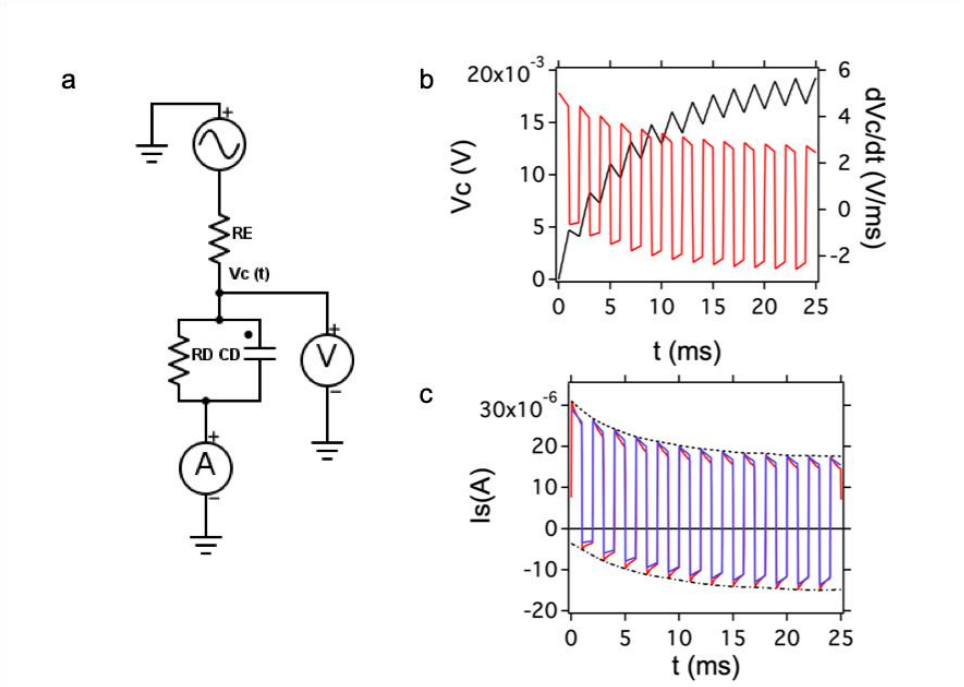

Figure 4.41 (a) The equivalent circuit adopted to describe the neuromorphic device exhibiting STP; the voltmeter measures the voltage $v_c(t)$; (b) time dependence of the voltage $v_c(t)$ across the capacitor from equation 13 (black line); the right axis shows the derivative obtained from equation 15 (red line); (c) STP current response from the equivalent circuit in (a) using equation 16 (blue line). Circuit parameters used are C_D=5.8 μF, R_D=1.4 kΩ and R_E=15.0 kΩ. The experimental curve (red line) shows deviations in the details of each peak. Dashed black and dashed-dotted black lines are the envelopes of the experimental STP maxima and minima of each spike, respectively.

By looking at the response to a few initial pulses at 500 Hz (Figure 4.9 a), one notices that the relaxation to the initial baseline current is prevented by the onset of the next voltage pulse that produces a progressively lower mean current. Accordingly, the peaks of the displacement current occur with the same pulse frequency but exhibit a progressively smaller (positive) value and a larger (negative) value. For many pulses (Figure 4.9 b), the envelopes of the peaks (maximum and minimum) exhibit an exponential decay in time to reach a plateau, and the mean current plateau is lower than the initial baseline current.

Since the transient effect shown in Figure 4.9 b is used as the relevant property for sensing, it is important to understand how the STP transient of the current waveform is affected by the analyte concentration as well as by the physical device parameters, like pulse amplitude V_0, duration Δt, frequency ν=1/T (T is the period), and number of pulses N_p. The duty cycle of the input signal is Δt /T.

To gain insight into the transient response observed, we chose to adopt an equivalent RC circuit, sketched in Figure 4.14 a. The parallel network comprising the resistance R_D and capacitance C_D accounts for the region dominated by the large capacitance of the PEDOT:PSS/electrolyte interface, in series with the

electrolyte region described here as the resistor R_E. In general, R_D and C_D are time-varying as a result of the dynamics of ions in and out of PEDOT:PSS. Hence, they are the most sensitive elements to the composition of the electrolyte solution as well as to the interactions of the solutes, the latter being dynamically partitioned between the solution and PEDOT:PSS. In order to obtain an analytical solution that reproduces the essential features of the sensing signals we take them as constant. We keep in mind, however, that even these "mean field" values must be regarded as characteristic of the nature of solute and concentration. A complete discussion on the choice of the components in the circuit, together with the exact solution as well as a dynamic model of ion-PEDOT:PSS interactions, will be presented elsewhere. Here we show that the circuit correctly predicts the transient response for a train of N_p square pulses.

When a single square voltage pulse is applied to the device, the overall current i_S (t) that flows through the system consists of two components, one resistive flowing through R_D and the other capacitive through C_D:

$$i_S(t) = \frac{v_C(t)}{R_D} + C_D \frac{dv_C(t)}{dt} \qquad (4.17)$$

To calculate i_s (t) one needs to solve the differential Equation 4.17 for the voltage v_C (t). The analytical solution is given in terms of the time constant τ:

$$\tau = \frac{R_D R_E C_D}{R_D + R_E} \qquad (4.18)$$

Equation 4.18 is the time constant of an RC circuit with an effective resistance consisting of two in-series resistors.

The first pulse yields the voltage:

$$v_C(t) = V_0 \frac{R_D}{R_D + R_E}\left[1 - e^{-\frac{t}{\tau}}\right] \quad \text{for } 0 \le t \le \Delta t \qquad (4.19a)$$

$$v_C(t) = V_0 \frac{R_D}{R_D + R_E} e^{-\frac{t}{\tau}}\left[e^{\frac{\Delta t}{\tau}} - 1\right] \text{ for } \Delta t < t \le T \qquad (4.19b)$$

Equation 4.19a applies when the voltage pulse is on, viz. during charging, while equation 4.19b applies during the lag time when the capacitor is discharging. At the end of the first pulse, viz. at the period $T = 1/\nu$ where ν is the pulse repetition frequency, the residual voltage is:

$$v_C(T) = V_0 \cdot \frac{R_D}{R_D + R_E} \cdot e^{-\frac{T}{\tau}} \left(e^{\frac{\Delta t}{\tau}} - 1 \right) \tag{4.20}$$

This is the voltage at which the second pulse starts. We notice that only when T>>Δt, the next pulse starts from $v_C(0)$=0 volt, else its value depends on the voltage divider (i.e. the two resistors), as well as on the ratio between τ and the frequency/duty cycle. The sign of $v_C(t)$ will be the same of the input pulse V_0.

For $N_p \geq 2$, a recursion solution is found. The voltage built upon $n+1=N_p$ pulses reads:

$$v_C(nT) = v_C(T) \left[\frac{1 - e^{-\frac{nT}{\tau}}}{1 - e^{-\frac{T}{\tau}}} \right] \tag{4.21}$$

Equation 4.21 encompasses both Equation 4.20 for n=1, and $v_C(0)$=0 V for n=0. Then the voltage $v_C(t)$ can be written as:

$$v_C(t) = v_C(nT) \cdot e^{-\frac{t-nT}{\tau}} + V_0 \frac{R_D}{R_D + R_E} \left[1 - e^{-\left(\frac{t-nT}{\tau}\right)} \right] \text{ for } nT \leq t \leq nT + \Delta t \tag{4.22a}$$

$$v_C(t) = \left[v_C(nT) + v_C(T) e^{\frac{T}{\tau}} \right] e^{-\frac{t-nT}{\tau}} \text{ for } nT + \Delta t < t \leq (n+1)T \tag{4.22b}$$

The combination of Equations 4.22a and 4.22b results in the voltage waveform plotted in Figure 4.14 b left axis for an V = 37mV applied at the second electrode. The variance of this value with 0.2 V applied experimentally at the first electrode is ascribed to the oversimplification of the equivalent circuit in Figure 4.14 a. The value found must be regarded as an effective potential that is divided across the network of

the resistors in the circuit, also the ones not accounted for here, as for instance contact and bulk resistances. We notice that the voltage rises and decays within a pulse has the same dynamics and the same time constant □. The difference between the maximum and minimum voltages achieved at the pulse n+1 is then obtained by plugging *t=nT+* Δt in equation 4.21a and *t=(n+1)T* in Equation 4.22b (else taking Equation 4.21) respectively:

$$v_{C,max}(n) - v_{C,min}(n) = \left[v_C(nT) + v_C(T)e^{\frac{T}{\tau}}\right] \cdot \left[e^{-\frac{\Delta t}{\tau}} - e^{-\frac{T}{\tau}}\right] \quad (4.23)$$

Equation 4.23 shows that this difference, that determines the current spike amplitude, can be maximized with the input frequency and duty cycle. It is also evident that the envelope passing through the maxima (obtained from Equation 4.22a) or the minima (as from Equation 4.22b) exhibits an exponential trend, whose characteristic time scale equals τ.

To obtain the current, we need first to calculate the derivative of Equation 4.22 shown in Figure 4.14 b, right axis:

$$\frac{dv_C(t)}{dt} = \left[\frac{V_0}{\tau}\frac{R_D}{R_D+R_E} - \frac{v_C(nT)}{\tau}\right] e^{-\left(\frac{t-nT}{\tau}\right)} \quad (4.24a)$$

for $nT \le t \le nT + \Delta t$

$$\frac{dv_C(t)}{dt} = -\frac{v_C(t)}{\tau} \text{ for } nT + \Delta t < t \le (n+1)T \quad (4.24b)$$

then we combine Equations 4.22 a (b) and 4.24 a (b) into Equation 4.17 to yield:

$$i_S(t) = \frac{V_0}{R_D+R_E} - \left[\frac{V_0}{R_D+R_E} - \frac{V_0}{R_E} + \frac{v_C(nT)}{R_E}\right] e^{-\frac{t-nT}{\tau}} \quad (4.25a)$$

for $nT \le t \le nT + \Delta t$

$$i_S(t) = -\frac{v_C(t)}{R_E} = -\frac{\left[v_C(nT)+v_C(T)e^{\frac{T}{\tau}}\right]}{R_E} e^{-\frac{t-nT}{\tau}} \qquad (4.25b)$$

$$for\ nT + \Delta t < t \leq (n+1)T$$

In Figure 4.14 c we show the current waveform as obtained from Equation 4.25 for the following parameters: C_D=5.8 μF, R_E=1.4 kΩ, and R_D=15.0 kΩ. The time constant equation 17 is τ=7.4 ms in agreement with the value obtained by best fit. We compare it first to the time derivative $dv_c(t)/dt$ of the potential (right axis in Figure 4.14 b) to infer that the trend is largely dictated by the capacitive contribution to the current **equation 16**, however the shape of the current spike and the exponential trend within each peak is more affected by the resistive contributions and fails to closely follow the details. Noticeably, by comparing it to the envelope fitted on the recorded current in Figure 4.9b (reported in Figure 4.14 c as a dashed line), we find an excellent agreement. Maxima and minima of each current spike read:

$$i_S(nT + \Delta t) = i_{S,min} = \frac{V_0}{R_D+R_E} - \left[\frac{V_0}{R_D+R_E} - \frac{V_0}{R_E} + \frac{v_C(nT)}{R_E}\right] e^{-\frac{\Delta t}{\tau}} \qquad (4.26a)$$

$$i_S\big((n+1)T\big) = i_{S,max} = -\frac{\left[v_C(nT)e^{-\frac{T}{\tau}}+v_C(T)\right]}{R_E} \qquad (4.26b)$$

Noticeably, the inverse exponential decay rate of either the maxima or the minima from Equation 4.26, are both equal to the inverse time decay rate of $v_C(nT)$ in Equation 4.20, viz. τ. Thus, we infer that our observable from the current peaks envelope is $\tau_{STP} \approx \tau$. This justifies our choice to relate τ_{STP} to the solute composition, as we stated that, even in this simplistic equivalent circuit description of the device, C_D and R_D are to be regarded as composition-sensitive circuit elements.

A few final considerations are useful:

i) by choosing T=2 ms, compared to τ=7.4 ms, it is necessary to supply $N_p \geq 5\tau/T \approx$ 18 pulses to achieve the steady state, in agreement with Figure 3b;

ii) the maximum STP is quantified as the difference between the maximum peak current at *t=Δt* and the maximum at the steady state for *t=nT* with n>>18:

$$\Delta i_S = i_S(\Delta t) - \lim_{n\to\infty} i_S(nT+\Delta t) = \frac{V_0}{R_D+R_E} - \left[\frac{V_0}{R_D+R_E} - \frac{V_0}{R_E}\right] e^{-\frac{\Delta t}{\tau}} - \\ -\frac{V_0}{R_D+R_E} + \lim_{n\to\infty}\left[\frac{V_0}{R_D+R_E} - \frac{V_0}{R_E} + \frac{v_C(nT)}{R_E}\right] e^{-\frac{\Delta t}{\tau}} = \\ \lim_{n\to\infty} \frac{v_C(nT)}{R_E} e^{-\frac{\Delta t}{\tau}} = \frac{v_C(T)}{R_E} \frac{e^{-\frac{\Delta t}{\tau}}}{1-e^{-\frac{T}{\tau}}} \tag{4.27}$$

By plugging Equation 4.20 into Equation 4.15 the simplified form is obtained:

$$\Delta i_S(T,\Delta t\,) = \frac{V_0}{R_D+R_E} \cdot \frac{R_D}{R_E} \cdot e^{-\frac{T}{\tau}} \left[\frac{1-e^{\frac{-\Delta t}{\tau}}}{1-e^{-\frac{T}{\tau}}}\right] \tag{4.28}$$

Equation 4.28 reveals that the STP response is strongly damped in one of the following cases when:

a) $R_E >> R_D$;

b) $T >> \tau$;

c) the duty cycle is very small, $\Delta t/T \to 0$.

These observations lead us to conclude that:

- The induction of STP requires either high ionic strength electrolyte solution to make R_E small, or an active material with high resistance R_D, for instance an organic semiconductor instead of the usual organic conductor;
- Capacitance C_D must be large, thus large area electrodes with small channel, else high surface area nanostructured electrodes, may perform better (albeit as C_D increases also R_D decreases).
- For each τ there is a threshold pulse frequency;

- Judicious doping to increase R_D can be used for tailoring STP.
- The STP response is larger at small T/t, but a greater number of voltage pulses is needed to observe it.
- There is an optimum period T_s that maximizes $\Delta i_S(T_s, \Delta t)$.

(1) Alibart, F.; Pleutin, S.; Bichler, O.; Gamrat, C.; Serrano-Gotarredona, T.; Linares-Barranco, B.; Vuillaume, D. A Memristive Nanoparticle/Organic Hybrid Synapstor for Neuroinspired Computing. *Adv. Funct. Mater.* **2012**, *22* (3), 609–616. https://doi.org/10.1002/adfm.201101935.

(2) Desbief, S.; di Lauro, M.; Casalini, S.; Guerin, D.; Tortorella, S.; Barbalinardo, M.; Kyndiah, A.; Murgia, M.; Cramer, T.; Biscarini, F.; et al. Electrolyte-Gated Organic Synapse Transistor Interfaced with Neurons. *Org. Electron.* **2016**, *38*, 21–28. https://doi.org/10.1016/j.orgel.2016.07.028.

(3) Ishikawa, F. N.; Curreli, M.; Chang, H. K.; Chen, P. C.; Zhang, R.; Cote, R. J.; Thompson, M. E.; Zhou, C. A Calibration Method for Nanowire Biosensors to Suppress Device-to-Device Variation. *ACS Nano* **2009**, *3* (12), 3969–3976. https://doi.org/10.1021/nn9011384.

(4) Bucher, E. S.; Wightman, R. M. Electrochemical Analysis of Neurotransmitters. *Annu. Rev. Anal. Chem.* **2015**, *8* (1), 239–261. https://doi.org/10.1146/annurev-anchem-071114-040426.

(5) Raj, C. R.; Okajima, T.; Ohsaka, T. Gold Nanoparticle Arrays for the Voltammetric Sensing of Dopamine. *J. Electroanal. Chem.* **2003**, *543* (2), 127–133. https://doi.org/10.1016/S0022-0728(02)01481-X.

(6) Sun, C. L.; Lee, H. H.; Yang, J. M.; Wu, C. C. The Simultaneous Electrochemical Detection of Ascorbic Acid, Dopamine, and Uric Acid Using Graphene/Size-Selected Pt Nanocomposites. *Biosens. Bioelectron.* **2011**, *26* (8), 3450–3455. https://doi.org/10.1016/j.bios.2011.01.023.

(7) Berto, M.; Casalini, S.; Di Lauro, M.; Marasso, S. L.; Cocuzza, M.; Perrone, D.; Pinti, M.; Cossarizza, A.; Pirri, C. F.; Simon, D. T.; et al. Biorecognition in Organic Field Effect Transistors Biosensors: The Role of the Density of States of the Organic Semiconductor. *Anal. Chem.* **2016**, *88* (24), 12330–12338. https://doi.org/10.1021/acs.analchem.6b03522.

(8) Wightman, R. M.; May, L. J.; Michael, a C. Detection of Dopamine Dynamics in the Brain. *Anal. Chem.* **1988**, *60* (13), 769A-779A. https://doi.org/10.1021/ac00164a001.

(9) Capella, P.; Ghasemzadeh, B.; Mitchell, K.; Adams, R. N. Nafion-Coated Carbon Fiber Electrodes for Neurochemical Studies in Brain Tissue. *Electroanalysis* **1990**, *2* (3), 175–182. https://doi.org/10.1002/elan.1140020303.

(10) Crotty, G. F.; Ascherio, A.; Schwarzschild, M. A. Targeting Urate to Reduce Oxidative Stress in Parkinson Disease. *Exp. Neurol.* **2017**, *298*, 210–224. https://doi.org/10.1016/j.expneurol.2017.06.017.

(11) Horowitz, W.; Latimer, G. W. *Official Methods of Analysis of AOAC International*; Gaithersburg, Maryland : AOAC International, 2006.

(12) Mettakoonpitak, J.; Miller-Lionberg, D.; Reilly, T.; Volckens, J.; Henry, C. S. Low-Cost Reusable Sensor for Cobalt and Nickel Detection in Aerosols Using Adsorptive Cathodic Square-Wave Stripping Voltammetry. *J. Electroanal. Chem.* **2017**, *805*, 75–82. https://doi.org/10.1016/j.jelechem.2017.10.026.

(13) Dougherty, D. A. The Cation-π Interaction. *Acc. Chem. Res.* **2013**, *46* (4), 885–893. https://doi.org/10.1021/ar300265y.

(14) Granot, J. Nmr Studies of Catecholamines. Acid Dissociation Equilibria in Aqueous Solutions. *FEBS Lett.* **1976**, *67* (3), 271–275. https://doi.org/10.1016/0014-5793(76)80545-5.

(15) Giordani, M.; Berto, M.; Di Lauro, M.; Bortolotti, C. A.; Zoli, M.; Biscarini, F. Specific Dopamine Sensing Based on Short-Term Plasticity Behavior of a Whole Organic Artificial Synapse. *ACS Sensors* **2017**, *2* (12), 1756–1760. https://doi.org/10.1021/acssensors.7b00542.

(16) Giordani, M.; Di Lauro, M.; Berto, M.; Bortolotti, C. A.; Vuillaume, D.; Gomes, H. L.; Zoli, M.; Biscarini, F. Whole Organic Electronic Synapses for Dopamine Detection; Kymissis, I., Shinar, R., Torsi, L., Eds.; 2016; Vol. 9944, p 99440P. https://doi.org/10.1117/12.2239532.

(17) Venton, B. J.; Zhang, H.; Garris, P. A.; Phillips, P. E. M.; Sulzer, D.; Wightman, R. M. Real-Time Decoding of Dopamine Concentration Changes in the Caudate-Putamen during Tonic and Phasic Firing. *J. Neurochem.* **2003**, *87* (5), 1284–1295. https://doi.org/10.1046/j.1471-4159.2003.02109.x.

(18) Goldstein, D. S.; Holmes, C.; Sharabi, Y. Cerebrospinal Fluid Biomarkers of Central Catecholamine Deficiency in Parkinson's Disease and Other Synucleinopathies. *Brain* **2012**, *135* (6), 1900–1913. https://doi.org/10.1093/brain/aws055.

(19) Wester, P.; Bergström, U.; Eriksson, A.; Gezelius, C.; Hardy, J.; Winblad, B. Ventricular Cerebrospinal Fluid Monoamine Transmitter and Metabolite Concentrations Reflect Human Brain Neurochemistry in Autopsy Cases. *J. Neurochem.* **1990**, *54* (4), 1148–1156. https://doi.org/10.1111/j.1471-4159.1990.tb01942.x.

(20) Johnson, J. A.; Wightman, R. M. Cyclic Voltammetric Measurements of Neurotransmitters. *Electrochem. Soc. Interface* **2017**, *26* (3), 53–57. https://doi.org/10.1149/2.F06173if.

(21) Nardes, A. M.; Kemerink, M.; Janssen, R. A. J.; Bastiaansen, J. A. M.; Kiggen, N. M. M.; Langeveld, B. M. W.; Van Breemen, A. J. J. M.; De Kok, M. M. Microscopic Understanding of the Anisotropic Conductivity of PEDOT:PSS Thin Films. *Adv. Mater.* **2007**, *19* (9), 1196–1200. https://doi.org/10.1002/adma.200602575.

(22) Markianos, E. S.; Nyström, I.; Reichel, H.; Matussek, N. Serum Dopamine-β-Hydroxylase in

Psychiatric Patients and Normals. Effect of d-Amphetamine and Haloperidol. *Psychopharmacology (Berl).* **1976**, *50* (3), 259–267. https://doi.org/10.1007/BF00426842.

(23) Jimerson, D. C.; Lesem, M. D.; Kaye, W. H.; Brewerton, T. D. Low Serotonin and Dopamine Metabolite Concentrations in Cerebrospinal Fluid from Bulimic Patients with Frequent Binge Episodes. *Arch. Gen. Psychiatry* **1992**, *49*, 132–138. https://doi.org/10.1001/archpsyc.1992.01820020052007.

(24) Christensen, N. J.; Vestergaard, P.; Sørensen, T.; Rafaelsen, O. J. Cerebrospinal Fluid Adrenaline and Noradrenaline in Depressed Patients. *Acta Psychiatr. Scand.* **1980**, *61* (2), 178–182. https://doi.org/10.1111/j.1600-0447.1980.tb00577.x.

(25) Menon, J. M. L.; Nolten, C.; Achterberg, E. J. M.; Joosten, R. N. J. M. A.; Dematteis, M.; Feenstra, M. G. P.; Drinkenburg, W. H. (Pim); Leenaars, C. H. C. Brain Microdialysate Monoamines in Relation to Circadian Rhythms, Sleep, and Sleep Deprivation – a Systematic Review, Network Meta-Analysis, and New Primary Data. *J. Circadian Rhythms* **2019**, *17* (1), 1–32. https://doi.org/10.5334/jcr.174.

(26) Peskind, E. Cerebrospinal Fluid Epinephrine in Alzheimer's Disease and Normal Aging. *Neuropsychopharmacology* **1998**, *19* (6), 465–471. https://doi.org/10.1016/S0893-133X(98)00054-2.

(27) Perdew, J. P.; Burke, K.; Ernzerhof, M. Perdew, Burke, Ernzerhof - 1997 - Generalized Gradient Approximation Made Simple(2). **1996**, No. 3, 3865–3868.

(28) Ahlrichs, R.; Bär, M.; Häser, M.; Horn, H.; Kölmel, C. Electronic Structure Calculations on Workstation Computers: The Program System Turbomole. *Chem. Phys. Lett.* **1989**, *162* (3), 165–169. https://doi.org/10.1016/0009-2614(89)85118-8.

(29) Klamt, A. Conductor-like Screening Model for Real Solvents: A New Approach to the Quantitative Calculation of Solvation Phenomena. *J. Phys. Chem.* **1995**, *99* (7), 2224–2235. https://doi.org/10.1021/j100007a062.

(30) Gangopadhyay, R.; Das, B.; Molla, M. R. How Does PEDOT Combine with PSS? Insights from Structural Studies. *RSC Adv.* **2014**, *4* (83), 43912–43920. https://doi.org/10.1039/c4ra08666j.

(31) Marutaphan, A.; Seekaew, Y.; Wongchoosuk, C. Self-Consistent Charge Density Functional Tight-Binding Study of Poly(3,4-Ethylenedioxythiophene): Poly(Styrenesulfonate) Ammonia Gas Sensor. *Nanoscale Res. Lett.* **2017**, *12* (1). https://doi.org/10.1186/s11671-017-1878-2.

(32) Rivnay, J.; Leleux, P.; Ferro, M.; Sessolo, M.; Williamson, A.; Koutsouras, D. a.; Khodagholy, D.; Ramuz, M.; Strakosas, X.; Owens, R. M.; et al. High-Performance Transistors for Bioelectronics

through Tuning of Channel Thickness. *Sci. Adv.* **2015**, *1* (4), e1400251–e1400251. https://doi.org/10.1126/sciadv.1400251.

(33) Kubo, R. Generalized Cumulant Expansion Method. *J. Phys. Soc. Japan* **1962**, *17* (7), 1100–1120. https://doi.org/10.1143/JPSJ.17.1100.

(34) Van Kampen, N. G. *Stochastic Processes in Physics and Chemistry*; North Holland, 2007.

5 CONCLUSION AND PERSPECTIVES

We demonstrated that the current response of a device made of two PEDOT:PSS electrodes is selective for DA even without specific recognition moieties. The dynamic measurement of the STP transient current allows us to discriminate DA from other chemical species that are produced from DA metabolic and catabolic pathways and from the classical electrochemical interferings. The breakthrough is in recognizing that the STP decay time τ_{STP} is a characteristic parameter of a given solute, which allows us to parametrize it in terms of a power law of the concentration. If on one hand we expected differences in response between DA and anionic molecules because of the negative charges at a physiological pH, we were positively surprised about the fact that DA gives rise to time scales substantially different than those of other cationic species; in fact, HVA and DOPAC signals are 4 times lower with respect to the cationic DA. The important result was to demonstrate that there is also a substantially different response also for the cationic catabolites and neurotransmitters, that exhibit just small structural differences with respect to DA like one methyl or hydroxyl group. The DFT calculations on a simple model of PEDOT:PSS binding DA or the cationic metabolites individually confirmed that DA gives rise to the strongest non covalent interaction with PEDOT:PSS followed by 3-MT, NE and EPI, respectively. Then we demonstrated with a simple adaptation of Eyring theory to the desorption of the interacting molecules with PEDOT:PSS, that an exponential correlation exists between the signal and the binding energy, although is not an ideal Arrhenius due to the distribution of the binding energies in PEDOT:PSS. This correlation, with the caveat that neglects other important phenomena like diffusion across a multiscale porous material like PEDOT:PSS, hint a simple way to rationalize the observed sequence of the timescales, as well as the microscopic origin of the selectivity, viz. an exponential response to binding energies that may differ of a few kcal/mol

In order to better understand the origin of these differences in STP, we have solved a simple RC circuit pulsed with train of square pulses, to show that the current response is very much alike the one produced by our artificial synapse, and that the timescale τ depends on the capacitance and the in-series resistances of the circuit. The simplest rationale of this approach as a new sensing framework then lies in the change of the resistance and capacitance of the PEDOT:PSS interface by the different interactions with the solute present in the electrolyte solution. A more physical description should keep into account the dynamics of ions in and out of the PEDOT:PSS film, thus introducing time-varying capacitance and resistance. At the present level, we are assuming that their “mean” values account semi-quantitatively for the observed STP behavior. The value of this simple model is on the indication of sensitive parameters that would allow one to enhance the STP response. The important message from the simple circuit is that the STP response is

not obtained always, but only at some “sufficiently high” frequency, and some rough figures of merit for the parameters are identified.

The novelty and relevance of this work lie in the demonstration that is possible to make selective sensor devices based on non-covalent interactions also in the absence of recognition groups coupled to the active elements of the device. This recognition scheme is completely general, since it requires first a different partition of the solute between the solution and PEDOT:PSS, and then different ion dynamics in and out the polymeric electrodes. The exponential correlation between the experimental STP timescale and the binding energy of DA metabolites interacting with PEDOT:PSS indicates that the slower dynamics of ionic species in and out PEDOT:PSS upon voltage pulsing might be the origin, or an important contribution, of the neuromorphic STP response of the device. Our sensing framework can discriminate differences of non-specific interactions with the active material as small as a few kcal/mol, else corresponding to one functional group in the molecular structure. However, we cannot assess at this level other important effects related for instance to the dynamics/transport of the relevant molecule from/to the electrolyte to the PEDOT:PSS active binding sites.

Our observation and the rationale behind it suggest that homolog series of a certain species (e.g. alcohols, aldehydes or carboxylic acids with different chain lengths and/or steric hindrance), could be discriminated within their group due to this exponential amplification into the transient current of small differences in the binding energy with PEDOT:PSS. We may expect that by changing the counterion, it would be possible to extend this new type of spectroscopic sensing to other homolog families, also not endowed with H-bond forming moieties. Potential benchmark systems include perfluorinated compounds and aromatic molecules. It is also likely that an optimum frequency, that maximizes the differential STP response for each molecule of interest, exists and that the approach could be viable to identify “spectroscopically” the target analytes. In this respect, a seemingly relationship must exist between the response of STP sensors, driven at one frequency, and electrochemical impedance spectroscopy.

6 APPENDIX

The following chapter is dedicated to side works I did during my PhD. These works were finalized to improve or standardize techniques that I used for the main work.

In particular, this chapter is taken by the paper:

''Di Lauro et al., Advanced Electronic Materials, 3(9), 1700159, (2017)''

6.1 Liquid-Gated Organic Electronic Devices Based on High-Performance Solution-Processed Molecular Semiconductor

6.1.1 Introduction

Liquid-gated organic transistors are emerging as ultrasensitive devices for the detection of biomarkers,[1–3] ions,[4,5] and molecular analytes[6,7] as well as for the transduction of bioelectrical signals.[8,9] The gate electrode in these devices is immersed in a liquid phase, typically an aqueous electrolytic solution; application of a gate potential (V_{GS}) results in the build-up of two electrical double layers (at the gate/electrolyte and electrolyte/active material interfaces) which are responsible of charge modulation in the semi-conductive organic layer and of the subsequent change of the source-drain current (I_{DS}). Amongst a variety of architectures used as organic-electronic bio-sensors, the lowest detection levels (i.e. minimum detectable variations in analyte concentration) were obtained with Electrolyte-Gated Organic Field-Effect Transistors (EGOFETs)[1,6,10–12] operated in accumulation mode with pentacene,[1,3,6] α-sexithiophene,[13,14] and poly(3-hexylthiophene-2,5-diyl) (P3HT)[10] channels. Figure 6.1 a shows the schematic layout of EGOFETs. A quantitative estimator of the sensitivity of a transistor as a sensor is the transconductance gm defined as the derivative of the transfer characteristics $\partial I_{DS}/\partial V_{GS}$. In the linear regime the transconductance reads as:

$$g_m = \frac{\delta I_{DS}}{\delta V_{GS}} = \frac{W}{L}\mu C_{eff} V_{DS} \qquad (6.1)$$

In Equation 1 W and L are channel width and length, C_{eff} is the effective areal capacitance, μ is the charge carrier mobility and V_{DS} is the potential difference between Source and Drain electrodes. Albeit it is not obvious that equation 6.1, derived for thin film transistors with solid-state dielectrics, can be adopted for EGOFET, this equation hints to the fact that high field-effect mobility is desirable for devising transistors with high sensitivity.

High transconductance in EGOFET-based sensors is ascribed to the intrinsic large capacitive coupling between gate electrode and semiconductor that enables device operations with voltage V_{GS} ranging from a few tens up to a few hundred mV, and yields a large I_{DS} modulation in response to small activity modifications at either the electrolyte/gate or electrolyte/channel interfaces. As suggested by equation 6.1, transconductance (and hence sensitivity) enhancement can be achieved by maximizing C_{eff} and μ, i.e. by tailoring both the electrolyte composition and the chemical nature and morphology of the semiconductor thin film. The effective capacitance C_{eff}, whose value can be modulated by electrolyte pH and gate voltage,[15] eventually exceeds the one of the electrolyte double layer; however, the apparent

charge mobility is observed to generally decrease in liquid-gated architectures (typically in the range 10^{-3}-10^{-4} cm^2 V^{-1} s^{-1})[1,15–17] with respect to solid-state devices with bottom gate.

Within this framework, high-mobility organic semiconductors operating in aqueous environment would lead to further g_m enhancement and would impact on the performances of electrolyte-gated organic devices also when not operated in EGOFET configuration, as in the case of synapstors.

The organic synapstor (synapse-transistor) is a neuromorphic two-terminal device (two of the transistor terminals are short circuited) that exhibits the electrical signature of a biological synapse.[18,19] In a neural network, synapses modulate signal transmission from a pre-synaptic neuron to a post-synaptic one by delivering neurotransmitters across the synaptic cleft; depending on the spiking frequency at the pre-synaptic neuron, the ionic current at the post-synaptic one can decay (depressing behavior) or rise (facilitating behavior) exponentially. This complex regulation mechanism, termed Short-Term Plasticity (STP), is mimicked by the organic synapstor, which exhibits frequency-dependent modulation of the current evoked by potential pulses at the gate. Frequencies higher or lower than a characteristic frequency υ^{-1} yield depressing or facilitating behavior, respectively. The time scale υ is the result of a network of capacitive and resistive elements that are present in the device. The Electrolyte-Gated Organic Synapstor (EGOS) is the liquid-gated counterpart of Nanoparticle Organic Memory Field-Effect Transistor (NOMFET)[18] and it has recently been demonstrated to operate in contact with a population of neural cells,[20] hinting that hybrid bio-electronic synapses may be possibly useful in prosthetics of damaged neural circuits.[21–23] Also in EGOSs a larger mobility should yield a decrease of the characteristic timescale.

Materials like [1]Benzothieno[3,2-b]benzothiophene (BTBT) derivatives are attractive for high performance organic electronics applications.[24] The material of the present study belongs to 2,7-dialkylated BTBTs whose hole mobility exceeds 10 cm^2 V^{-1} s^{-1} in Organic Thin-Film Transistors (OTFTs)[25–27] and 170 cm^2 $V^{-1}s^{-1}$ as measured with field-induced time-resolved microwave conductivity (FI-TRMC).[28] In addition, they possess other attractive features for interfacing them to living matter: i) ease of synthesis and purification;[29,30] ii) solubility in non-chlorinated organic solvents;[31] iii) ease of processing as thin films;[32–36] iv) low T (≈100°C) post-processing yielding to high molecular order;[37,38] v) limited dynamic disorder.[39] Further desirable properties for their use in bio-interfacing devices are their ambient stability (a work function of 5.3 eV makes them less prone to oxidative processes),[28] and their transparency in the visible region that allows the exploitation of the spectromicroscopy techniques typically used for the characterization of biological matrices.[40] BTBT OFETs operated in aqueous environment have not been reported to date.

This work demonstrates 2,7-dioctyl BTBT (C8-BTBT-C8) as active material both in EGOFET and in EGOS architecture (Figure 6.3a). The transconductance of the EGOFET is in order of tens µS, with a maximum observed value as large as 265 µS, while EGOS exhibits the fastest time scale (15 ms) observed to date. These figures of merit prompt this BTBT derivative as an attractive material for organic bioelectronics.

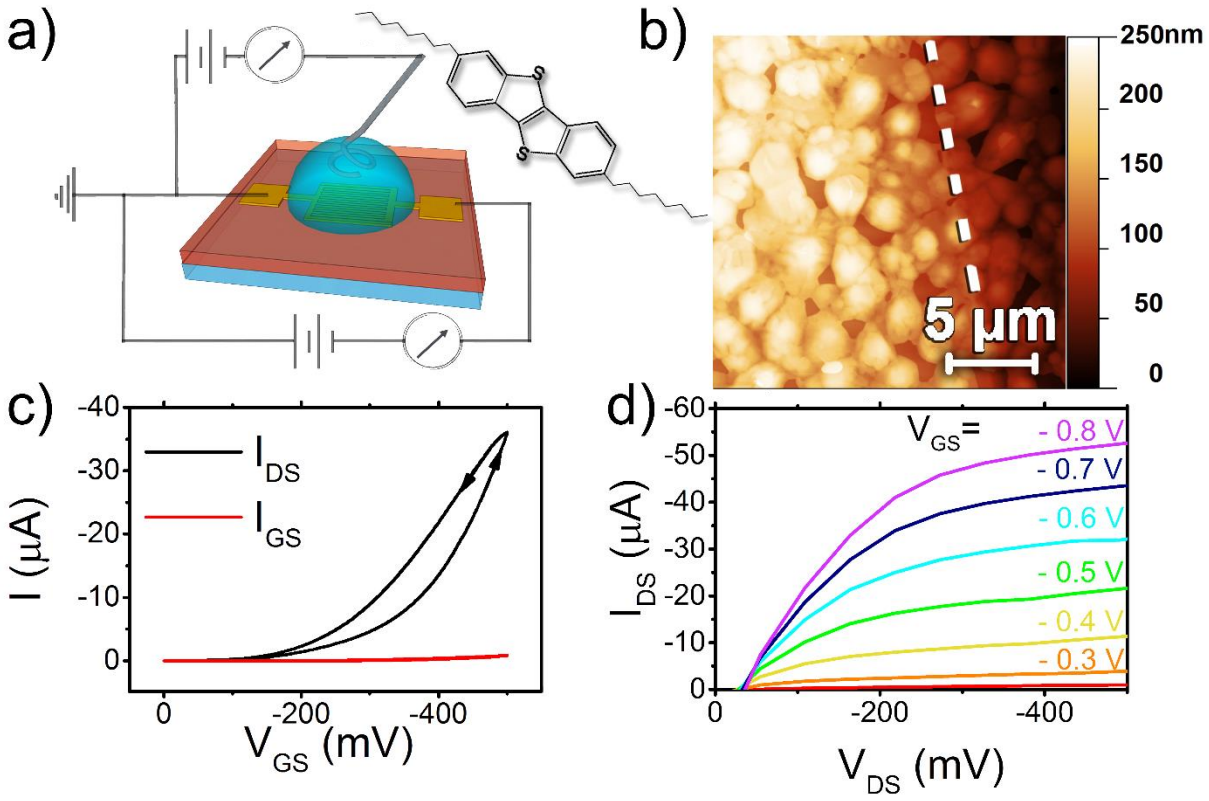

Figure 6.42 EGOFET featuring gold source and drain: a) schematics of the device depicting electrical connections, gold source and drain, platinum top gate electrode and molecular structure of C8-BTBT-C8; b) 20 µm x 20 µm AFM image of the semiconductor film at the edge (dashed line) between quartz substrate (right) and gold electrode (left); c) transfer characteristic recorded at VDS = -0.2V; d) output characteristics. Transistor parameters averaged over ten devices are Vth = -0.356 (± 0.014) V; gm = 45 (±32) µS and ION/IOFF = $10^{3.38}$(±0.06).

6.1.2 Results and discussion

EGOFET and EGOS were fabricated on transparent quartz substrates featuring either metallic (Au) or polymeric electrodes made of poly(3,4-ethylenedioxythiophene): polystyrene sulfonate (PEDOT:PSS). Thin films of C8-BTBT-C8, synthesized according to literature,[29] have been deposited on the test patterns by spin coating and their morphology has been characterized by means of Atomic Force Microscopy (AFM), as shown in Figure 6.1b and Figure 6.2b. All devices were electrically characterized.

Figure 6.1c and Figure 6.1d show I-V characteristics of EGOFETs featuring Au contacts. The output characteristics in Figure 6.1d exhibit ohmic response at low voltages and an incomplete plateau at saturation. In these devices, we observed time evolution of the transfer characteristics, with the performances improving upon repeated measurement cycles up to a stability plateau (Figure S6.1, Supporting Information); transistor parameters have been extracted from transfer curves recorded after reaching the stability regime. From the transfer curve in Figure 6.1c we extracted the best EGOFET parameters obtained in this work V_{th} = -0.360 (± 0.010) V, $I_{ON}/I_{OF}F$ = 103.47(± 0.04), sub-threshold slope = 79 (± 2) mV dec-1 and transconductance gm = 265 (± 5) µS. These values are comparable to state-of-the-art parameters of EGOFETs with aqueous electrolyte that are summarized in Table S6.1.[7,14,17,41–45] It should be noticed that the estimator we choose for comparison is the product of the charge mobility µ by the capacitance C_{eff}, as the device geometry as well as the operation regime may differ. In this respect, our devices with Au electrodes exhibit an average $\mu \cdot C_{eff}$ = 0.112 (± 0.080) $\mu S \cdot V^{-1}$, which is in line with most of the experimental values.

The leakage current I_{GS} is more than two orders of magnitude lower than the channel current I_{DS}, and is purely capacitive as solely due to the build-up of the electrical double layer responsible of the gating; no evidence of faradaic reactions was observed in the relevant V_{GS} range. The counterclockwise hysteresis recorded in I_{DS}, and not observed in I_{GS}, points to the asymmetry of the processes of "electrostatic doping and de-doping"[46,47] which should be ascribed to the interaction between the organic semiconductor and the gate-modulated anion distribution and its dynamics. The detailed nature of this modulation is not addressed in our experiment.

PEDOT:PSS test patterns were prototyped from spin cast films subjected to direct laser ablation with a CAD-driven laser scan marker. Figure 6.2a shows an optical micrograph of the interdigitated PEDOT:PSS source and drain electrodes patterned by laser ablation. Optimization of ablation parameters yields channel lengths as small as 20 µm, resulting in W/L ≈ 1650. The edge roughness of the electrodes is lower than 1 µm and cannot be resolved within the optical image. The process takes a few minutes and is fully reproducible.

The morphology of the C8-BTBT-C8 film that is spin cast on the PEDOT:PSS test pattern is shown in Figure 6.2b. The AFM image at the edge between the electrode and the channel resembles that in Figure 6.1b. The best obtained transfer characteristic for these devices is reported in Figure 6.2c, yielding Vth = -554 (± 2) mV, ION/IOFF = 101.68 (± 0.03), sub-threshold slope = 154 (± 1) mV dec^{-1} and transconductance gm = 24 (± 5) µS. The hysteresis in the source-drain current is much smaller than in the case in Figure 6.1c.

The transistor parameters are perfectly comparable to those extracted from typical devices featuring Au electrodes, as highlighted by the statistical analysis reported in the captions of Figure 6.1 and Figure 6.2. From Table S6.1, our devices with PEDOT:PSS electrodes exhibit an average $\mu \cdot C_{eff}$ = 44 (± 9) $nS \cdot V^{-1}$, which compares to the average value obtained with Au electrodes.

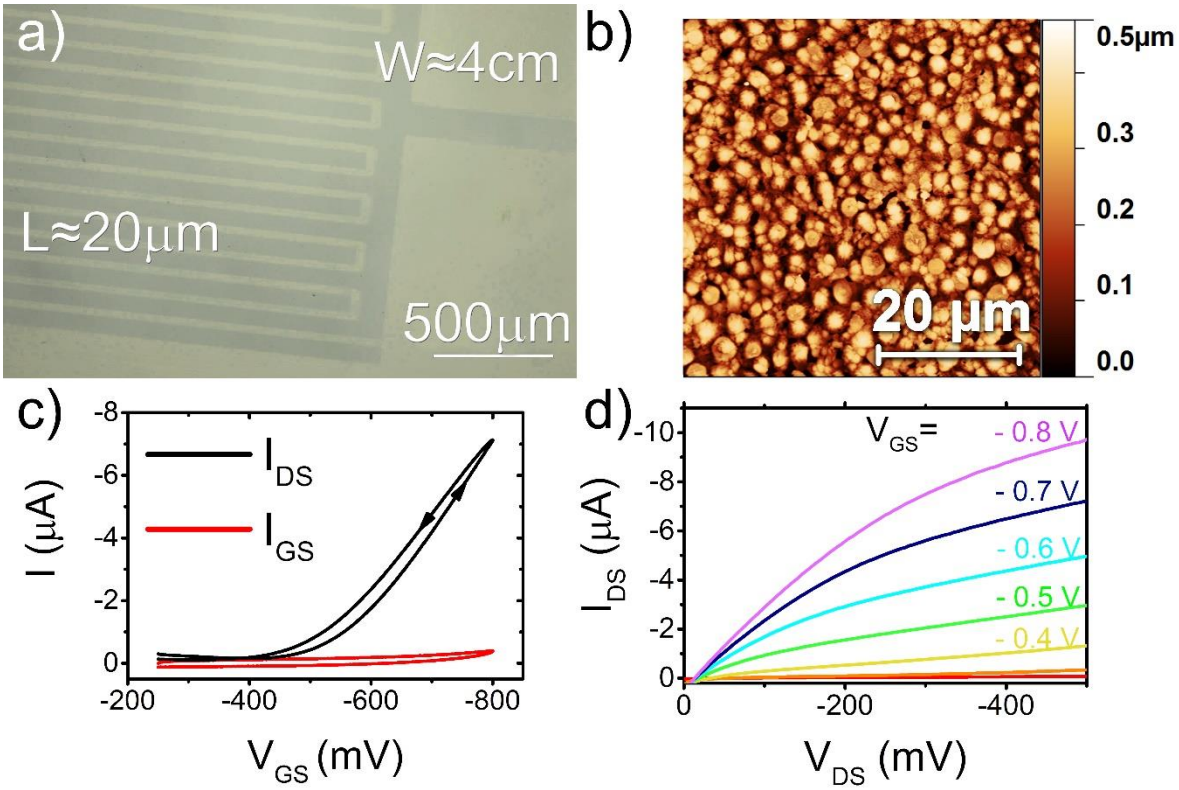

Figure 6.43 EGOFET featuring PEDOT:PSS source and drain: a) Optical micrograph of interdigitated electrodes on quartz. Final W/L ≈ 1650; b) 50 μm x 50 μm AFM image of the semiconductor film on quartz substrate and PEDOT:PSS; c) transfer characteristic recorded at VDS = -0.3 V; d) output characteristics. Statistical analysis on 5 devices yields: Vth = -0.548 (± 0.043) V; gm = 21.8 (± 4.4) μS and ION/IOFF = $10^{3.9}$(±0.7).

Analysis of the AFM topography yields semiconductor thickness, roughness and morphology scaling parameters of C8-BTBT-C8 films, as described in detail in SI (Figure S6.1 and Table S6.2). We notice that: i) morphology parameters are comparable both on Au and PEDOT:PSS devices; ii) C8-BTBT-C8 topography in the channel does not differ significantly from the one observed on the electrodes (either Au or PEDOT:PSS); iii) larger roughness of PEDOT:PSS electrodes does not result in sizable variations of C8-BTBT-C8 surface area (i.e. only a 3% increase of the surface area moving from Au devices to PEDOT:PSS ones). We do not expect a large influence of the mesoscale surface morphology of C8-BTBT-C8 on resistance and/or capacitance, regardless the different nature of the electrodes. We infer that in our device the EGOFET response is mostly to be ascribed to the C8-BTBT-C8 with minimum influence by the electrodes.

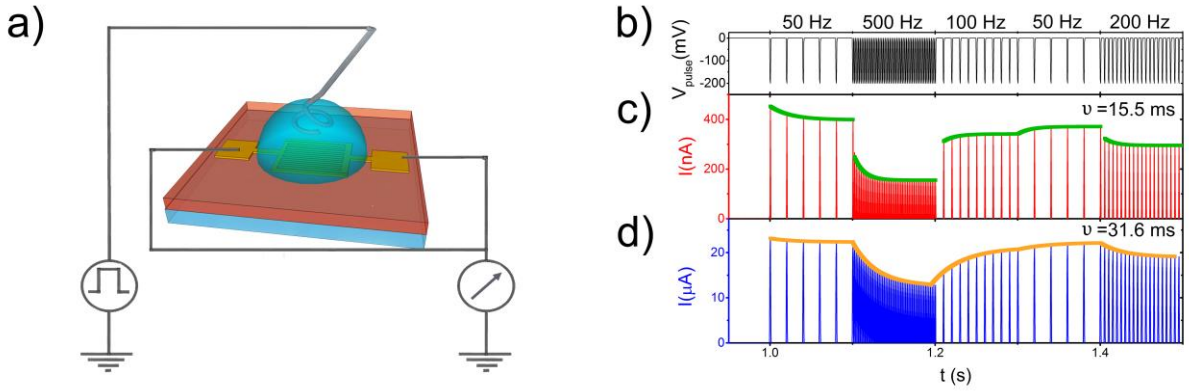

Figure 6.44 EGOS: a) schematics of the device in which are highlighted electrical connections, gold source and drain electrodes and platinum top gate electrode; b) voltammogram of the input pulse train; STP characterization of the EGOSs with c) Au and d) PEDOT:PSS electrodes. Exponential fits of both the STP responses are shown as green and orange line segments.

EGOS response was also investigated for the two types of electrodes. A schematic representation of EGOS configuration is reported in Figure 6.3a, where source and drain electrodes are both grounded. To investigate STP response the top Pt electrode was pulsed with the sequence of spikes depicted in Figure 6.3b (50 Hz, 500 Hz, 100 Hz, 50 Hz, 200 Hz; pulse width = 1 ms, frequency was changed every 100 ms) and the resulting current flowing in the recording electrode was plotted vs time. Current-time, I-t, plots are shown in Figure 6.3c and 6.3d. Both electrode types yield STP response, although STP in PEDOT:PSS devices exhibits the largest values for absolute current intensity and characteristic time scale, υ: current intensity increases from 452 nA to 23.094 μA and υ from 15.5 ms to 31.6 ms moving from Au to PEDOT:PSS contacts. It is worth noticing that, albeit being about ten times larger than the duration of single action potentials in neurons, the observed timescales are comparable with those of collective physiological events such as brain waves. For instance, the timescale herein reported compares to those typical of β-/γ-waves (20-60 Hz) that are evoked in the brain cortex and are known to be pathognomonic signatures of neuro-degenerative diseases such as Parkinson's disease.[48]

As previously stated, in the relevant voltage range we did not observe the occurrence of faradaic processes, hence the recorded current is the displacement current which is linearly correlated with the effective capacitance of the device.[49] The observed increases of both current intensity and υ (i.e. characteristic time scale of the response of the equivalent circuit of the device) suggest that a higher capacitance is established in the case of PEDOT:PSS electrodes with respect to Au ones. Since the only difference between the two architectures resides in the electrode chemical nature and morphology, while the surface area of C8-BTBT-C8 films does not change significantly, this noticeable change of capacitance

hints to the contact interface between the electrodes and the electrolyte, regardless of the presence of the C8-BTBT-C8 film.[15,50] Under this assumption, the marked difference of capacitance can be ascribed to a larger electrolyte-accessible electrodic area in the case of polymeric electrodes, due to hydrophilicity (contact angle $\Theta_{water} \approx 30°$) and porous nature[51,52] in contrast with the rather hydrophobic ($\Theta_{water} \approx 70°$) bulky metallic Au electrodes. Interestingly, as already observed,[15,50] the organic semiconductor thin film appears perfectly permeable to the solution and especially to ions.

The results of Figure 6.3 can be rationalized by assuming that the STP response emerges as a consequence of the RC equivalent of the device, namely a leaking capacitor resulting from ionic distributions in the electrolyte.[53] This opens unprecedented possibilities for EGOS: by controlling the composition of the electrolyte, the area of the electrodes and the thickness of the semi-conductive film it is possible to finely tune the characteristic time and the magnitude of the STP response. To appreciate the advantage of it, in NOMFET architectures this is done by embedding gold nanoparticles in the semiconductor film, and tuning their size and density.[18] Noticeably, the ms-response timescales that can be achieved for C8-BTBT-C8-based EGOS compares to the timescales reported for optimized NOMFETs in air[19] and outperform the few seconds timescale measured on Au-NP/pentacene EGOS on quartz.[20]

6.1.3 Conclusion

This work presented the first liquid-gated organic electronic devices based on BTBT derivatives as active channel material. Both architectures, either with gold or polymeric electrodes, yielded remarkable transconductance (directly related to sensitivity when the device is operated as sensor) as EGOFET and fast dynamic response (few tens ms scale) as EGOS. The devices response and the ease of the fabrication techniques, with rapid prototyping based on laser patterning of the electrodes, prompt for the development of whole organic and completely solution-processed electronic devices working in accumulation regime in physiological environments. These BTBT-based organic electronic devices have the potential to impact on ultra-sensitive diagnostics and therapeutic applications.

6.1.4 Experimental section

Gold electrodes: Gold interdigitated electrodes were fabricated on quartz by means of photolithography and lift-off (Fondazione Bruno Kessler FBK, Trento, Italy). They feature channel length L = 15 µm and width W = 30 mm (W/L = 2000).

PEDOT:PSS electrodes: PEDOT:PSS (PH1000, Clevios™) containing 5% DMSO and 0.2% Silquest (3-glycidoxypropyltrimethoxysilane) was deposited onto clean quartz substrates by spin-coating (3 s @ 500

rpm, 30 s @ 2200 rpm) and cured in thermostatic oven for 20 minutes at 120 °C. CAD drawing of source and drain interdigitated electrodes was transferred on the resulting film by means of direct laser ablation using a Nd:YAG laser scan marker (λ = 1064 nm), equipped with three inertial micrometrical motors that allow precise (displacement accuracy < 1 μm) control of the sample holder displacement along each of the three axes (ScribaR, Scriba Nanotecnologie Srl, Bologna, Italy).[54]

Semiconductor deposition: Thin films of C8-BTBT-C8 were deposited by spin-coating (30 s @ 3500 rpm; 500 rpm s-1) from a 0.4% w/w solution in chloroform and annealed in a standard thermostat oven at 80°C for 40 minutes.

AFM: Morphological characterization was performed using an NT-MDT SMENA Solver platform (Moscow, Russia); all images were obtained in semi-contact mode and analyzed using Gwyddion 2.43 freeware (http://gwyddion.net/).

Electrical Characterization: Device characterization was performed with an Agilent B2902A. Phosphate buffer saline (PBS) (pH = 7.4; i.e. 40 mM Na2HPO4, 10 mM KH2PO4) was used as electrolyte; a Pt wire (ø = 800 μm) immersed in the electrolyte (exposed area = 0.36 cm2) was used as Gate electrode in EGOFET and as pulsed electrode in EGOS.

6.1.5 Supporting information

- Electrical performances

Table S6.4 Comparison between best EGOFETs electrical performances (μ^*C_{eff}) for different active materials and operation regimes and the work presented in this paper.

	Active Layer	μ^*C_{eff} [$\mu S\ V^{-1}$]	Operation Regime	Reference number
Buth et al., 2012	αT6	0.080	Linear	14
Suspène et al., 2013	P3HT-biotin	0.022	Saturation	46
Porrazzo et al., 2014	P3HT	0.006	Saturation	44
	pBTTT not annealed	0.054	Saturation	
	pBTTT annealed	0.048	Saturation	
Mulla et al., 2015	PBTTT-C14	0.069	Saturation	7
Leonardi et al.,2016	DB-TTF:PS	0.072	Saturation	43
Zhang et al., 2016	TIPS	0.0005	Saturation	42
	TIPS:PS	0.025	Saturation	
	TIPS:PS/PFBT	0.636	Saturation	
	diF	0.00015	Saturation	

	diF:PS	0.05	Saturation
	diF:PS/PFBT	0.522	Saturation
This work	C8-BTBT-C8/Au (average)	0.112	Linear
	C8-BTBT-C8/Au (max value)	0.663	Linear
	C8-BTBT-C8/PEDOT:PSS (average)	0.044	Linear
	C8-BTBT-C8/PEDOT:PSS (max value)	0.048	Linear

- Performance evolution

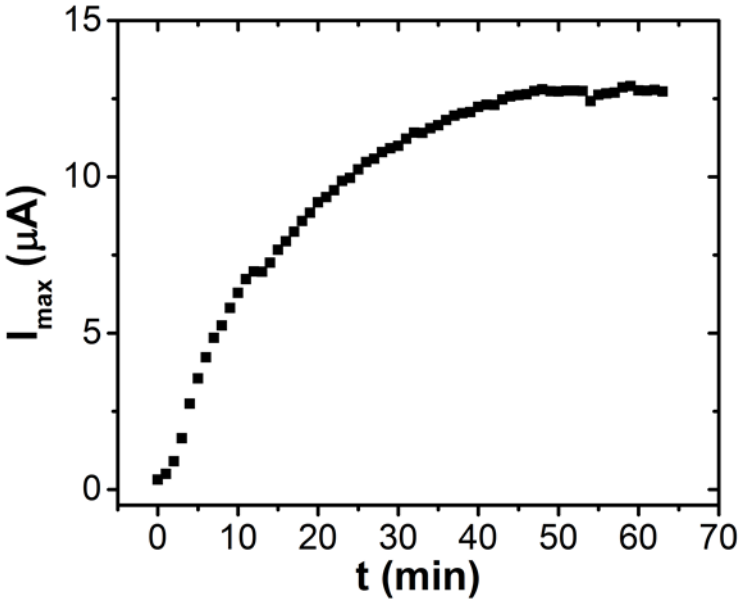

Figure S6.1 Typical evolution of the maximum Drain-Source current with time for C8-BTBT-C8 EGOFETs, obtained from continuously recorder transfer characteristics in linear regime; upon stress, device performances improve several times until reaching a plateau in less than 1 hour.

- AFM Analysis

The morphology from AFM images was analyzed with the power spectral density (PSD) estimated along the fast scan direction from 50 µm x 50 µm images, 1024 points per line. Figure S6.1 shows a representative PSD exhibiting two characteristic wavevectors k1 and k2 that are obtained as the intersection points between the power-law fits of the three different regions of the PSD exhibiting different slope. They correspond to the correlation lengths $\xi1=2\pi/k1$ and $\xi2=2\pi/k2$.

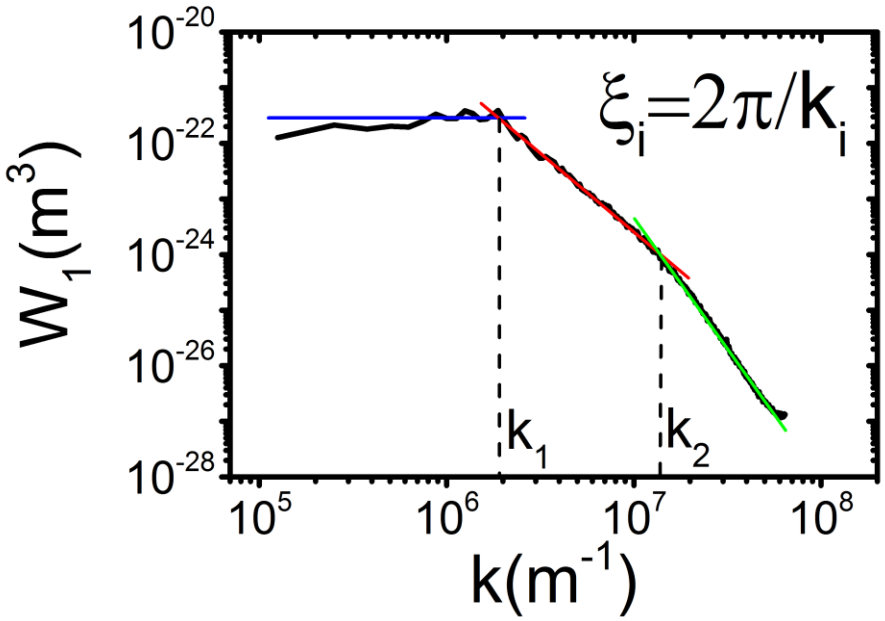

Figure S6.2 Typical power spectral density function of the Fourier transformed AFM data.

We quantify the morphological characteristics of the C8-BTBT-C8 films on the channel and on the electrodes by reporting the saturated roughness and correlation lengths in Table S2, as well as the thickness of BTBT film, estimated by the difference between the two peaks of the height distribution from AFM images. Values refer to regions that can be imaged directly or cropped from images including more than one region. Standard deviations from measurements on different devices and different images of same device are reported as errors.

Table S6.5 Morphological parameters extracted from AFM images and their Radial PSD.

EGOFET electrodes	Region	Thickness BTBT [nm]	Saturated rms roughness [nm]	Correlation length ξ_1 [nm]	Correlation length ξ_2 [nm]	Surface area/Projected area
Au	Electrodes	64±4	19±2	495±48	47±8	1.0028±0.0002
	Channel	70±13	21±1	511±39	120±4	1.0032±0.0002
PEDOT:PSS	Electrodes	120±4	45±3	572±148	62±16	1.018 ± 0.003
	Channel	100.8±30.1	36±4	530±90	58±4	1.067 ± 0.032

- Laser ablation

Figure S6.3 shows the CAD drawing driving the sample holder displacements in the Laser assisted subtractive patterning of interdigitated PEDOT:PSS electrodes. To transfer the electrode patterns on

PEDOT:PSS films, the following ablation parameters have been used: 2 mm/s speed, 10 ns pulse width, 15.5 Hz pulse frequency. The tunable voltage sourcing the laser has been kept to 10 V.

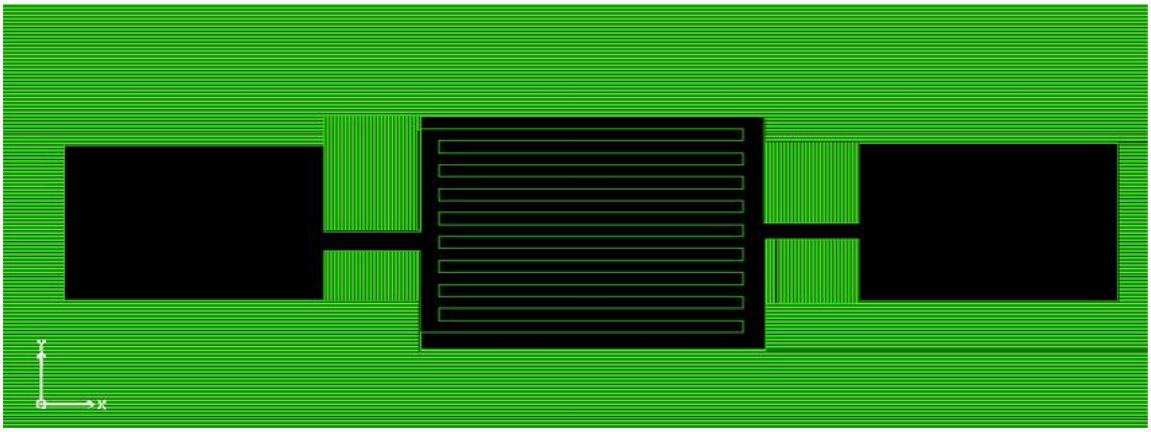

Figure S6.3 CAD drawing of interdigitated electrodes, green lines indicate laser traces.

References

(1) Casalini, S.; Dumitru, A. C.; Leonardi, F.; Bortolotti, C. A.; Herruzo, E. T.; Campana, A.; de Oliveira, R. F.; Cramer, T.; Garcia, R.; Biscarini, F. Multiscale Sensing of Antibody–Antigen Interactions by Organic Transistors and Single-Molecule Force Spectroscopy. *ACS Nano* **2015**, *9* (5), 5051–5062. https://doi.org/10.1021/acsnano.5b00136.

(2) Palazzo, G.; De Tullio, D.; Magliulo, M.; Mallardi, A.; Intranuovo, F.; Mulla, M. Y.; Favia, P.; Vikholm-Lundin, I.; Torsi, L. Detection Beyond Debye's Length with an Electrolyte-Gated Organic Field-Effect Transistor. *Adv. Mater.* **2015**, *27* (5), 911–916. https://doi.org/10.1002/adma.201403541.

(3) Berto, M.; Casalini, S.; Di Lauro, M.; Marasso, S. L.; Cocuzza, M.; Perrone, D.; Pinti, M.; Cossarizza, A.; Pirri, C. F.; Simon, D. T.; et al. Biorecognition in Organic Field Effect Transistors Biosensors: The Role of the Density of States of the Organic Semiconductor. *Anal. Chem.* **2016**, *88* (24), 12330–12338. https://doi.org/10.1021/acs.analchem.6b03522.

(4) Sessolo, M.; Rivnay, J.; Bandiello, E.; Malliaras, G. G.; Bolink, H. J. Ion-Selective Organic Electrochemical Transistors. *Adv. Mater.* **2014**, *26* (28), 4803–4807. https://doi.org/10.1002/adma.201400731.

(5) Knopfmacher, O.; Hammock, M. L.; Appleton, A. L.; Schwartz, G.; Mei, J.; Lei, T.; Pei, J.; Bao, Z. Highly Stable Organic Polymer Field-Effect Transistor Sensor for Selective Detection in the Marine Environment. *Nat. Commun.* **2014**, *5* (1), 2954. https://doi.org/10.1038/ncomms3954.

(6) Casalini, S.; Leonardi, F.; Cramer, T.; Biscarini, F. Organic Field-Effect Transistor for Label-Free Dopamine Sensing. *Org. Electron. physics, Mater. Appl.* **2013**, *14* (1), 156–163. https://doi.org/10.1016/j.orgel.2012.10.027.

(7) Mulla, M. Y.; Tuccori, E.; Magliulo, M.; Lattanzi, G.; Palazzo, G.; Persaud, K.; Torsi, L. Capacitance-Modulated Transistor Detects Odorant Binding Protein Chiral Interactions. *Nat. Commun.* **2015**, *6* (1), 6010. https://doi.org/10.1038/ncomms7010.

(8) Cramer, T.; Campana, A.; Leonardi, F.; Casalini, S.; Kyndiah, A.; Murgia, M.; Biscarini, F. Water-Gated Organic Field Effect Transistors – Opportunities for Biochemical Sensing and Extracellular Signal Transduction. *J. Mater. Chem. B* **2013**, *1* (31), 3728. https://doi.org/10.1039/c3tb20340a.

(9) Strakosas, X.; Bongo, M.; Owens, R. M. The Organic Electrochemical Transistor for Biological Applications. *J. Appl. Polym. Sci.* **2015**, *132* (15). https://doi.org/10.1002/app.41735.

(10) Magliulo, M.; Mallardi, A.; Gristina, R.; Ridi, F.; Sabbatini, L.; Cioffi, N.; Palazzo, G.; Torsi, L. Part per Trillion Label-Free Electronic Bioanalytical Detection. *Anal. Chem.* **2013**, *85* (8), 3849–3857. https://doi.org/10.1021/ac302702n.

(11) Hammock, M. L.; Knopfmacher, O.; Naab, B. D.; Tok, J. B.-H.; Bao, Z. Investigation of Protein Detection Parameters Using Nanofunctionalized Organic Field-Effect Transistors. *ACS Nano* **2013**, *7* (5), 3970–3980. https://doi.org/10.1021/nn305903q.

(12) Kergoat, L.; Piro, B.; Berggren, M.; Horowitz, G.; Pham, M.-C. Advances in Organic Transistor-Based Biosensors: From Organic Electrochemical Transistors to Electrolyte-Gated Organic Field-Effect Transistors. *Anal. Bioanal. Chem.* **2012**, *402* (5), 1813–1826. https://doi.org/10.1007/s00216-011-5363-y.

(13) Buth, F.; Kumar, D.; Stutzmann, M.; Garrido, J. A. Electrolyte-Gated Organic Field-Effect Transistors for Sensing Applications. *Appl. Phys. Lett.* **2011**, *98* (15), 153302. https://doi.org/10.1063/1.3581882.

(14) Buth, F.; Donner, A.; Sachsenhauser, M.; Stutzmann, M.; Garrido, J. A. Biofunctional Electrolyte-Gated Organic Field-Effect Transistors. *Adv. Mater.* **2012**, *24* (33), 4511–4517. https://doi.org/10.1002/adma.201201841.

(15) Di Lauro, M.; Casalini, S.; Berto, M.; Campana, A.; Cramer, T.; Murgia, M.; Geoghegan, M.; Bortolotti, C. A.; Biscarini, F. The Substrate Is a PH-Controlled Second Gate of Electrolyte-Gated Organic Field-Effect Transistor. *ACS Appl. Mater. Interfaces* **2016**, *8* (46), 31783–31790. https://doi.org/10.1021/acsami.6b06952.

(16) Magliulo, M.; Mallardi, A.; Mulla, M. Y.; Cotrone, S.; Pistillo, B. R.; Favia, P.; Vikholm-Lundin, I.; Palazzo, G.; Torsi, L. Electrolyte-Gated Organic Field-Effect Transistor Sensors Based on Supported Biotinylated Phospholipid Bilayer. *Adv. Mater.* **2013**, *25* (14), 2090–2094. https://doi.org/10.1002/adma.201203587.

(17) Toss, H.; Suspène, C.; Piro, B.; Yassar, A.; Crispin, X.; Kergoat, L.; Pham, M.-C.; Berggren, M. On the Mode of Operation in Electrolyte-Gated Thin Film Transistors Based on Different Substituted Polythiophenes. *Org. Electron.* **2014**, *15* (10), 2420–2427. https://doi.org/10.1016/j.orgel.2014.06.017.

(18) Alibart, F.; Pleutin, S.; Guérin, D.; Novembre, C.; Lenfant, S.; Lmimouni, K.; Gamrat, C.; Vuillaume, D. An Organic Nanoparticle Transistor Behaving as a Biological Spiking Synapse. *Adv. Funct. Mater.* **2010**, *20* (2), 330–337. https://doi.org/10.1002/adfm.200901335.

(19) Desbief, S.; Kyndiah, A.; Guérin, D.; Gentili, D.; Murgia, M.; Lenfant, S.; Alibart, F.; Cramer, T.; Biscarini, F.; Vuillaume, D. Low Voltage and Time Constant Organic Synapse-Transistor. *Org. Electron.* **2015**, *21*, 47–53. https://doi.org/10.1016/j.orgel.2015.02.021.

(20) Desbief, S.; di Lauro, M.; Casalini, S.; Guerin, D.; Tortorella, S.; Barbalinardo, M.; Kyndiah, A.; Murgia, M.; Cramer, T.; Biscarini, F.; et al. Electrolyte-Gated Organic Synapse Transistor Interfaced with Neurons. *Org. Electron.* **2016**, *38*, 21–28. https://doi.org/10.1016/j.orgel.2016.07.028.

(21) Saïghi, S.; Mayr, C. G.; Serrano-Gotarredona, T.; Schmidt, H.; Lecerf, G.; Tomas, J.; Grollier, J.; Boyn, S.; Vincent, A. F.; Querlioz, D.; et al. Plasticity in Memristive Devices for Spiking Neural Networks. *Front. Neurosci.* **2015**, *9* (MAR), 1–16. https://doi.org/10.3389/fnins.2015.00051.

(22) Gkoupidenis, P.; Schaefer, N.; Strakosas, X.; Fairfield, J. A.; Malliaras, G. G. Synaptic Plasticity Functions in an Organic Electrochemical Transistor. *Appl. Phys. Lett.* **2015**, *107* (26), 263302. https://doi.org/10.1063/1.4938553.

(23) Tuma, T.; Pantazi, A.; Le Gallo, M.; Sebastian, A.; Eleftheriou, E. Stochastic Phase-Change Neurons. *Nat. Nanotechnol.* **2016**, *11* (8), 693–699. https://doi.org/10.1038/nnano.2016.70.

(24) Takimiya, K.; Osaka, I.; Mori, T.; Nakano, M. Organic Semiconductors Based on [1]Benzothieno[3,2- b][1]Benzothiophene Substructure. *Acc. Chem. Res.* **2014**, *47* (5), 1493–1502. https://doi.org/10.1021/ar400282g.

(25) Schweicher, G.; Olivier, Y.; Lemaur, V.; Geerts, Y. H. What Currently Limits Charge Carrier Mobility in Crystals of Molecular Semiconductors? *Isr. J. Chem.* **2014**, *54* (5–6), 595–620. https://doi.org/10.1002/ijch.201400047.

(26) Schweicher, G.; Lemaur, V.; Niebel, C.; Ruzié, C.; Diao, Y.; Goto, O.; Lee, W.; Kim, Y.; Arlin, J.; Karpinska, J.; et al. Bulky End-Capped [1]Benzothieno[3,2- b]Benzothiophenes: Reaching High-Mobility Organic Semiconductors by Fine Tuning of the Crystalline Solid-

State Order. *Adv. Mater.* **2015**, *27* (19), 3066–3072. https://doi.org/10.1002/adma.201500322.

(27) Janneck, R.; Vercesi, F.; Heremans, P.; Genoe, J.; Rolin, C. Predictive Model for the Meniscus-Guided Coating of High-Quality Organic Single-Crystalline Thin Films. *Adv. Mater.* **2016**, *28* (36), 8007–8013. https://doi.org/10.1002/adma.201602377.

(28) Tsutsui, Y.; Schweicher, G.; Chattopadhyay, B.; Sakurai, T.; Arlin, J.-B.; Ruzié, C.; Aliev, A.; Ciesielski, A.; Colella, S.; Kennedy, A. R.; et al. Unraveling Unprecedented Charge Carrier Mobility through Structure Property Relationship of Four Isomers of Didodecyl[1]Benzothieno[3,2- b][1]Benzothiophene. *Adv. Mater.* **2016**, *28* (33), 7106–7114. https://doi.org/10.1002/adma.201601285.

(29) Ebata, H.; Izawa, T.; Miyazaki, E.; Takimiya, K.; Ikeda, M.; Kuwabara, H.; Yui, T. Highly Soluble [1]Benzothieno[3,2- b]Benzothiophene (BTBT) Derivatives for High-Performance, Solution-Processed Organic Field-Effect Transistors. *J. Am. Chem. Soc.* **2007**, *129* (51), 15732–15733. https://doi.org/10.1021/ja074841i.

(30) Ruzié, C.; Karpinska, J.; Kennedy, A. R.; Geerts, Y. H. Synthesis of 1,6-, 2,7-, 3,8-, and 4,9-Isomers of Didodecyl[1]Benzothieno[3,2- b][1]Benzothiophenes. *J. Org. Chem.* **2013**, *78* (15), 7741–7748. https://doi.org/10.1021/jo401134c.

(31) Li, Y.; Liu, C.; Kumatani, A.; Darmawan, P.; Minari, T.; Tsukagoshi, K. Large Plate-like Organic Crystals from Direct Spin-Coating for Solution-Processed Field-Effect Transistor Arrays with High Uniformity. *Org. Electron.* **2012**, *13* (2), 264–272. https://doi.org/10.1016/j.orgel.2011.11.012.

(32) Uemura, T.; Hirose, Y.; Uno, M.; Takimiya, K.; Takeya, J. Very High Mobility in Solution-Processed Organic Thin-Film Transistors of Highly Ordered [1]Benzothieno[3,2-b]Benzothiophene Derivatives. *Appl. Phys. Express* **2009**, *2* (11), 111501. https://doi.org/10.1143/APEX.2.111501.

(33) Minemawari, H.; Yamada, T.; Matsui, H.; Tsutsumi, J.; Haas, S.; Chiba, R.; Kumai, R.; Hasegawa, T. Inkjet Printing of Single-Crystal Films. *Nature* **2011**, *475* (7356), 364–367. https://doi.org/10.1038/nature10313.

(34) Treier, M.; Arlin, J.-B.; Ruzié, C.; Geerts, Y. H.; Lemaur, V.; Cornil, J.; Samorì, P. Ambipolar Organic Field-Effect Transistors with Balanced Mobilities through Solvent–Vapour Annealing Induced Phase-Separation of Bi-Component Mixtures. *J. Mater. Chem.*

2012, *22* (19), 9509. https://doi.org/10.1039/c2jm31063e.

(35) Gbabode, G.; Dohr, M.; Niebel, C.; Balandier, J.-Y.; Ruzié, C.; Négrier, P.; Mondieig, D.; Geerts, Y. H.; Resel, R.; Sferrazza, M. X-Ray Structural Investigation of Nonsymmetrically and Symmetrically Alkylated [1]Benzothieno[3,2- b]Benzothiophene Derivatives in Bulk and Thin Films. *ACS Appl. Mater. Interfaces* **2014**, *6* (16), 13413–13421. https://doi.org/10.1021/am5015315.

(36) He, D.; Zhang, Y.; Wu, Q.; Xu, R.; Nan, H.; Liu, J.; Yao, J.; Wang, Z.; Yuan, S.; Li, Y.; et al. Two-Dimensional Quasi-Freestanding Molecular Crystals for High-Performance Organic Field-Effect Transistors. *Nat. Commun.* **2014**, *5* (1), 5162. https://doi.org/10.1038/ncomms6162.

(37) Iino, H.; Hanna, J. Availability of Liquid Crystallinity in Solution Processing for Polycrystalline Thin Films. *Adv. Mater.* **2011**, *23* (15), 1748–1751. https://doi.org/10.1002/adma.201004474.

(38) Iino, H.; Usui, T.; Hanna, J. Liquid Crystals for Organic Thin-Film Transistors. *Nat. Commun.* **2015**, *6* (1), 6828. https://doi.org/10.1038/ncomms7828.

(39) Illig, S.; Eggeman, A. S.; Troisi, A.; Jiang, L.; Warwick, C.; Nikolka, M.; Schweicher, G.; Yeates, S. G.; Henri Geerts, Y.; Anthony, J. E.; et al. Reducing Dynamic Disorder in Small-Molecule Organic Semiconductors by Suppressing Large-Amplitude Thermal Motions. *Nat. Commun.* **2016**, *7* (1), 10736. https://doi.org/10.1038/ncomms10736.

(40) Gemayel, M. El; Börjesson, K.; Herder, M.; Duong, D. T.; Hutchison, J. A.; Ruzié, C.; Schweicher, G.; Salleo, A.; Geerts, Y.; Hecht, S.; et al. Optically Switchable Transistors by Simple Incorporation of Photochromic Systems into Small-Molecule Semiconducting Matrices. *Nat. Commun.* **2015**, *6* (1), 6330. https://doi.org/10.1038/ncomms7330.

(41) Zhang, Q.; Leonardi, F.; Casalini, S.; Temiño, I.; Mas-Torrent, M. High Performing Solution-Coated Electrolyte-Gated Organic Field-Effect Transistors for Aqueous Media Operation. *Sci. Rep.* **2016**, *6* (1), 39623. https://doi.org/10.1038/srep39623.

(42) Leonardi, F.; Casalini, S.; Zhang, Q.; Galindo, S.; Gutiérrez, D.; Mas-Torrent, M. Electrolyte-Gated Organic Field-Effect Transistor Based on a Solution Sheared Organic Semiconductor Blend. *Adv. Mater.* **2016**, *28* (46), 10311–10316. https://doi.org/10.1002/adma.201602479.

(43) Porrazzo, R.; Bellani, S.; Luzio, A.; Lanzarini, E.; Caironi, M.; Antognazza, M. R.

Improving Mobility and Electrochemical Stability of a Water-Gated Polymer Field-Effect Transistor. *Org. Electron.* **2014**, *15* (9), 2126–2134. https://doi.org/10.1016/j.orgel.2014.06.002.

(44) Wang, D.; Noël, V.; Piro, B. Electrolytic Gated Organic Field-Effect Transistors for Application in Biosensors—A Review. *Electronics* **2016**, *5* (1), 9. https://doi.org/10.3390/electronics5010009.

(45) Suspène, C.; Piro, B.; Reisberg, S.; Pham, M.-C.; Toss, H.; Berggren, M.; Yassar, A.; Horowitz, G. Copolythiophene-Based Water-Gated Organic Field-Effect Transistors for Biosensing. *J. Mater. Chem. B* **2013**, *1* (15), 2090. https://doi.org/10.1039/c3tb00525a.

(46) Egginger, M.; Bauer, S.; Schwödiauer, R.; Neugebauer, H.; Sariciftci, N. S. Current versus Gate Voltage Hysteresis in Organic Field Effect Transistors. *Monatshefte für Chemie - Chem. Mon.* **2009**, *140* (7), 735–750. https://doi.org/10.1007/s00706-009-0149-z.

(47) D'Angelo, P.; Stoliar, P.; Cramer, T.; Cassinese, A.; Zerbetto, F.; Biscarini, F. Quantitative Analysis of Charge-Carrier Trapping in Organic Thin-Film Transistors from Transfer Characteristics. *Appl. Phys. A* **2009**, *95* (1), 55–60. https://doi.org/10.1007/s00339-008-4996-y.

(48) Lopes da Silva, F. Neural Mechanisms Underlying Brain Waves: From Neural Membranes to Networks. *Electroencephalogr. Clin. Neurophysiol.* **1991**, *79* (2), 81–93. https://doi.org/10.1016/0013-4694(91)90044-5.

(49) Bard, A. J.; Faulkner, L. R. *Electrochemical Methods: Fundamentals and Applications*; 2000.

(50) Lago, N.; Cester, A.; Wrachien, N.; Benvenuti, E.; Quiroga, S. D.; Natali, M.; Toffanin, S.; Muccini, M.; Meneghesso, G. Investigation of Mobility Transient on Organic Transistor by Means of DLTS Technique. *IEEE Trans. Electron Devices* **2016**, *63* (11), 4432–4439. https://doi.org/10.1109/TED.2016.2611142.

(51) Newman, J.; Tiedemann, W. Porous-Electrode Theory with Battery Applications. *AIChE J.* **1975**, *21* (1), 25–41. https://doi.org/10.1002/aic.690210103.

(52) Elshner, Andreas; Kirchmeyer, Stephan; Lovenich, Wilfried; Merker, Udo; Reuter, K. *PEDOT. Principles and Applications of an Intrinsically Conductive Polymer*; CRC Press, 2010.

(53) Israelachvili, J. N. *Intramolecular and Surface Forces: Revised Third Edition*; Academic Press, 2011.

(54) Giordani, M.; Di Lauro, M.; Berto, M.; Bortolotti, C. A.; Vuillaume, D.; Gomes, H. L.; Zoli, M.; Biscarini, F. Whole Organic Electronic Synapses for Dopamine Detection; Kymissis, I., Shinar, R., Torsi, L., Eds.; 2016; Vol. 9944, p 99440P. https://doi.org/10.1117/12.2239532.

Ringraziamenti

Alla fine è finito anche il mio dottorato, che sembrava infinito tra studio, gravidanze, bambini e pandemie.

Se sono arrivata dove sono adesso lo devo a tantissime persone, primo fra tutti al prof. Fabio Biscarini a cui sicuramente devo il fatto di aver creduto in me, accettandomi come dottoranda e spronandomi sempre, cercando di farmi vincere le paure e facendomi crescere come persona e come scienziata.

Un ringraziamento anche al prof. Michele Zoli che ha sempre risposto a tutti i miei quesiti nei momenti di smarrimento con molta gentilezza e pazienza e che mi ha aiutata a destreggiarmi nel mondo delle neuroscienze.

Un grazie va anche a Carlo che ha sempre ascoltato i miei lamenti e il mio pessimismo, accompagnandoli con il suo solito humor, dandomi anche consigli scientifici.

Ringrazio Marcello, che, anche se non vuole essere annoverato nella lista dei miei amici, è la persona più fidata dentro e fuori dal laboratorio, a cui si può raccontare e chiedere tutto, anche se non è detto che si ottenga una risposta.

Grazie a Matteo che, nonostante la recente apparizione nel LeoLab, ha scalato le classifiche delle mie persone preferite con la sua pazienza, competenza, calma e simpatia.

Come non ringraziare anche Michele che mi ha accolta come piccola bambina spaurita ed è riuscito a infondermi coraggio per farmi credere sempre nelle mie capacità.

Ringrazio i miei super amici Chiara, Pippy (Simone), Carla, Giulia e Sofia per avermi ascoltata, rassicurata e accompagnata sempre, nonostante i lamenti e le difficoltà.

Grazie alla mia mamma Luisa, che nonostante non sapesse sempre bene che cosa stessi facendo, ha sempre creduto in me, nei miei sforzi e ha fatto di tutto per permettermi di studiare e diventare quello che sono, crescendomi senza impormi limiti e incoraggiando le mie peculiarità e rendendosi sempre una fonte di ispirazione per il coraggio e la forza di affrontare le difficoltà.

Ringrazio il mio fratellino Riccardo, mio compagno di giochi e di vita, un punto saldo.

Ringrazio mio fratello Alessandro, Patrizia e Andrea che nonostante la lontananza sono sempre presenti per me.

Un grazie allargato a tutta la mia famiglia, cugini, zii, suoceri, cognati e nonni che sono sempre una rete di supporto importante, perché qualunque cosa succeda, sai che quelle persone non te le toglierà nessuno.

Infine ringrazio la mia famiglia: Andrea che ha sopportato tanti momenti difficili facendomi sempre sentire amata, offrendomi birre nei momenti bui, lasciandomi sempre il tempo di cui avevo bisogno senza lamentarsi e facendomi sempre vedere il lato bello delle cose; Niccolò e Irma, che, se pure inconsapevolmente, mi hanno fatto capire le priorità della vita e che le difficoltà che vedevo erano tutte relative. Grazie a loro so che nella vita in qualche modo si va sempre avanti e che niente è insormontabile.

Come ultimo, più che un ringraziamento una speranza: al mio papà Gianfranco che era una persona sempre curiosa e pronta ad imparare, da cui ho preso il carattere spigoloso e puntiglioso, spero che la conclusione di questo percorso lo renda fiero.